

Characterization of the physical properties of the ROSETTA target comet 67P/Churyumov-Gerasimenko

Von der Fakultät für Elektrotechnik, Informationstechnik, Physik
der Technischen Universität Carolo-Wilhelmina
zu Braunschweig
zur Erlangung des Grades einer
Doktorin der Naturwissenschaften
(Dr.rer.nat.)
genehmigte
Dissertation

von Cecilia Tubiana
aus Moncalieri/Italien

Bibliografische Information Der Deutschen Bibliothek

Die Deutsche Bibliothek verzeichnet diese Publikation in der Deutschen Nationalbibliografie; detaillierte bibliografische Daten sind im Internet über <http://dnb.ddb.de> abrufbar.

1. Referentin oder Referent: Prof. Dr. Jürgen Blum
 2. Referentin oder Referent: Prof. Dr. Michael A'Hearn
- eingereicht am: 18 August 2008
mündliche Prüfung (Disputation) am: 30 Oktober 2008

ISBN 978-3-936586-89-3

Copernicus Publications 2008

<http://publications.copernicus.org>

© Cecilia Tubiana

Printed in Germany

Contents

Summary	7
1 Comets: introduction	11
1.1 Physical properties of cometary nuclei	15
1.1.1 Size and shape of a cometary nucleus	18
1.1.2 Rotational period of a cometary nucleus	22
1.1.3 Albedo of cometary nuclei	24
1.1.4 Bulk density of cometary nuclei	25
1.1.5 Colors indices and spectra of the nucleus	25
1.2 Dust trail and neck-line	27
2 67P/Churyumov-Gerasimenko and the ESA's ROSETTA mission	29
2.1 Discovery and orbital evolution	29
2.2 Nucleus properties	30
2.3 Annual light curve	32
2.4 Gas and dust production	32
2.5 Coma features, trail and neck-line	35
2.6 ESA's ROSETTA mission	35
2.7 Motivations of the thesis	39
3 Observing strategy and performance of the observations of 67P/C-G	41
3.1 Observations: strategy and preparation	41
3.2 Instrumentation	43
3.3 Datasets	43
3.3.1 April 2004	45
3.3.2 June 2004	46
3.3.3 May 2006	46
3.3.4 August 2006	47
3.3.5 July 2007	47
3.3.6 Photometric and spectroscopic calibrations	48
3.4 Data reduction: instrumental calibration of photometric and spectroscopic frames	48
3.5 Photometry: methods & calibrations	55
3.5.1 Methods	55
3.5.2 Flux calibration of photometric images	57
3.5.3 Correction for heliocentric and geocentric distances and phase angle	59

3.5.4	Errors on photometric measurements	60
3.6	Spectroscopy: method	60
3.6.1	Uncertainties on the spectra	60
4	Results on 67P/C-G	65
4.1	Activity at large heliocentric distance: coma	65
4.2	Rotational period and phase function of the nucleus	67
4.2.1	Datasets	69
4.2.2	Method	71
4.2.3	Results using May 2006 + August 2006 datasets	72
4.2.4	Results using May 2006 + August 2006 + July 2007 datasets	76
4.2.5	Discussion	78
4.3	Shape and size of the nucleus	81
4.4	Surface colors and reflectance spectra of the nucleus	82
4.5	Tail-like structure	87
5	Discussion of the results	93
5.1	Activity at large heliocentric distance	93
5.2	Rotational period	93
5.3	Phase function of the nucleus	94
5.4	Light curve of the nucleus	96
5.5	Size and shape of the nucleus	96
5.6	Nucleus colors and reflectance	98
5.7	Tail-like structure	99
5.8	Dust and gas production	102
5.9	Comparisons with other “spaceflight” comets	103
6	Conclusions	107
A	FORS2 filters and grism used in the observing runs	109
B	Flux calibration of photometric images	111
B.1	Aperture photometry	111
B.2	Atmospheric extinction	112
B.3	Color transformation	114
B.4	Determination of flux calibration coefficients	116
C	Table of measured brightness of 67P/C-G	119
D	Rotational period and phase function determination	127
D.1	Phase Dispersion Minimization method	127
D.2	χ^2 minimization method	129
	Bibliography	133
	Publications	139
	Acknowledgements	141

Curriculum Vitae

143

Summary

This thesis is based on the analysis and interpretation of photometric and spectroscopic observations of the Jupiter family comet (JFC) 67P/Churyumov-Gerasimenko (67P/C-G) at large heliocentric distance. The aim of this study is to provide a good characterization of the nucleus of the ROSETTA target comet and its dust environment far away from the Sun. This information is of high importance for a good planning of the rendezvous of the ROSETTA spacecraft with 67P/C-G. Moreover, this study will provide valuable information on the basic physical properties of the nucleus of JFCs and their dust environment far away from the Sun, helping to understand if 67P/C-G behaves as a typical Jupiter family comet or not.

The observations were carried out between April 2004 and July 2007, when the comet was moving in its aphelion arc between 4.6 AU pre-aphelion and about 4.6 AU post-aphelion. From our analysis of the point spread function, the comet appeared point like at all observing epochs, indicating that no significant coma was present around the nucleus at large heliocentric distance. In this respect, 67P/C-G behaves like several other JFCs. Moreover, we can also infer that supervolatiles like CO may be either absent in the top surface layer of the nucleus or covered by temporary crust or confined to regions not exposed to sunlight during aphelion.

The multiple solutions for the rotational period of 67P/C-G, as determined from our observations, fall in the range $T_{rot} = 12.6801 - 12.8612$ h and are in general agreement with the rotational periods published by Lowry et al. (2006) and Lamy et al. (2006). Although from our solutions a final conclusion on the accurate rotational period cannot be drawn, our rotational period estimates have a much higher intrinsic accuracy rather than the ones of Lowry et al. (2006) and Lamy et al. (2006). Concerning the rotational period, 67P/C-G behaves like a rather typical JFC. In fact, our multiple solutions fall in the range of values determined for the bulk of the nuclei of ecliptic comets (Lamy et al. 2004).

The phased light curve of 67P/C-G has an asymmetric, double-peak profile with a maximum amplitude $\Delta m = 0.40 \pm 0.07$ mag and mean absolute R filter magnitude $H = 15.35 \pm 0.04$ mag. We determined a lower limit for the axis-ratio $a/b \geq 1.45 \pm 0.09$ and an effective radius of the nucleus $R_{eff} = 2.38 \pm 0.04$ km, assuming an albedo of 0.04. The former value is in agreement with the determinations by Lowry et al. (2006) and Lamy et al. (2006). Our effective radius is well compatible with the one determined by Lowry et al. (2006). The effective radius determined by Lamy et al. (2006), instead, is not in agreement with our estimation within the uncertainties. This disagreement is most likely an effect of changes of the viewing geometry of the comet between our observations and Lamy et al. (2006) one. Our estimations for the rotational period and lower limit for the axis ratio of 67P/C-G are close to the mean values of the effective radius and axis-ratio distributions for ecliptic comets, as determined by Lamy et al. (2004). Thus, also in this

aspect, 67P/C-G is a rather typical Jupiter family comet.

Our observations covered the phase angle range between 0.5° and 10° . 67P/C-G does not show opposition effect at small phase angles; we determined that the brightness dependence on phase angle is linear and very steep, with linear phase function coefficient $\beta = 0.061 - 0.076 \text{ mag}^\circ$. The possible linear phase function coefficient of 67P/C-G was found to be steeper than the one usually assumed for JFCs (Lamy et al. 2004), while it is close to the value determined, for instance, for comet 2P/Encke (Fernandez et al. 2000, Bönhardt et al. 2008).

The nucleus of 67P/C-G is slightly redder than the Sun, with a constant reddening slope of $\sim 11 \text{ \%}/1000 \text{ \AA}$. No color variation with rotational phase is found, based on broad-band color indices and reflectance spectra of the nucleus. The V-R color index determined by Lowry et al. (2006) is slightly lower than the ones we obtained, while the averaged V-R color index determined by Lamy et al. (2006) is in agreement with our results. The nuclear colors we determined for 67P/C-G are slightly redder than the mean colors determined for ecliptic comets by Lamy et al. (2004). The absence of absorption or emission features in our spectra and a rather constant spectral slope ($\sim 11 \text{ \%}/1000 \text{ \AA}$) are in agreement with visible spectra of other ecliptic comets (Luu 1993). We iterate the conclusion that 67P/C-G is a rather typical Jupiter family comet concerning its spectral behaviour in the visible wavelength range.

In April 2004, June 2004 and May 2006 we detected a tail-like structure of heavy grains associate with 67P/C-G. It displays a mean R filter surface brightness of $27.5 \pm 0.1 \text{ mag}''^2$ in April 2004, $28.1 \pm 0.1 \text{ mag}''^2$ in June 2004 and $28.5 \pm 0.2 \text{ mag}''^2$ in May 2006. The tail-like structure was not detected in July 2007, despite similar sensitivity as in April 2004. Using the June 2004 observations, for the first time we determined also the visible colors of the tail-like structure: $V-R = 0.95 \pm 0.14 \text{ mag}''^2$ and $R-I = 0.39 \pm 0.14 \text{ mag}''^2$, which correspond to a mean spectral reddening of $\sim 17 \text{ \%}/1000 \text{ \AA}$. Thus, on the average, the tail-like structure looks redder than the nucleus of 67P/C-G. Based on geometrical considerations (position angle of the tail-like structure), we concluded that the tail-like structure is more compatible with a neck-line activity of the comet during the recent perihelion passage (i.e. 2002/03) rather with an “old” dust trail, composed of large dust particles emitted during the previous orbits of 67P/C-G, i.e. 1995/96 and earlier. Our conclusion is strengthened by the fact that the surface brightness of the tail-like structure is not a linear function of $\log(r)$, as it would have been expected for a “old” dust trail.

In conclusion, 67P/C-G is a rather typical Jupiter family comet concerning most of the aspects we dealt with.

The knowledge we acquired about the comet’s behaviour of large heliocentric distance is of high importance for a good planning of the ROSETTA spacecraft rendezvous with the comet, which will take place at $\sim 4.5 \text{ AU}$ of heliocentric distance. No observations of 67P/C-G from previous aphelion passages are available which can be compared with our results to estimate if changes in the comet’s behaviour at large heliocentric distance took place during the last apparitions. The gas and dust production rates of 67P/C-G close to perihelion show similar behaviour during the last three apparitions, indicating that the comet’s activity did not change significantly during the last orbital passages (Schleicher 2006, Weiler et al. 2004). This might suggest that also the comet’s behaviour at large heliocentric distance did not change from one orbital revolution to the other and we could

expect that during its approach to 67P/C-G, ROSETTA will find the same conditions we detected during our observations.

1 Comets: introduction

One of the most spectacular phenomena in the Solar System is the apparition of a bright comet, which can be easily seen in the sky by naked eyes. Comets attracted and fascinated the human being for the last several thousand years, as is reported from paintings and drawings of comets on caves, cloths and observations of early writers. Since early times, comets were believe to be bad omens and their apparitions were associated with disasters, calamities, tragedies and so on. One example is provided by the Bayeux tapestry showing the 1066 apparition of comet Halley.

It was only in 1577 that Tycho Brahe demonstrated that comets are celestial objects and not atmospheric phenomena. He observed a very bright comet (C/1577 V1) with accurate instruments and from various locations in Europe and due to the small comet's parallax, he concluded that the comet must have been further away than the Moon.

Edmond Halley discovered that comets are members of the solar system. Using Newton's gravitational theory, he computed the orbit of several comets and showed that the comet apparitions in 1531, 1607 and 1682 belong to the same comet with orbital period of about 75 years. He also noticed that the time interval between successive perihelion passages was not the same and he concluded that this could have been due to perturbation of the cometary orbit produced by Jupiter and Saturn. Halley successfully predicted that the same comet would have appeared in 1758, as it was observed. After his success this object was named comet Halley.

During early times, comets were studied basically from the point of view of their dynamics, while with the passage of time, cometary research evolved to the study of the nature of comets. In the last decades, the focus is mostly in the understanding of the origin, physics and chemistry of comets.

What are comets? The three main parts of a comet are the nucleus, the coma and the tails (Fig. 1.1 and 1.2).

According to the icy-conglomerate model (Whipple 1950) the *nucleus* is a discrete rotating body which consists of water ice (about 80%), complex molecules formed out of abundant elements (H, C, N and O) and dust. The diameter of the nucleus is very small and it is typically about 1 to 10 km.

When the comet is far away from the Sun, only the nucleus is present. As it approaches the Sun, due to solar heating, the ice sublimates producing gas, called parents molecules, (i.e. CH₄, CO, CO₂, H₂O) which drags along dust. It expands in the vacuum giving rise to the *coma*, which in the visible has a dimension up to 10⁴ - 10⁵ km. The heliocentric distance at which sublimation becomes important and thus comets become active depends on which ice (i.e. H₂O, CO₂, CO) is present in the top surface layers of the nucleus and is therefore exposed to sunlight or to the related heat wave expanding into the upper sur-



Figure 1.1: Image of comet Hale-Bopp, showing coma and tails (dust tail: yellowish, plasma tail: bluish). The nucleus is embedded in the coma and it is not visible. Image adapted from: <http://www.secretum-omega.com/HaleBopp.gif>.

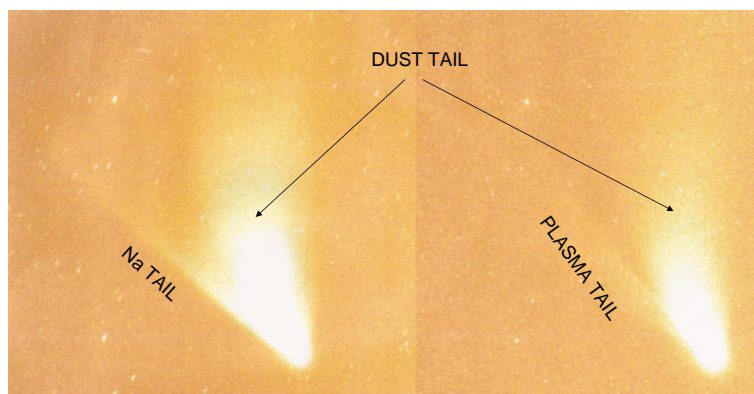


Figure 1.2: Image of comet Hale-Bopp in narrow-band Na (left panel) and H_2O^+ (right panel) filters. The dust tail is visible in both images. The sodium tail and the plasma tail are marked. Image adapted from Cremonese et al. (1997).

face layers. Figure 1.3 shows the sublimation rate as function of heliocentric distance for different ices.

The cut-off distance for water sublimation is around 3 AU solar distance after which the activity of short period comets is usually no longer driven by water sublimation. It is frequently found that these comets are inactive at larger distances. However, long period comets (i.e. Hale-Bopp (Szabó et al. 2008)) display activity at much larger heliocentric distance, which can be explained for instance by sublimation of CO ice.

The parent molecules are subjected to various physical processes (i.e dissociation, ionization, etc.) which transform them into daughter species.

The dust particles dragged outwards by the gas are subject to the radiation pressure of the Sun which pushes them away from the comet and gives rise to the *dust tail*. The dust grains move in orbits with slowly increasing semi-major axis and as a result their Keplerian velocities decrease slowly relative to that of the cometary nucleus and they lag

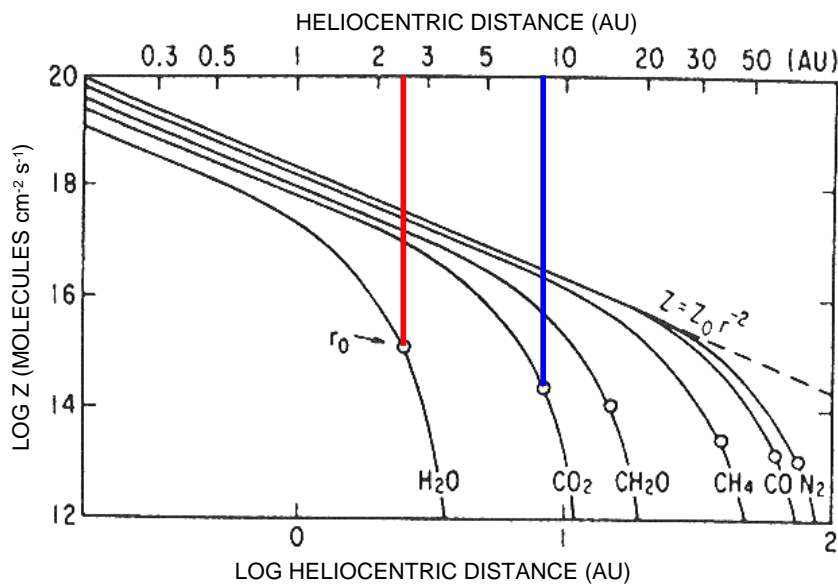


Figure 1.3: Sublimation rate for various ices as function of the heliocentric distance. The distance at which sublimation becomes negligible is marked by r_0 . Figure adapted from Delsemme (1982).

behind the nucleus and coma in their orbits. This produces the broad curved appearance of the dust tail when the comet is close to the Sun. The dust tail is visible through the light scattering of the solar radiation by the dust particles, which explains its yellowish color in photographs. It generally extends up to about 10^7 km, but in some cases dust tails can reach extensions > 1 AU.

Incident UV radiation breaks up the parent molecules released by the nucleus and it also ionizes them. The ionized gas is accelerated away from the coma by the solar wind to produce the *plasma tail* which extends up to about $10^7 - 10^8$ km. The structure and dynamics of the plasma tail are basically due to the interaction of the cometary plasma and the solar wind. The ionized cometary gas is coupled to the solar wind through the interplanetary magnetic field. The dominant emission in plasma tails in the visible is the one of CO^+ . Since this emission lies in the blue spectral region, the ion tail appears bluish in color photographs.

Visible images of cometary coma and dust tail are dominated by μm -sized particles. The dust mass which is released by a comet to the interplanetary space is mainly carried by mm-sized or larger particles (Agarwal 2007, and references therein). These dust grains have low emission speed (about m/s) and are little sensitive to solar radiation pressure, thus they remain close to the comet orbit for two or more revolutions around the Sun. They appear as a faint linear structure, called *dust trail*.

A *neutral gas tail* was discovered in 1997 (Cremonese et al. 1997). It consists of sodium atoms which have a high efficiency for resonance fluorescence emission of the sunlight and are thus also subjected to the radiation pressure.

Why is it important to study comets? Comets spend most of their life far away from the Sun where they are not active. Only a thin layer (order of meters) of the material of

the nucleus is abraded at every perihelion passage due to comet activity and only a few meters of the upper surface layers warm up from the heat wave from sunlight. The deep interior of the nucleus remains unaffected at cold temperature. Therefore, the inner core of a comet may represent the composition of the original material at the time of its formation. Systematic studies of comet nuclei can give information about the nature of the material present at the time of the Solar System formation.

In the 20th century comets were tried to be subdivided in different classes according to their properties. A first distinction was done based on the orbital period: comets with period longer than 200 y were defined long period comets, while the ones with period shorter than 200 y were called short period comets. Short period comets were then split in two classes: Jupiter family comets (JFCs), with period smaller than 20 y whose orbits are governed by Jupiter, and Halley-type comets, with longer period (between 20 and 200 y). The historical division between JFCs and Halley-type comets based on their orbital period can be iterated based on their orbital dynamics. Figure 1.4 shows the inclination of short period comets versus their semi-major axis. The red vertical line shows the historical division at $T = 20$ y, which, through Kepler's third law, corresponds to semi-major axis $a = 7.4$ AU.

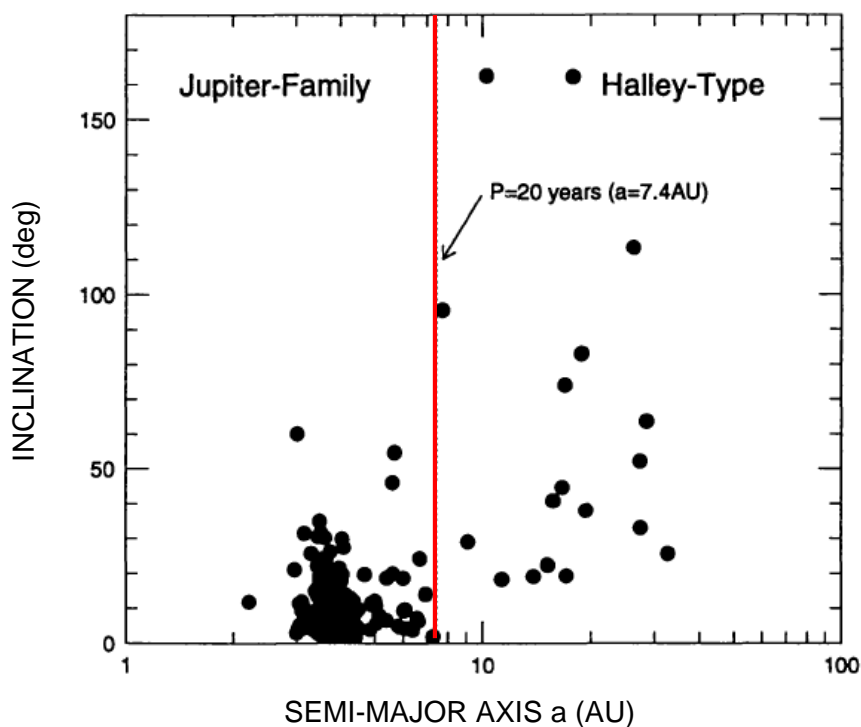


Figure 1.4: Distribution of the inclination of short period comets versus semi-major axis. The red vertical line shows the historical division between JFCs and Halley-type comets at $T = 20$ y, which corresponds to $a = 7.4$ AU. Figure adapted from Levison (1996).

There is a strong concentration of objects with semi-major axis between 3 and 4 AU and low inclination, while comets with $a > 7$ AU display a more uniform inclination distribution. Comets on the left-hand side of the plot tend to have aphelion close to the orbit of

Jupiter, thus they are dynamically dominated by this planet: they are the Jupiter family comets. Their inclination distribution is very flat, with mean inclination of 10° , thus their are approximately confined to the ecliptic plane. Moreover, JFCs are generally in prograde orbits. Halley-type comets, instead, have a more isotropic inclination distribution, with a mean inclination of 41° and several of them are in retrograde orbits (Levison 1996). Levison (1996) proposed a new classification based on the Tisserand parameter (with respect to Jupiter):

$$T_J = \frac{a_J}{a} + 2\sqrt{\frac{a(1-e^2)}{a_J}} \cos(i), \quad (1.1)$$

where a_J is Jupiter's semi-major axis and a , e and i are the comet's semi-major axis, eccentricity and inclination, respectively. Thus, it is based on the orbital elements and uses dynamical properties to differentiate between groups of comets. The Tisserand parameter is approximately constant for any given comet, even after perturbation due to Jupiter. Comets with $T_J > 2$ are defined Ecliptic comets (ECs), while the ones with $T_J < 2$ are Near Isotropic comets (NICs). Halley-type and long period comets are NICs. JFCs have $2 < T_J < 3$, thus they are ECs.

Where do comets come from? Based on observed orbital characteristics (eccentricity $e \leq 1$) and isotopic ratios ($^{12}\text{C}/^{13}\text{C}$ measured in many comets and few other isotopic ratios seen in comet Halley), comets are believed to be members of the solar system. Oort (1950) pointed out that there should exist a comet reservoir between 20000 and 200000 AU from the Sun which contains around 10^{11} comets: the Oort cloud. The Oort cloud is the source of long period comet and its predicted spherical shape explains the isotropic distribution of inclinations of LP comets orbits (comet interaction with passing stars makes the orbit inclinations random). However, the Oort cloud theory faces serious problems in explaining the number of low inclination short period comets. Fernández and Ip (1981) proposed that short period comets come from another reservoir, located in the ecliptic plane beyond the orbit of Neptune. This reservoir is called Kuiper Belt and is supposed to contain around 10^8 to 10^{10} comets. The first Kuiper Belt Object (KBO) discovered was Pluto in 1930. However, originally it was classified as a planet and only later it was recognized as one of the largest member of the KBOs. Only in 1992 Jewitt and Luu (1993) discovered the first KBO which was recognized as such: (15760) 1992 QB₁. After than, over a thousand of similar objects have been discovered, confirming the prediction of Fernandez and Ip regarding the existence of a reservoir of objects beyond the orbit of Neptune.

A sketch of the Oort Cloud and the Kuiper Belt is shown in Fig. 1.5.

1.1 Physical properties of cometary nuclei

In the last two decades, spacecraft flew-by 6 comets: comet 21P/Giacobini-Zinner (International Cometary Explorer, 1985), comet 1P/Halley (Giotto, Vega 1, Vega 2, Suisei, Sakigake, 1986), comet 26P/Grigg-Skjellerup (Giotto, 1992), comet 19P/Borrelly (Deep Space 1, 2001), comet 81P/Wild 2 (Stardust, 2004) and comet 9P/Tempel 1 (Deep Impact, 2005). These fly-bys provided in-situ measurements of cometary nuclei and resolved images of four of the aforementioned comets: 1P/Halley, 19P/Borrelly, 81P/Wild 2 and

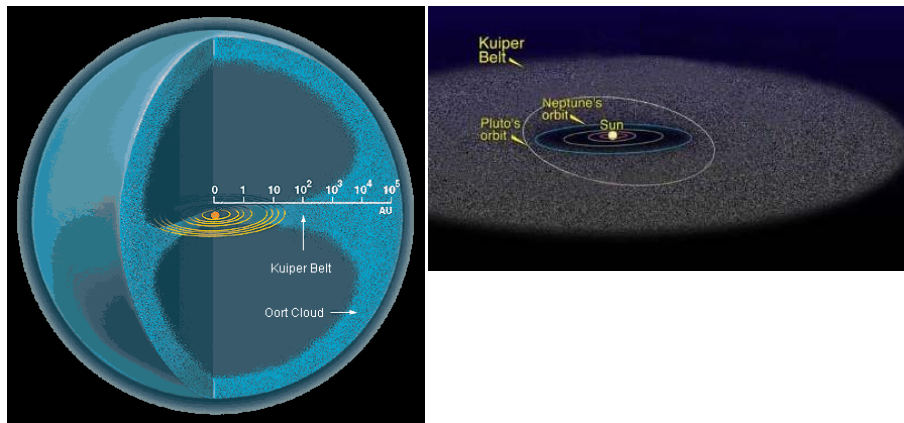


Figure 1.5: Sketch of the Oort cloud (left panel) and the Kuiper Belt (right panel). Images from: http://www.astro.rug.nl/~onderwys/ACTUEELONDERZOEK/JAAR2000/pluto/oort_cloud.gif and <http://www.enterprisemission.com/images/star-dust/image003.jpg>.

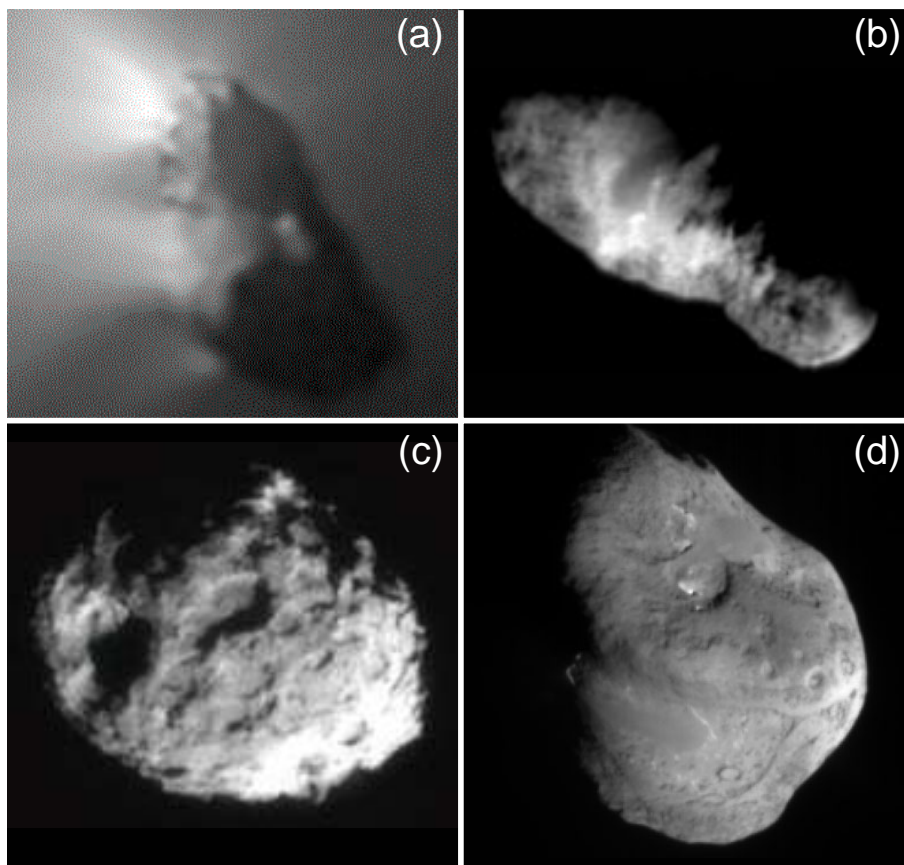


Figure 1.6: Spacecraft image of (a) comet 1P/Halley, (b) comet 19P/Borrelly, (c) comet 81P/Wild 2 and (d) comet 9P/Tempel 1.

9P/Tempel 1. The resolved images show that cometary nuclei can be very diverse (Fig. 1.6).

While spacecraft encounters are the best way to obtain detailed information about physical properties of cometary nuclei, this approach is limited to a small number of object and cannot be used to determine properties of cometary nuclei as a population. Ground- and space-based telescopes allow the study of a large number of cometary nuclei although not at the great details as spacecraft missions.

Cometary nuclei are certainly among the most difficult solar system object to detect and characterize since when comets are at small heliocentric distance their nuclei are surrounded by a coma and when comets are far away from the Sun and thus not active, cometary nuclei are faint. For illustration, Fig. 1.7 show the apparent magnitude of comets with different effective radii, observed at opposition ($\Delta = r - 1$, $\alpha = 0^\circ$ where r and Δ are heliocentric and geocentric distance, respectively, and α is the phase angle) at different heliocentric distances.

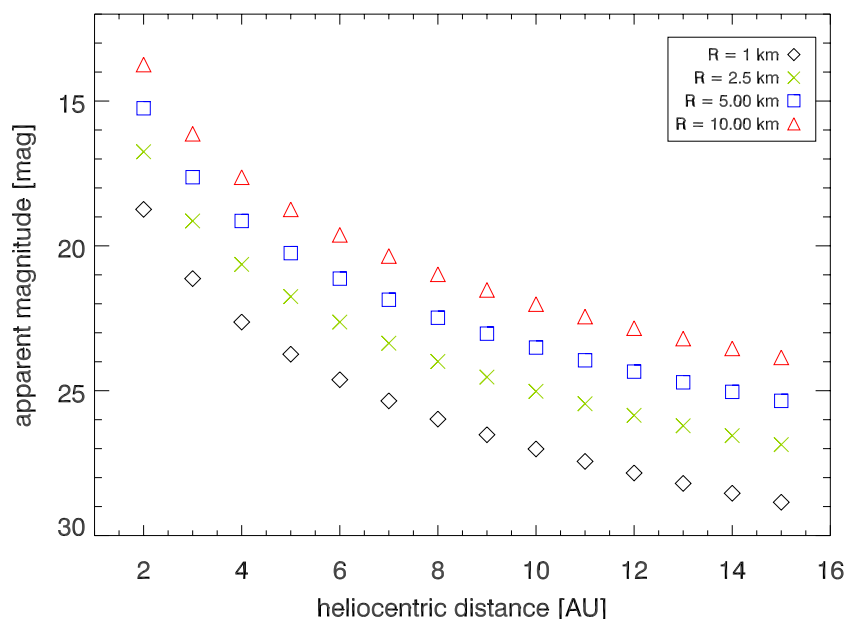


Figure 1.7: Apparent magnitude of comets with effective radii of 1 km, 2.5 km, 5 km and 10 km, observed at opposition at different heliocentric distances.

For remote observations, four techniques can be applied to detect and characterize cometary nuclei. The primary technique is visible wavelength imaging and spectroscopy, which uses the sunlight reflected by the nucleus and takes advantage of large telescopes (typically 3-10 m aperture) and very high-performance detectors like CCDs. This technique has been successfully used for nuclei at large heliocentric distance, where very low or no activity is detected, and for active comets observed with instruments with very high spatial resolution to separate the nucleus and coma signals (Lamy et al. 2004). A second technique relies on the detection of the thermal emission from the nucleus. The disadvantages with respect to the previously described technique are that generally the IR signal is much fainter than the visible one, using ground-based telescopes the thermal background is high, and the infrared detectors have much lower performance rather than CCDs. If a cometary nucleus is close or large, it can be detected through its thermal emission at radio wavelength. The number of nuclei which fulfill the requirements is very restricted. When

comets pass very close to the Earth, radar measurements of their nuclei can be performed (Lamy et al. 2004, and references therein). The limit of this technique is set by the fact that the radar signal scales as Δ^{-4} , where Δ is the geocentric distance.

Since our observations were performed in visible wavelength, in the following paragraphs we describe how a cometary nucleus can be characterized starting from its visible photometry and spectroscopy at large heliocentric distance.

1.1.1 Size and shape of a cometary nucleus

Ground- or space-based observations do not allow to determine directly size and shape of cometary nuclei, since due to their small dimension, they cannot be resolved, even with the largest telescopes available. Nevertheless, size and shape of a nucleus can be indirectly determined from photometric observations when the comet is at large heliocentric distance and thus not active (stellar appearance). When solar radiation impinges on the nucleus surface, part of the energy is reflected and part is absorbed. The reflected energy depends on the albedo of the nucleus. The absorbed energy gives rise to thermal emission and to the surface temperature which sublimates the material present in the nucleus. At large distance from the Sun the temperature of the nucleus is too low to allow sublimation of the ices from the nucleus (see Fig. 1.3). The observed radiation in the visible wavelength is the reflected sunlight and can be written as (Keller 1990):

$$F_c = \frac{F_\odot S A \phi(\alpha)}{r^2 \Delta^2 \pi 2.25 \cdot 10^{22}}, \quad (1.2)$$

where F_\odot is the solar flux at 1 AU, A the geometric albedo and $S = \pi R_{eff}^2$ [m²] the effective cross section of the nucleus, r [AU], Δ [AU] and $\phi(\alpha)$ are the heliocentric, geocentric distances and the value of the phase function of the comet at the time of the observation, respectively. Using the relation between flux and magnitude (magnitude = -2.5 log(flux)), from Eq. 1.2 we obtain the effective radius of the nucleus in km (Russell 1916):

$$R_{eff} = 1.496 \times 10^8 \sqrt{\frac{10^{0.4(M_\odot - H)}}{A}}, \quad (1.3)$$

where H and M_\odot are the absolute magnitude of the comet and of the Sun in the same wavelength (Lamy et al. 2004). The absolute magnitude $H = m(1,1,0)$ is the apparent magnitude of the comet nucleus scaled at heliocentric and geocentric distance of 1 AU and zero phase angle. The determination of the absolute magnitude is described in Sec. 3.5.3. The aforementioned equation requires the assumption of an albedo value. Nowadays, measurements of albedo exists only for a few comets and a canonic value $A = 0.04 \pm 0.02$ is generally assumed (Lamy et al. 2004).

If the spatial resolution of the imaging optics is adequate, even when the nucleus is active the coma contamination can be effectively subtracted to derive the flux contribution from the nucleus. Adequate spatial resolution means that the flux in the central pixel is dominated by scattered solar light from the nucleus. This technique has been applied for Hubble Space Telescope observations by Lamy and co-workers to determine the nuclear sizes of comets (Lamy et al. 2004). The brightness of an active comet is the sum of the coma and of the nucleus brightness, as sketched in Fig. 1.8 (left panel).

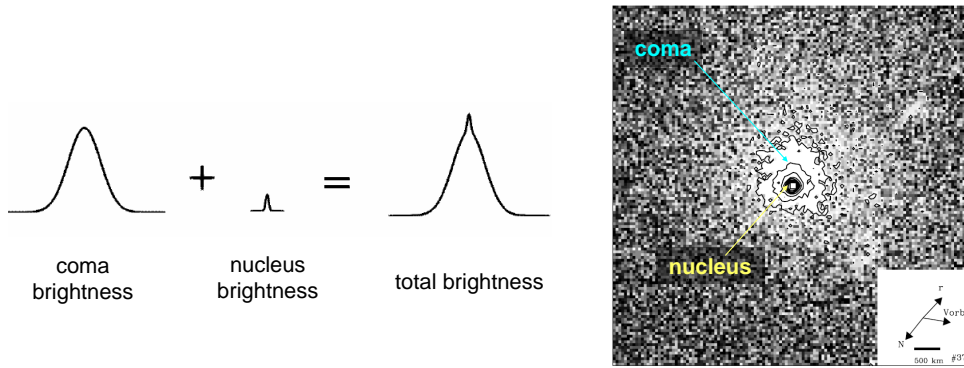


Figure 1.8: Left panel: schematic representation of the coma and nucleus profiles separately and their combination, which represents the brightness of an active comet (Figure adapted from Tancredi et al. (2000)). Right panel: Image of 67P/C-G obtained with the WFPC2 of the Hubble Space Telescope. The inner circular isophotes highlight the nucleus of the comet, while the outer ones indicate the coma. Figure adapted from Lamy et al. (2006).

Thus, the detection of an unresolved nucleus is matter of contrast of a point source (nucleus) against an extended object (coma), which is maximized when the comet is closest to the Earth. When the spatial resolution is very high, as for HST, while the nucleus signal is preserved in the point spread function of the telescope, the signal from the coma is diluted as the spatial resolution increases. Figure 1.8 (right panel) shows one image of 67P/C-G obtained with the WFPC2 of the Hubble Space Telescope by Lamy et al. (2006), when the comet was at 2.5 AU from the Sun and active. The inner circular isophotes highlight the nucleus of the comet, while the outer ones indicate the slightly asymmetric coma. The signal from the nucleus is estimated comparing the observed brightness distribution with a model for the surface brightness distribution for nucleus + coma (Lamy and Toth 1995). Lamy et al. (2006) model the brightness distribution of the comet as:

$$B(\rho) = [nucleus + coma] \otimes PSF, \quad (1.4)$$

where PSF is the point spread function of the telescope and \otimes is the convolution operator. Since the nucleus is not resolved:

$$nucleus = k_n \delta(\rho) \quad (1.5)$$

where ρ is the projected radial distance from the nucleus, $\delta(\rho)$ the Dirac delta function and k_n a scaling factor. $k_n PSF$ represents the nucleus brightness in absence of coma. In a canonical coma with a constant dust production rate, the surface brightness decreases as $1/\rho$. Lamy et al. (2006) adopt a simple isotropic model for the coma:

$$coma = k_c / \rho^p, \quad (1.6)$$

where k_c is a scaling factor for the coma and p the power exponent of the brightness versus distance from the nucleus. The scaling factor k_n and the parameters of the coma model (k_c , p , location of the nucleus) are determined minimizing the residuals between

the synthetic and the observed images.

Once the flux contribution from the nucleus of the comet has been determined, the effective radius of the cometary nucleus can be computed from Eq. 1.3.

If the radius is measured for a large sample of nuclei, the size distribution function can be calculated. The number of comets with radius greater than r_N can be approximated by a power law:

$$N(> r_N) \propto r_N^{-q} \quad (1.7)$$

The size distribution is an important marker of the history of cometary nuclei. If comets are collisional fragments of larger bodies they should have a distribution with $q = 2.5$ (Dohnanyi 1969). A theoretical work by O'Brien and Greenberg (2003) gives a wavy size distribution with an average $q = 2.04$ for the size range observed in comets. Comets, during their repeated passages through the inner part of the solar system, are subjected to mass loss (outgassing and splitting), which may significantly distort the size distribution of the nuclei. The very small number of small size cometary nuclei observed is very likely an observational bias, since small nuclei are very difficult to observe. Lowry et al. (2003) determined $q = 1.6 \pm 0.1$, Weissman and Lowry (2003) obtained $q = 1.59 \pm 0.03$ and Lamy et al. (2004) $q = 1.9 \pm 0.3$ (Fig. 1.9). All the aforementioned results imply either a non-collisional parent population or significant modification of the size distribution due to activity. Fernández et al. (1999), instead, determined $q = 2.65 \pm 0.25$.

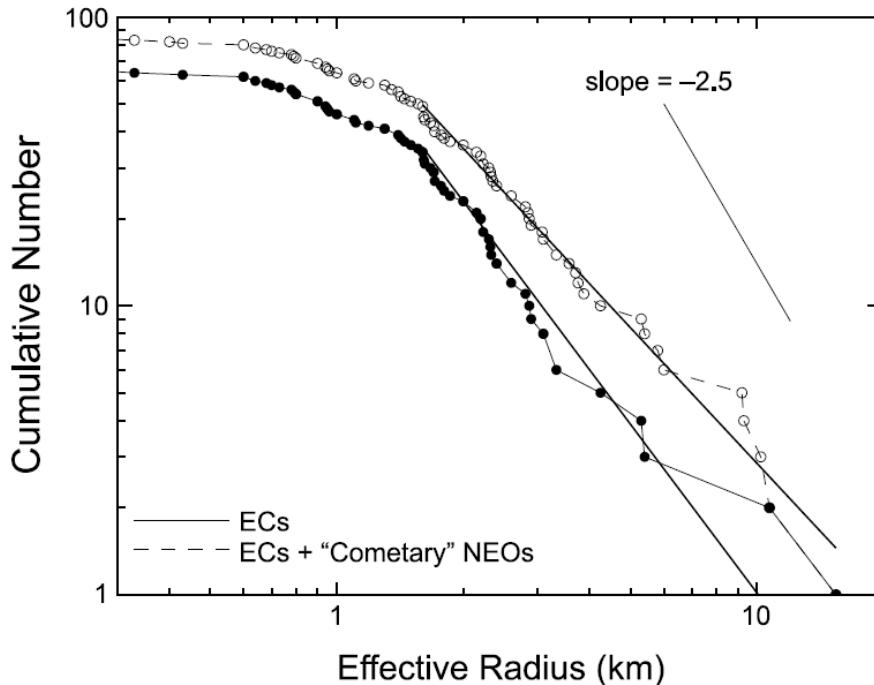


Figure 1.9: Cumulative size distribution for 65 ecliptic comets, as determined by Lamy et al. (2004). Figure adapted from Lamy et al. (2004).

We approximate the shape of a comet nucleus with a tri-axial ellipsoid having semi-

axis a and b and c , where $a > b$ and $b = c$ (Fig. 1.10), and we assume that the spin axis of the comet is perpendicular to the line of sight. The nuclear shape is describe by the axis-ratio a/b . If the second requirement is not fulfilled, we determine a lower limit for the axis-ratio of the nucleus.

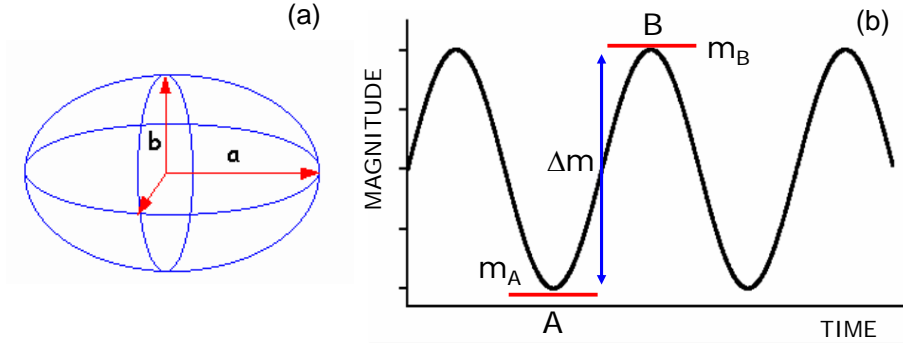


Figure 1.10: (a): tri-axial ellipsoid with semi-axis a and b and c , where $a > b$ and $b = c$; (b): light curve. A and B correspond to a minimum and a maximum of the light curve, respectively.

The amplitude Δm of the light curve can be due to 1) cross-section variations, assuming constant albedo of the nucleus or 2) large scale albedo variations, considering the cross-section constant or 3) a combination of cross-section and albedo variations. If only cross-section variations take place:

$$\frac{F_B}{F_A} = \frac{S_B}{S_A} = \frac{a}{b}, \quad (1.8)$$

where F_A and F_B are the reflected fluxes in A and B, respectively, $S_A = \pi b^2$ and $S_B = \pi ab$ are the cross-sections in A and B, respectively. Using the relation between flux and magnitude, Eq. 1.8 can be re-written as:

$$\frac{a}{b} = 10^{-0.4\Delta m}, \quad (1.9)$$

which expresses the shape of the comet (a/b) as function of the amplitude of the light curve (Δm).

If instead the magnitude variation is due to albedo variations (considering constant cross-section), in an analogue way we obtain:

$$\frac{A_B}{A_A} = 10^{-0.4\Delta m}, \quad (1.10)$$

which relates albedo variations with the amplitude of the light curve (Δm).

Generally, shape dominated light curves are double peaked, while the ones produced by albedo variations display a single peak.

Sizes have been determined for 65 ecliptic comets and their effective radii are in the range 0.2-15 km (Lamy et al. 2004) (Fig. 1.11). Although there are examples of highly elongated cometary nuclei, which display an axis ratio $a/b > 2$, most of the cometary

nuclei seem to differ from a spherical body by about 50%. In fact the distribution of lower limits of the axis ratio for ecliptic comets shows a median value of ~ 1.5 (Lamy et al. 2004) (Fig. 1.11).

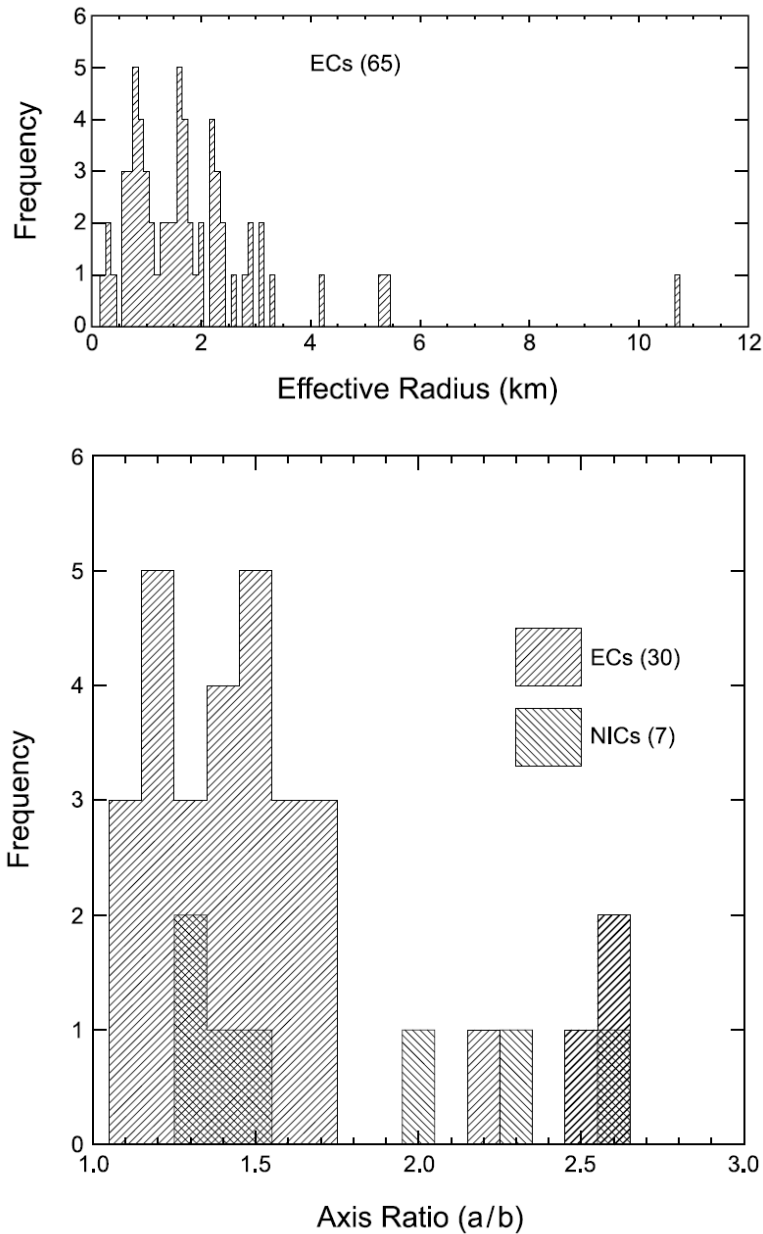


Figure 1.11: Distribution of the effective radii (top panel) and of the lower limit for the axis ratio (bottom panel) for ecliptic comets. Figure adapted from Lamy et al. (2004).

1.1.2 Rotational period of a cometary nucleus

First, we have to distinguish between sidereal and synodic rotational period. The sidereal rotational period is the time required to make a complete cycle of rotation around the fixed

axis of rotation as seen by an inertial observer (i.e. a distant star). It is independent from the Sun-comet-Earth geometry and any change of it. The synodic rotational period is the apparent rotational period of a comet that is moving relative to the observer. From now on, we refer to synodic rotational periods.

The rotational period of a cometary nucleus can be determined using well sampled rotational light curves or coma structures which display periodic variability. In general, the former method provides more precise determinations.

Rotational light curves. Rotational light curves of cometary nuclei can be obtained from 1) observations of bare nuclei when the comet is at large heliocentric distance or 2) observations of active comets if the spatial resolution is adequate to allow to effectively subtract the coma contamination and derive the flux contribution from the nucleus.

Extraction of periods from light curves can be achieved from different techniques (Samarasinha et al. 2004, and references therein), for instance the phase dispersion minimization and the χ^2 minimization using a sum of harmonics fitted to the observations. Both methods are described in Appendix D.

Repetitive coma structures. The time evolution of repetitive structures present in cometary comae (i.e. jets) can be used to determine the rotational period of the comet (Samarasinha et al. 2004, and references therein). Figure 1.12 shows three CN jets of comet 109P/Swift-Tuttle (Bönnhardt and Birkle 1994). The jet orientation changes with time and it has been used by Bönnhardt and Birkle (1994) to determine the rotational period of the comet.

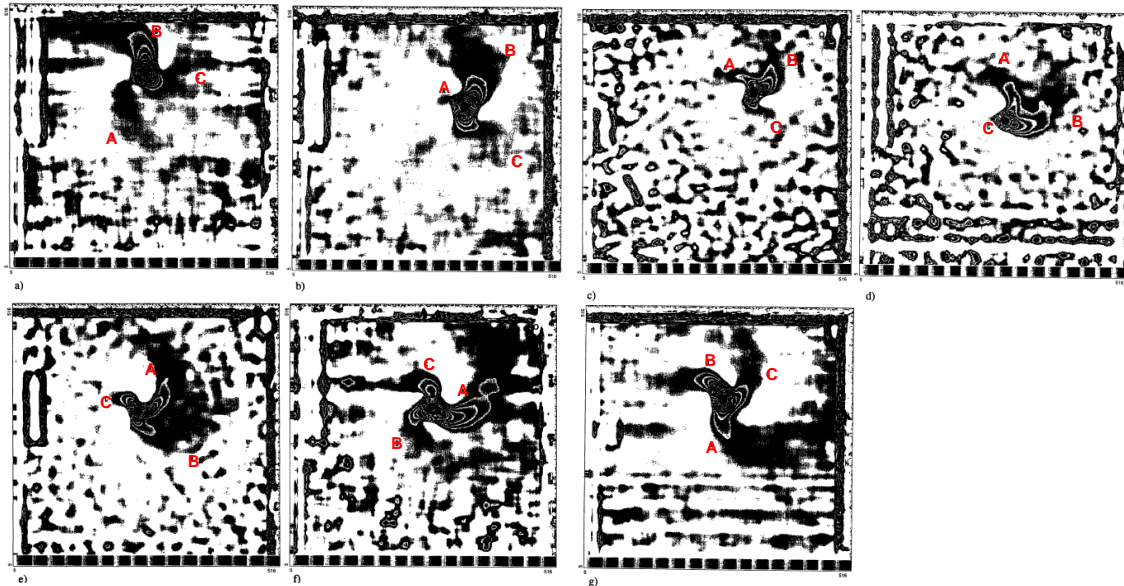


Figure 1.12: Variation in the orientation of the CN jets (A, B and C) of comet 109P/Swift-Tuttle with rotational phase. Figure adapted from Bönnhardt and Birkle (1994).

In conclusion, the most common technique to determine rotational period of cometary nuclei is to use their rotational light curve. Unfortunately most of the rotational periods are not accurately determined because of the scarcity of data points to define the light

curves. The range of rotational periods for ecliptic comets extends from 5 to 70 h and the bulk of the nuclei have period in a more restricted range, between 5 and 18 h (Lamy et al. 2004) (Fig. 1.13). However, most likely a bias towards short rotational periods exists, due to the difficulty in the measure of long rotational periods.

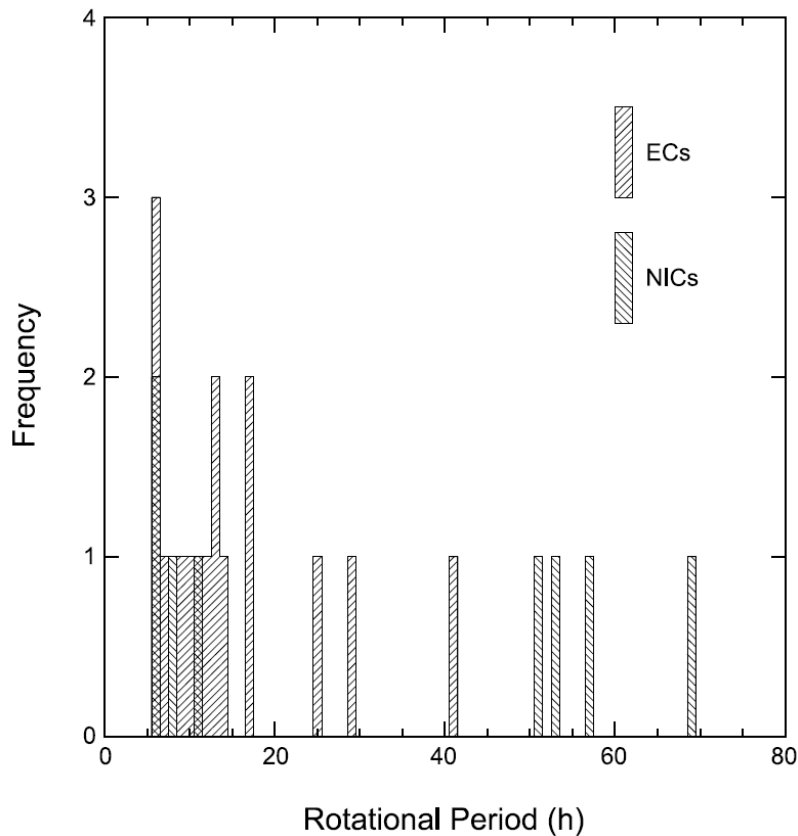


Figure 1.13: Distribution of the rotational periods for cometary nuclei. Figure from Lamy et al. (2004).

1.1.3 Albedo of cometary nuclei

Comets are among the darkest objects of the solar system. Albedo of cometary nuclei can be determined either from in-situ measurements, as in the case of comet 1P/Halley where a geometric albedo of $0.04^{+0.02}_{-0.01}$ was derived from Vega images (Keller et al. 2004) and comet 9P/Tempel 1 for which albedo variations are within 50% of an average of 0.04 (A'Hearn et al. 2005), or combining simultaneous observations in visible and IR, which allow to solve independently for radius and albedo of the nucleus. In fact, if sublimation is negligible, the energy balance on the isothermal nuclear surface can be written as:

$$\frac{F_{\odot} (1 - A)}{r^2} \pi R_{eff}^2 = \sigma T_e^4 \cdot k \pi R_{eff}^2 \quad (1.11)$$

where F_{\odot} is the solar flux at 1 AU, A the geometric albedo and R_{eff} the effective radius of the nucleus and T_e its effective temperature, r is the heliocentric distance. $k = 4$ for a fast

rotating nucleus and $k = 2$ for a slow rotating nucleus. The left-hand side of the equation is the energy which is reflected by the nuclear surface in visible wavelength and the right-hand side the energy which is instead irradiated in IR. Both quantities can be measured through simultaneous observations in the visible and IR. Unfortunately, the unknowns in Eq. 1.11 are 3: the albedo of the nucleus, its effective radius and its effective temperature. Thus, to use this method to determine the albedo of a comet, simultaneous observations in the two wavelength regions have to be complemented by the determination of the effective temperature of the cometary nucleus with a model.

The described technique has been applied e.g. to the determination of the albedo of comet 67P/C-G which resulted to be 0.044 in R band (Lamy et al. 2004b).

The geometric albedo has been measured only for a small number of comets. Based on the available values, the range of albedos is narrow, from 0.02 to 0.06 (Lamy et al. 2004). A canonical value of 0.04 ± 0.02 is usually assumed for Jupiter family comets, which corresponds to the average of the measured albedos.

1.1.4 Bulk density of cometary nuclei

The bulk density is one of the most uncertain, yet important, physical properties of a cometary nucleus. It can give information about the structure of the nucleus. The bulk density can be estimated provided the mass and the volume of the nucleus are known; unfortunately, the aforementioned quantities are difficult to determine. Several methods can be used for constraining the mass or bulk density of cometary nuclei. Among others, ground-based Doppler tracking of a spacecraft flying-by or orbiting a nucleus, observations and modelling of breakup of cometary nuclei, the need of a body to have a certain self-gravity and material strength in order to resist to the centrifugal force due to rotation and time lags between the predicted and the observed perihelion passages, caused by non-gravitational forces due to nucleus sublimation and outgassing. The general conclusion is that the results appear to indicate a low value for the bulk density of cometary nuclei, suggesting that the nucleus could be fluffy and a loosely packed structure (Swamy 1996). For comet 9P/Tempel 1 a bulk density of about 350 kg/m^3 has been estimated (A'Hearn and Combi 2007).

1.1.5 Colors indices and spectra of the nucleus

Information on the surface compositions of cometary nuclei can be inferred studying how their reflectance varies at different wavelengths. The most complete compositional information comes from spectroscopy. While it is regularly used in observations of active comets (to study the gases and the dust present in the coma or tail), it is just rarely employed in studies of bare nuclei: due to the faintness of the nuclei, it is very difficult to obtain a good signal-to-noise ratio. To overcome this problem, big telescopes have to be employed. Luu (1993) obtained CCD spectra of five nuclei at large heliocentric distance, where they are expected to be inactive. The spectra do not show any absorption or emission feature and display a fairly constant gradient in the whole wavelength range considered (Fig. 1.14).

A color index is defined as the difference between magnitudes of an object at two specific wavelengths. The color indices can also be converted into relative spectral reflec-

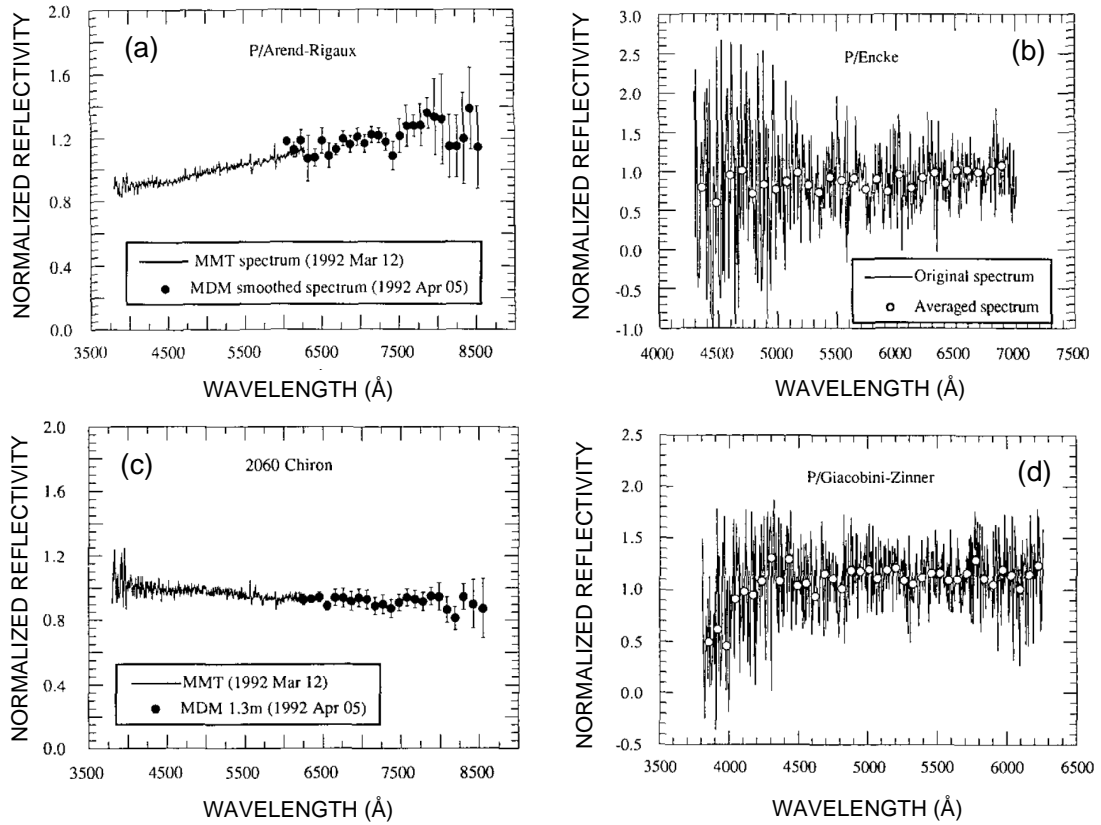


Figure 1.14: Visible spectra of cometary nuclei at large heliocentric distance, as observed by Luu (1993). The spectra do not show any absorption or emission feature and display a fairly constant gradient in the wavelength range considered. Figure adapted from Luu (1993).

tivities computed at the central wavelength of the broadband filter used (Delsanti et al. 2001):

$$R(\lambda) = 10^{-0.4[(color)_{comet} - (color)_{\odot}]} \quad (1.12)$$

where $(color)_{comet}$ is the color of the comet and $(color)_{\odot}$ the corresponding color of the Sun. Thus, color indices are equivalent to very low resolution spectra. Both from color indices and from spectra the reflectivity gradient can be determined. It is the rate of change of reflectivity with respect to the wavelength in the considered wavelength range (Delsanti et al. 2001):

$$S(\lambda_1, \lambda_2) = 100 \times \frac{R(\lambda_2) - R(\lambda_1)}{(\lambda_1 - \lambda_2)/1000} \quad (1.13)$$

The reflectivity gradient is measured in $\% / 1000 \text{ \AA}$.

Lamy et al. (2004) obtained that cometary nuclei are statistically redder than the Sun, with mean value of the color indices $\langle V-R \rangle = 0.42 \text{ mag}$, $\langle R-I \rangle = 0.38 \text{ mag}$ and $\langle B-V \rangle = 0.82 \text{ mag}$ (Fig. 1.15). For comparison, the solar colors are: $(V-R)_{\odot} = 0.36 \text{ mag}$, $(R-I)_{\odot} = 0.33 \text{ mag}$ and $(B-V)_{\odot} = 0.67 \text{ mag}$. The individual colors, however, are very diverse

ranging from slightly blue to very red, as obtained also from spectra by Luu (1993), who measured normalized reflectivity gradients in the range from $-3 \text{ \%}/1000 \text{ \AA}$ to $20 \text{ \%}/1000 \text{ \AA}$. Jewitt (2002) obtained for cometary nuclei a mean spectral reddening of $8.3 \pm 2.8 \text{ \%}/1000 \text{ \AA}$, which corresponds to $V-R = 0.45 \pm 0.02 \text{ mag}$.

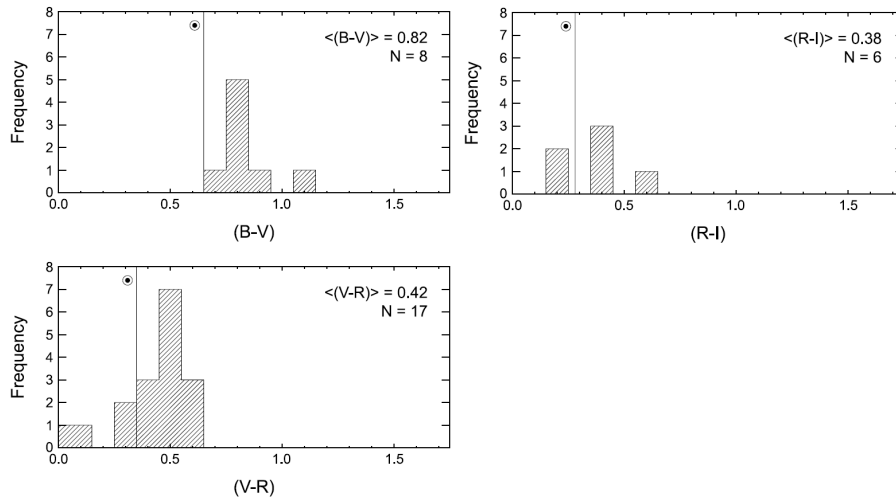


Figure 1.15: Distribution of the B-V, V-R and R-I color indices for ecliptic comets. Figure from Lamy et al. (2004).

1.2 Dust trail and neck-line

Cometary nuclei release dust particles with very diverse sizes, ranging from 10^{-6} m or less to 10^{-1} m . While small particles are blown away from the comet into the tail region by solar radiation pressure, large dust grains, ejected at low velocities (perhaps m/s), generally remain close to the orbit of the comet for many revolutions around the Sun and form the dust trail. Due to their non-zero ejection velocities, large dust grains slowly drift away from the comet orbit due to slow changes in their orbits caused by radiation pressure forces. Cometary trails were observed for the first time in 1983, when the first survey of the entire sky at thermal infrared wavelength was conducted by IRAS (Sykes et al. 2004, and references therein).

When the Earth crosses a comet trail orbit, the large dust grains enter the atmosphere at high speed, are heated by friction to high temperatures and vaporizing the material, give rise to visible meteors. Because of the high concentration of dust grains in the orbit, many of them enter the atmosphere at the same time, producing meteor showers. Two of the most famous meteor showers are the Perseids and the Leonids, associated to comet 109P/Swift-Tuttle and 55P/Tempel-Tuttle, respectively. Meteor showers often show variations of magnitude from year to year. The peak magnitude is usually near or soon after the time of perihelion passage of the parent comet. For example the Leonid meteor shower peaks every 33 years, which corresponds to the orbital period of 55P/Tempel-Tuttle.

The concept of neck-lines was introduced by Kimura and Liu (1977). The orbit of dust grains emitted by the comet nucleus is determined by the starting velocity of the dust and

β , defined as the ratio between the solar gravity and the radiation pressure force. In non-relativistic approximation β depends only on the material properties of the dust grains and not on their distance from the Sun. Dust grains ejected in all directions at the same time, with the same β and with the same velocity form a spherical shell expanding in space (Fig. 1.16).

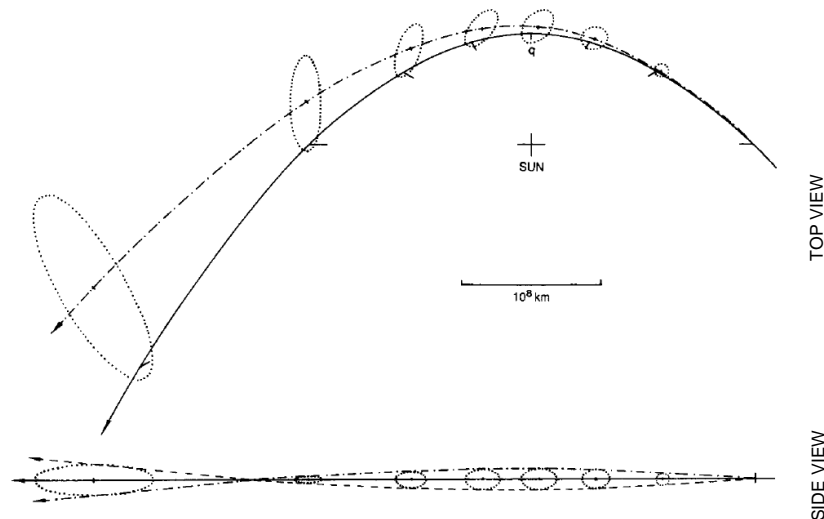


Figure 1.16: Evolution of a dust shell emitted with positive velocity. The solid line is the orbit of the comet nucleus and the dotted and dashed-dotted lines are the orbits of the dust grains ejected perpendicular to the comet orbital plane. Top panel: line of sight perpendicular to the comet orbital plane. Bottom panel: line of sight parallel to the comet orbital plane. Figure adapted from Fulle and Sedmak (1988).

Dust grains composing the spherical shells have heliocentric orbits similar to the one of the parent comet, and in general inclined with respect to it. The orbital plane of the comet and the one of the dust grains intersect one another along the nodal line crossing the Sun. The first node is the location of dust emission and the second one is at true anomaly of 180° after ejection along the orbit of the dust grains. Monte Carlo simulations by Fulle and Sedmak (1988) showed that at true anomaly of 180° after ejection the dust shell can be approximated by an ellipsoid, whose two main axes in the comet orbital plane are orders of magnitude longer than the axis perpendicular to the comet orbital plane. Thus, the ellipsoid can be approximated by a 2D ellipse laying on the comet orbital plane. The expansion and shrink of the dust shell takes place only in the direction perpendicular to the orbital plane, while the shell is always expanding in the orbital plane. The position of the second intersection point on the line of nodes depends on the semi-major axis of the particle orbit. Since the orbital periods are less sensitive to small changes of orbital energy than the semi-major axis, large particles emitted at a given time cross the orbital plane of the comet almost simultaneously but at different positions along the nodal line. To an observer in or close to the orbital plane of the comet, they appear as a bright line: the neck-line (Agarwal 2007).

2 67P/Churyumov-Gerasimenko and the ESA's ROSETTA mission

After the success of the Giotto mission to comet 1P/Halley, the European Space Agency (ESA) approved in the early nineties a new space mission with a comet as main target: ROSETTA, which will rendezvous with the Jupiter family comet 67P/Churyumov-Gerasimenko (67P/C-G) in 2014. ROSETTA will be the first spacecraft to orbit a comet's nucleus and to land on it. What makes this mission exceptional is that the spacecraft will follow the comet in its journey towards the Sun, examining how a frozen comet is transformed by solar heating and space weathering. In 2003, due to a delay in the launch of the ROSETTA spacecraft, on the basis of orbital considerations, 67P/C-G was chosen as the most suitable alternative to the original target, 46P/Wirtanen, even though very little was known at that time about this comet and the physical properties of its nucleus. Since then observational campaigns and theoretical investigations were performed in order to establish a detailed portrait of 67P/C-G in preparation of the rendezvous with the spacecraft. Thanks to space- and ground-based observations performed around perihelion in different wavelength regions, a detailed portrait of 67P/C-G has been drawn (see Agarwal et al. 2007, Hansen et al. 2007, Lamy et al. 2007). What needs to be enhanced in this picture of the ROSETTA target is a profound description of the comet's behaviour at large heliocentric distances, where the rendezvous between the ROSETTA spacecraft and 67P/C-G will take place. This information will also help to identify to which extent 67P/C-G is a typical JFC.

Here on, we summarize published results about 67P/C-G, which will be used as comparison with our results in Chapter 5.

2.1 Discovery and orbital evolution

67P/Churyumov-Gerasimenko is a Jupiter family comet with Tisserand parameter with respect to Jupiter $T_J = 2.75$, orbital period of 6.56 years and orbital elements listed in Table 2.1 (Lamy et al. 2007).

Due to repeated close encounters with Jupiter, the orbital evolution of 67P/C-G is chaotic. The last encounter in February 1959 occurred at a distance of only 0.0518 AU and produced a drastic change in the orbit of 67P/C-G. In fact its perihelion distance dropped from 2.76 AU to 1.29 AU, the eccentricity of the orbit increased from 0.36 to 0.63, the inclination decreased from 23.15° to 7.13° and the orbital period of 67P/C-G shortened from 9.00 y to 6.55 y (Belyaev et al. 1986). It is speculated that this drastic change may have triggered the activity of the comet, which most likely led to its discovery in 1969 by

orbital element	value
Eccentricity	0.63
Inclination	7.13°
Longitude of ascending node	50.92°
Argument of perihelion	11.37°
Semi-major axis	3.50 AU
Perihelion distance	1.29 AU
Aphelion distance	5.72 AU
Time of perihelion passage	2002 Aug 18.24

Table 2.1: Orbital elements of comet 67P/C-G for the epoch 23.0 August 2004 in the coordinate system given by the ecliptic and the mean equinox of J2000. The values are taken from Lamy et al. (2007).

K. I. Churyumov and S. I. Gerasimenko (Lamy et al. 2007).

2.2 Nucleus properties

Information about the nuclear properties of 67P/C-G has been obtained thanks to observations performed on March 12-13, 2003 using the Planetary Camera 2 onboard the Hubble Space Telescope (HST) (Lamy et al. 2006) and on May 10, 12 and 14, 2005 using the ESO's 3.5m New Technology Telescope (NTT) at La Silla, Chile (Lowry et al. 2006). While at the time of the first observation 67P/C-G was at heliocentric distance of about 2.52 AU and active, in the other epoch the comet was at about 5.6 AU from the Sun and there were no sign of coma outgassing. The main results obtained from the aforementioned observations are reported in Lamy et al. (2007) and summarized in Table 2.2.

	R_{eff} [km]	a/b	T_{rot} [h]	V-R (mag)	reference
HST	1.98 ± 0.02	≥ 1.5	12.41 ± 0.41	0.52 ± 0.05	Lamy et al. (2006)
NTT	2.26 ± 0.03	$\geq 1.42 \pm 0.05$	12.72 ± 0.05	0.41 ± 0.04	Lowry et al. (2006)

Table 2.2: Physical properties of the nucleus of 67P/C-G as obtained by Lamy et al. (2006) and Lowry et al. (2006) thanks to observations performed with HST and NTT, respectively.

The light curves derived from HST and NTT observations are highly asymmetric and the difference in amplitude suggests that the nucleus was observed at different aspect angles. Lamy et al. (2007) attempt to determine the phase function of the nucleus of 67P/C-G combining HST and NTT observations, even though they stated that, due to the orbital motion of the comet, changes of observing geometry might have occurred. They suggest a strong opposition effect for 67P/C-G and determine a slope parameter $G = -0.45$.

For the determination of the orientation of the nucleus rotational axis various methods can be used, such as the inversion of at least three light curves of the nucleus observed at three different viewing geometries, the analysis of coma structures or non-gravitational

forces or thermophysical models. Lamy et al. (2007) applied the inversion technique to the HST and NTT light curves of 67P/C-G. Even though the constraint on the number of light curves employed was not fulfilled, the inversion yielded a useful constraint on the rotational axis orientation. They obtained two possible solutions: $\lambda = 51^\circ \pm 20^\circ$, $\beta = +54^\circ \pm 10^\circ$ corresponding to a prograde rotation and $\lambda = 245^\circ \pm 20^\circ$, $\beta = -50^\circ \pm 10^\circ$ corresponding to a retrograde rotation. The existence of two solutions is due to the too small number of light curves used.

Weiler et al. (2004), using images of 67P/C-G taken in March 2003, identified two radial structures in the coma of the comet which were interpreted as the edge of a cone originated by a single active region present on the rotating nucleus. From the position angle of this structure Weiler et al. (2004) estimated that the inclination of the projected rotational axis to the orbital plane was about 40° . A strong sunward radial feature in the coma of 67P/C-G was detected by Schleicher (2006) in images obtained in January 1996. He explained this structure as the edge of a cone swept out by the rotation of a jet from a single active region. Using Monte Carlo simulations of this jet and imposing the constraint on the inclination given by Weiler et al. (2004), he determined that the best solutions for the rotational axis are: RA $\sim 57^\circ$, DEC $\sim +65$ or RA $\sim 223^\circ$, DEC ~ -65 , since the sense of rotation is not constrained.

Chesley (2004) modelled the non-gravitational acceleration as outgassing from body-fixed jets that thrust according to the level of insolation received. He assumed a near-polar northern jet or a mid-latitude southern jet responsible for the post-perihelion activity of 67P/C-G. Images of the comet from Weiler et al. (2004) constraint the jet location: in fact, images are not consistent with a polar jet, while a good agreement exists with the predicted orientation and width of a mid-latitude jet. The estimation of the pole orientation of 67P/C-G is: RA = $90^\circ \pm 10^\circ$ and DEC = $+75^\circ \pm 10^\circ$ (with no constraint on the sense or rotation), which implies an obliquity around 45° .

Davidsson and Gutiérrez (2005), using a thermophysical model and imposing observational constraints (i.e. the water production rate measurements have to be reproduced), determined that the spin axis of 67P/C-G can be confined in two regions in the (argument, obliquity) plane (Sekanina 1981): $(60^\circ \pm 15^\circ, 120^\circ \pm 30^\circ)$ or $(240^\circ \pm 15^\circ, 60^\circ \pm 30^\circ)$.

Lamy et al. (2007) defined the direction of the rotational axis of the nucleus of 67P/C-G using as constraints the determinations by Weiler et al. (2004), Schleicher (2006), Chesley (2004), Davidsson and Gutiérrez (2005) and Lamy et al. (2007): RA = $220^\circ_{-30^\circ}^{+50^\circ}$ and DEC = $-70^\circ \pm 10^\circ$ (retrograde rotation) or RA = $40^\circ_{-30^\circ}^{+50^\circ}$ and DEC = $+70^\circ \pm 10^\circ$ (prograde rotation).

The bulk density of cometary nuclei is believed to be rather low, typically 500 kg/m^3 . Davidsson and Gutiérrez (2005) calculated for the nucleus of 67P/C-G a density range from 100 to 370 kg/m^3 . The mass of 67P/C-G is therefore estimated to be in the range 2.1×10^{12} - $1.1 \times 10^{13} \text{ kg}$ (Lamy et al. 2007).

Thermal infrared images of 67P/C-G were obtained with the MIPS instrument onboard the Spitzer Space Telescope on February 25, 2004 when the comet was at heliocentric distance of 4.48 AU (Lamy et al. 2007). Lamy et al. (2004b) combined the HST visible images and the aforementioned thermal infrared ones and they determined an albedo of 0.044 (in R band) for 67P/C-G.

2.3 Annual light curve

Weiler et al. (2004) compared the annual light curves of 67P/C-G relative to the last three perihelion passages (Fig. 2.1).

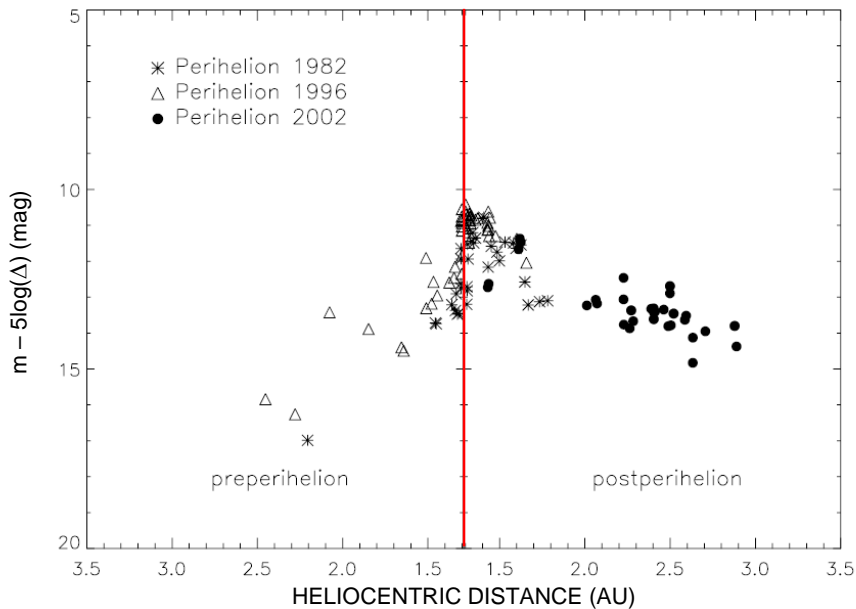


Figure 2.1: Annual light curve of 67P/C-G relative to the 1982/83, 1995/96 and 2002/03 apparitions. The apparent magnitude, corrected for changing geocentric distance, is plotted versus the heliocentric distance. Figure adapted from Weiler et al. (2004).

A similar dependence of activity from heliocentric distance is observed in the 1982/83, 1995/96 and 2002/03 apparitions, with a higher post- rather than pre-perihelion activity. A possible conclusion is that no significant changes of activity of 67P/C-G during the last orbital passages took place.

2.4 Gas and dust production

Gas and dust production rates have been determined for 67P/C-G during the 1982/83, 1995/96 and 2002/03 apparitions (see i.e. Hanner et al. 1985, A'Hearn et al. 1995, Osip et al. 1992, Schleicher 2006, Schulz et al. 2004, Weiler et al. 2004, Agarwal 2007). All species present a pronounced perihelion asymmetry in the production rates, with a peak about one month after perihelion (Fig. 2.2).

Schleicher (2006) measured a peak water production of $\sim 8 \times 10^{27}$ mol/s one month after perihelion at ~ 1.35 AU. When combined with a standard water vaporization model, the aforementioned production rate implies an effective active area on the nuclear surface of about $1.5 - 2.2$ km². Assuming that the radius of the nucleus of 67P/C-G is 1.98 ± 0.02 km (Lamy et al. 2006) the effective active area corresponds to a fraction of about 3 - 4% of the nucleus surface. In a similar way, based on water production rate of 67P/C-G

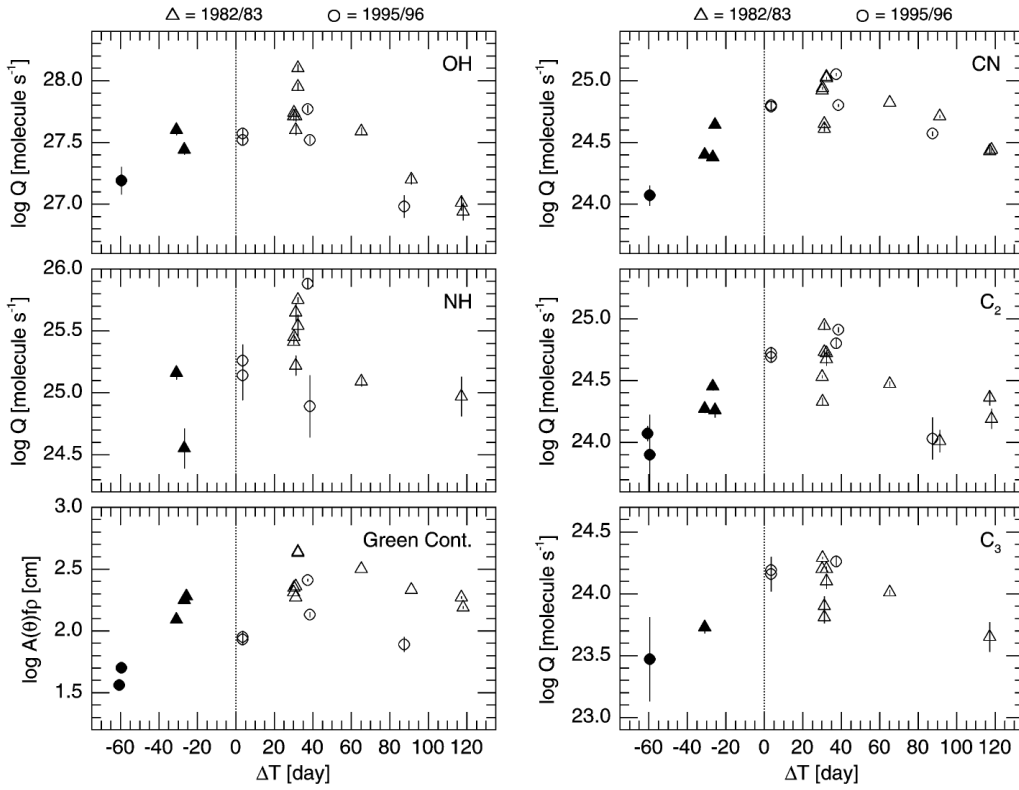


Figure 2.2: Log of the production rates for OH, NH, CN, C₂, C₃ and of $Af\rho$ as function of the time from perihelion, for the 1982/83 apparition (triangles) and the 1995/96 one (circles). Filled symbols represent data obtained before perihelion and open symbols are used for post-perihelion measurements. The dotted vertical line represents the perihelion position. Figure from Schleicher (2006).

at 1.41 AU, A'Hearn et al. (1995) estimated an active area of the nucleus of 1.3 km², yielding an active fraction of 2.6%. Schleicher (2006) observed a dependence of $Af\rho$ (A'Hearn et al. 1984) on the employed aperture size; moreover, he determined $Af\rho \sim 450$ cm at 1.35 AU post-perihelion, a red color of the dust grains (reddening slope 30 ± 42 %/1000 Å) and no obvious variations of dust color with location in the coma. $Af\rho$ is the product of grain albedo (A), filling factor (\equiv mean cross section of the particles per aperture surface area, f) and aperture radius (ρ). It is a proxy of the dust production. Lamy et al. (2006), with observations of 67P/C-G performed at 2.5 AU post-perihelion in the 2002/03 apparition, determined $Af\rho = 40.2 \pm 0.3$ cm. Moreover they determined that the dust grains of 67P/C-G are quite red, with a reddening slope of 32 ± 6 %/1000 Å. From spectroscopic observations Storrs et al. (1992) determined a reflectivity gradient of 24 ± 1 %/1000 Å, while Weiler et al. (2004) obtained -0.7 ± 5.1 %/1000 Å.

A 3- σ upper limit for the CO production rate of 9.2×10^{26} mol/s at 3 AU from the Sun has been derived from radio observations (Bockelée-Morvan et al. 2004). From longslit spectra obtained during the perihelion passage of 67P/C-G in 1996 Weiler et al. (2004) determined a CN production rate of $(1.35 \pm 0.35) \times 10^{25}$ mol/s, an upper limit for the C₃ production rate of 1×10^{25} mol/s and $Af\rho = 428.2 \pm 59.8$ cm at ~ 1.3 AU post-perihelion. The CN production rate and the $Af\rho$ parameter are similar to the values determined in

the 1982 perihelion passage. This might indicate that the activity of 67P/C-G did not change significantly during the last orbital revolutions. The strong perihelion asymmetry, observed in both gas and dust productions during the 1982/83 and 1995/96 apparitions, may result from an inclination of the rotational axis with respect to the orbital plane. In fact, if the rotational axis is inclined, the illumination of parts of the nuclear surface can vary strongly along the orbit of 67P/C-G (Weiler et al. 2004).

Schulz et al. (2004) studied the activity of 67P/C-G during the 2002/03 apparition, when the comet was along its post-perihelion orbit from 2.29 AU to 3.22 AU. They detect a major drop of activity between 2.5 AU and 2.9 AU and a continued fading with increasing heliocentric distance, but at much lower pace (Fig. 2.3).

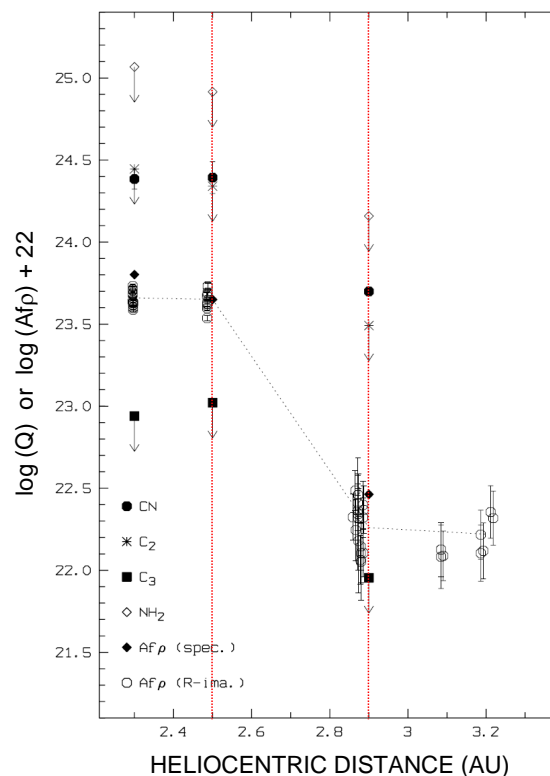


Figure 2.3: Post-perihelion activity of 67P/C-G during the 2002/03 apparition. Gas production rates and $Af\rho$ are plotted versus heliocentric distance. The red vertical lines mark the heliocentric distances of 2.5 AU and 2.9 AU. Figure adapted from Schulz et al. (2004).

The CN production rate decreased by a factor 4.8 between 2.5 AU and 2.9 AU, while the decrease of $Af\rho$ was of a factor 21. In fact the production rate of CN changed from $(24.2 \pm 3.4) \times 10^{23}$ mol/s to $(5.0 \pm 0.3) \times 10^{23}$ mol/s and $Af\rho$ from 63.1 ± 1.3 cm to 2.9 ± 0.1 cm. The strong activity decrease indicates a major change in the outgassing behaviour of the nucleus at heliocentric distance between 2.5 AU and 2.9 AU, and might be due to water sublimation becoming less efficient (Schulz et al. 2004).

Observations obtained during the comet's apparition in 1982/83 showed that the coma of 67P/C-G was depleted in C_2 with respect to CN ($C_2/CN \approx 0.49$) at a heliocentric distance of 1.4 AU (A'Hearn et al. 1995). The same depletion was also measured by Schulz et al. (2004) during the 2002/03 apparition at 2.9 AU post-perihelion ($C_2/CN < 0.62$).

2.5 Coma features, trail and neck-line

The coma of 67P/C-G displayed distinct features during both 1995/96 and 2002/03 apparitions. These features have been interpreted as border lines of coma fans produced by active areas at different latitudes on the rotating nucleus (Agarwal et al. 2007, and references therein).

Between perihelion in August 2002 and at least April 2004, the tail of 67P/C-G was characterized by a thin bright spike close to the orbit of the comet pointing in the trailing direction. Fulle et al. (2004) and Moreno et al. (2004) interpreted this structure as a neck-line (Kimura and Liu 1977).

The dust trail of 67P/C-G was observed for the first time in the IR by the Infrared Astronomical Satellite (IRAS) in 1983 (Sykes et al. 1986a, Sykes and Walker 1992, Sykes et al. 1986b). The first observation of the trail in the visible wavelength was performed by Ishiguro (2008), using images obtained between September 2002 and February 2003.

Agarwal (2007) detected the trail of 67P/C-G in visible observations performed in April 2004 and in IR observations (using Spitzer) performed in August 2005 and April 2006. In the April 2004 image, a split of the trail is seen beyond 17' from the nucleus (Fig. 2.4).

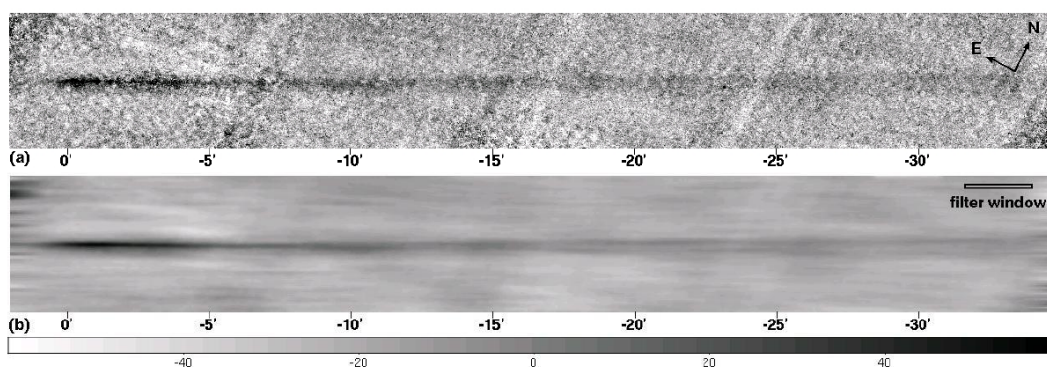


Figure 2.4: Image of 67P/C-G obtained in April 2004 before (a) and after (b) filtering to increase the signal-to-noise ratio is applied. The image size is $35' \times 4.7'$, the orientation of the images is indicated and the brightness range is ADU is shown by the colorbar. A split of the trail is seen beyond 17' from the nucleus. Image by courtesy of J. Agarwal (Agarwal 2007).

Thanks to simulations, the upper and the lower branches are interpreted as due to particles emitted during the last apparition of the comet (neck-line) and previous apparitions (old trail), respectively. The trail split was instead not detected in IR images (Agarwal 2007). Kelley et al. (2008) reported the detection of the dust trail and neck-line of 67P/C-G in images taken in February 2004 with the Spitzer Space Telescope. Additionally, the neck-line was detected also in visible images taken in June 2003.

2.6 ESA's ROSETTA mission

ROSETTA is the planetary cornerstone mission in ESA's long-term program Horizon 2000. Its primary objective is to investigate the origin of our Solar System by studying

the origins of comets. The mission is named after the Rosetta stone, a volcanic basalt plate which allowed to understand hieroglyphic writing and thus unravel the civilization of ancient Egypt. In fact, the scientific instruments onboard the ROSETTA spacecraft are designed to unlock the mysteries of comets, the oldest building blocks of our Solar System (Glassmeier et al. 2007, and references therein). ROSETTA was launched on March 2, 2004 from the Guyana Space Center in Kourou, French Guyana and it will rendezvous with the comet 67P/Churyumov-Gerasimenko in 2014, when 67P/C-G will be at about 4.5 AU from the Sun.

The main goals of the ROSETTA mission are: 1) a global characterization of the nucleus of 67P/C-G, its dynamical properties, surface morphology and composition; 2) the study of the development of cometary activity and of the processes in the surface layers of the nucleus and inner coma, and 3) the study of the evolution of the interaction region between the solar wind and the outgassing comet during perihelion approach (Schwehm and Schulz 1999). The ROSETTA spacecraft consists of two parts, an orbiter and a lander and it is comprised of 22 experiments. To characterize the properties of the cometary nucleus, ROSETTA combines two strategies. The orbiter instruments will investigate the evolution of 67P/C-G along its orbit while it is approaching the Sun, by monitoring the physical and chemical properties of the nucleus and in-situ analysis of the near-nucleus environment. The lander will analyse the nucleus material directly. Figure 2.5 shows a sketch of the ROSETTA spacecraft and its scientific payload.

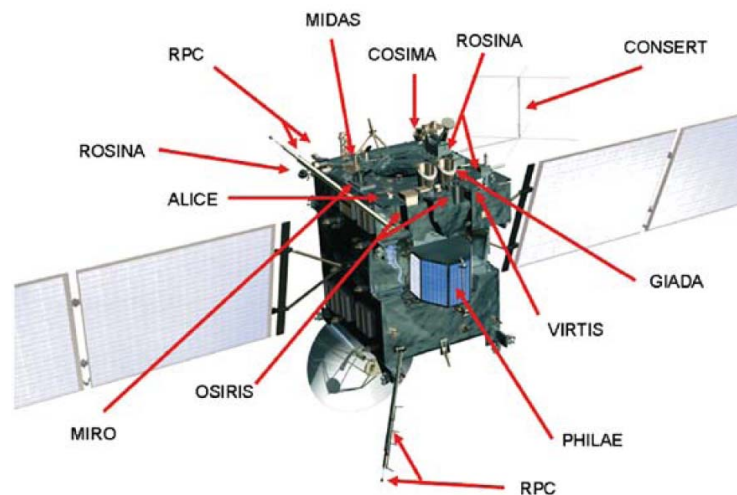


Figure 2.5: Sketch of the ROSETTA spacecraft and its scientific payload. Figure from Glassmeier et al. (2007).

The orbiter's scientific payload includes 12 experiments (Glassmeier et al. 2007):

- ALICE: ultraviolet imaging spectrometer which will analyse gases in the coma and in the tail and measure the comet's production rates of water and CO or CO₂. It will also provide information of the surface composition of the nucleus.

- **CONCERT**: comet nucleus radiowave sounding experiment, which will probe the nucleus interior by studying radio waves that will penetrate the nucleus.
- **COSIMA**: a secondary ion mass spectrometer which will analyse the characteristics of the dust grains emitted by the comet, such as their composition and whether they are organic or inorganic.
- **GIADA**: grain impact analyser and dust accumulator, which will measure the number, mass, momentum and velocity distribution of the dust grains coming from the comet nucleus.
- **MIDAS**: micro-imaging dust analysis system, which will study the dust environment around the comet and provide information on particle population, size, volume and shape.
- **MIRO**: microwave instrument for the ROSETTA orbiter, which will determine the abundances of selected major gases, the surface outgassing rate and the nucleus sub-surface temperature.
- **OSIRIS**: optical, spectroscopic and infrared remote imaging system which consists of a wide-angle and a narrow-angle camera to obtain high resolution images of the nucleus of 67P/C-G.
- **ROSINA**: ROSETTA orbiter spectrometer for ion and neutral species analysis, which will determine the composition of the comet's atmosphere and ionosphere, the velocities of ionized gas particles and reactions in which they take part.
- **RPC**: ROSETTA plasma consortium (plasma interface unit + five instruments: Ion and electron sensor, flux gate magnetometer, ion composition analyser, mutual impedance probe and plasma interface unit) which will study structure and dynamics of the comet - solar wind interaction during the comet's approach to the Sun. RPC will also examine the physical properties of the nucleus and, during the cruise phase, will provide scientific measurements about possible encounters of cometary ion tails and dust trails.
- **RSI**: radio science investigation, which will use shifts in the spacecraft's radio signal to measure mass, density and gravity of the nucleus of 67P/C-G.
- **VIRTIS**: visible and infrared thermal imaging spectrometer which will map and study the temperature of the surface of the nucleus and will identify comet gases, characterize the physical conditions of the coma.
- **SREM**: standard radiation environment monitor which will monitor the high energetic, ionizing particle environment aboard the spacecraft to provide an almost uninterrupted measurement of the high energetic particles encountered by ROSETTA.

The ROSETTA lander PHILAE can be considered a scientific spacecraft by its own. It will be carried by the ROSETTA orbiter to the comet and delivered in November 2014, when 67P/C-G will be at about 3 AU from the Sun. PHILAE will be dropped on the cometary surface from a distance of 1 – 2 nucleus radii (approximately 2 – 4 km) and at

a speed of up to 1 m/s. It is equipped with sophisticated touch-down equipments and harpoons which will assure a safe landing even in case of very hard or very soft and inclined surface layers.

The ROSETTA lander PHILAE contains 10 scientific instruments (Glassmeier et al. 2007):

- CIVA and ROLIS: panoramic and microscopic imaging system and descendent camera, respectively, which will take images of the cometary surface during the descent of the lander to the nucleus and after landing will continue the imaging of the surface and its environment around the landing site.
- SESAME: surface electrical, acoustic and dust impact monitoring (composed of comet acoustic surface sounding experiment, dust impact monitor and permittivity probe), which will perform electric and acoustic sounding of the surface and monitor dust impacts from cometary activity.
- CONSERT: the lander equipment of the CONSERT (radio sounding, nucleus tomography) experiment will receive and transmit the radio sounding signal from the orbiter counterpart of the instrument, allowing to explore the interior of the comet and the global constitution of the comet and a whole.
- ROMAP: magnetometer and plasma monitor, which will explore the magnetic and plasma environment of the landing site and its interaction with the solar wind.
- APXS: α -p-X-Ray spectrometer which will be deployed to the surface and will measure the elemental composition of the surface material.
- MUPUS: multi-purpose sensor for surface and sub-surface science, which will be deployed to the surface of the comet and will measure the thermal and mechanical properties of the sub-surface layers.
- SD-2: sampler, drill and distribution system, which can also retrieve mechanical properties of the nuclear surface.
- PTOLEMY: evolved gas analyser for isotopic composition (mass spectrometer).
- COSAC: evolved gas analyser for elemental and molecular composition (mass spectrometer & gas chromatograph).

The combined activities of the drill and sampling acquisition system SD-2 and of the mass spectrometer and gas chromatograph PTOLEMY and COSAC will collect and analyse surface and sub-surface samples of the nucleus for elemental, isotopic and molecular composition. A camera and the infrared spectrometer of the CIVA instrument will allow to take images and measure SD-2 samples before they are vaporized in the PTOLEMY and COSAC ovens.

After the intense measurement phase which will take place during the first 5 days after the landing of PHILAE on the nucleus of 67P/C-G, the long-term exploration of the comet will start. It consists in the monitoring of the temporal evolution of the nuclear activity and environmental phenomena, in a further sampling of the nucleus at different locations around the landing site and in continuing the exploration of the interior of the comet

through the CONSERT measurements. It is expected that PHILAE will survive the tough environment at the comet surface for few months up to at least when 67P/C-G will be at heliocentric distance of 2 AU.

2.7 Motivations of the thesis

As discussed in the previous paragraphs, 67P/C-G is the target comet of the ESA's ROSETTA mission. Thanks to space- and ground-based observations performed around perihelion, a detailed portrait of the comet has been drawn. What needs to be enhanced is the description of the comet's behaviour at large heliocentric distance, where ROSETTA will make its first approach to 67P/C-G. This information is of high importance for a good planning of the ROSETTA spacecraft rendezvous with the comet.

The purpose of this thesis is to study the properties of the nucleus of 67P/C-G and its dust environment at large heliocentric distance, thanks to ground-based observations performed in the visible wavelength range at the ESO Very Large Telescope (VLT). Using imaging and spectroscopy we wanted:

1. To investigate the possible presence of cometary activity in the aphelion arc.
2. To determine the nucleus size, the light curve over rotational phase, the rotation period of 67P/C-G with high accuracy (for a refinement of the values already determined by Lamy et al. (2006) and Lowry et al. (2006)) and the phase function of the nucleus.
3. To measure the colors of the nucleus and investigate possible color variations with rotational phase.
4. To investigate the presence of mineral and absorptive materials on the nucleus surface (through reflectance spectroscopy).
5. To detect and characterize the dust trail associated with 67P/C-G.

Moreover, this study provides valuable information on the basic physical properties of the nucleus of JFCs and its dust environment far away from the Sun. Due to their small size, JFCs are usually observed and well characterized mainly at small heliocentric distance. In addition, our characterization of 67P/C-G helps to identify to which extent this comet is a typical JFC.

A description of the instrument used for the observations, the datasets obtained and the methods employed for the analysis is presented in Chapter 3. The results are summarized in Chapter 4 and in Chapter 5 they are compared with what was already known about 67P/C-G and with the physical characteristics of other well-studied comets.

3 Observing strategy and performance of the observations of 67P/C-G

3.1 Observations: strategy and preparation

As outlined in the previous chapter, the main purpose of our observations is to obtain an accurate knowledge about the nucleus of 67P/C-G and its dust environment at large heliocentric distance, through groundbased observations. Why at large heliocentric distance? For three reasons. First, because the rendezvous of 67P/C-G with the ROSETTA spacecraft will take place at about 4.5 AU from the Sun, thus a good knowledge of the dust environment of the comet at that distance is necessary for the mission planning. Second, to provide valuable information of the dust environment of JFCs far away from the Sun, since they are usually observed and thus well characterized only much closer to it. Third, because JFCs and therefore also 67P/C-G is thought to be not (or at low level) active at large heliocentric distance and the best condition to characterize a comet's nucleus is when it is not surrounded by a coma.

We performed broadband imaging in different filters and spectroscopy of 67P/C-G. The purposes of the photometric observations were: 1) to investigate the possible presence of activity at large heliocentric distance and to monitor its evolution in the aphelion arc from 4.6 AU pre-aphelion to 4.6 AU post-aphelion. 2) to determine a well sampled rotational light curve of the nucleus of 67P/C-G from which to determine its rotational period with high accuracy. 3) to determine the nuclear colors and their possible variations with rotational phase. 4) to detect and characterize the dust trail associate with 67P/C-G. Through reflectance spectroscopy, instead, we wanted to investigate the possible presence of minerals and absorptive materials on the nuclear surface. Spectral slopes provide also valuable information about the nuclear color and its possible variations with rotational phase.

The expected 67P/C-G nuclear magnitude, estimated from previous measurements, was around 23 mag. Thus 67P/C-G was a faint object at the time of the observations. To obtain images and spectra with high signal-to-noise ratio, necessary for accurate measurements, the employment of a large telescope was required. For images, we required a signal-to-noise ratio SNR $\sim 50 - 100$, to achieve an accuracy of ± 0.05 mag in the determination of the magnitude of the comet. For spectroscopy, instead we required a signal-to-noise ratio SNR ~ 10 . Our observations, in fact, have been performed at the ESO 8.2m Very Large Telescope (VLT), as described in the following paragraphs. To achieve the same S/N ratio we obtained using a smaller telescope, we would have had to combine images together, losing both time resolution and a good sampling of the light curve, nec-

essary for an accurate determination of the rotational period. Regarding the spectra, one night of integration would have been necessary to achieve the S/N ratio needed to detect potential absorption and emission features.

Our observations can be divided into two groups: full nights of observations and short point-and-shoot runs. The full nights of observations, performed in visitor mode in April 2004, May 2006 and July 2007, are used to determine the nuclear properties of 67P/C-G over rotational phase. They consist of R filter imaging of 67P/C-G interspersed with V, I and B filter images and visible spectra of the comet. In 2006 and 2007 67P/C-G was at galactic latitude lower than 20° , thus projected in front of very star-rich background. Due to its motion, 67P/C-G could pass close to or even across background objects which contaminate the comet image or the background around it. Most of the times the contaminated frames have to be discarded from photometric measurements. To limit the loss of data we selected as observing nights the ones in which dust clouds in the Milky Way were present. In fact, they reduce the intensity of background objects and therefore they reduce the number of them in the field of view. Even though this precaution was taken, the background was still rather crowded, but not comparable with the one when no dust clouds were present (Fig. 3.1).

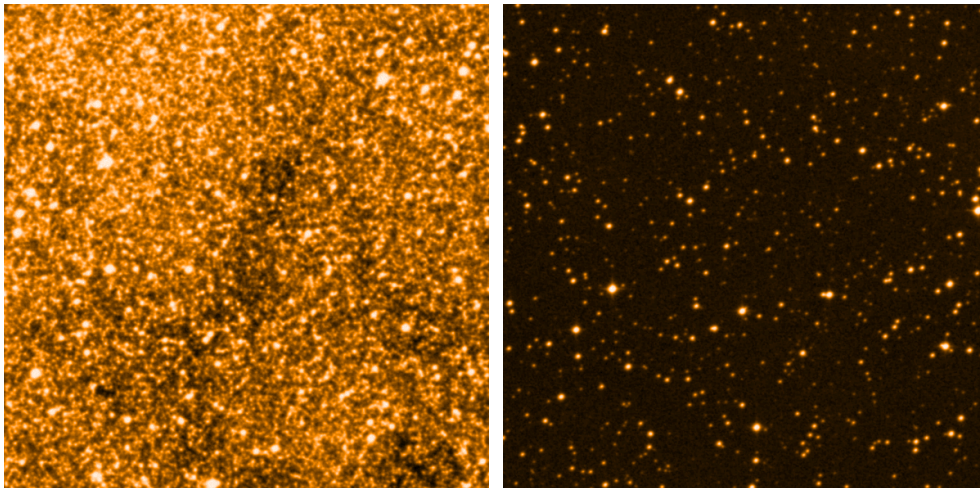


Figure 3.1: Star background when dust clouds are not present in the Milky Way (left panel) and when instead they are present (right panel). The field of view of each image is $10' \times 10'$. The images have been retrieve using the ESO Online Digitized Sky Survey (<http://archive.eso.org/dss/dss>).

The point-and-shoot observations, performed in service mode in June 2004 and August 2006, are used to investigate the activity and dust environment of 67P/C-G along the aphelion arc. They consist of short sequences of images of 67P/C-G in V, R and I filters in June 2004 and in R filter solely in August 2006. The dates of the August 2006 run were chosen to be simultaneous or at least close in time with scheduled Spitzer observations.

In the following sections we will describe the instrument used for the observations (Sec. 3.2), the acquired datasets (Sec. 3.3), the data reduction techniques applied (Sec.

3.4) and the methods employed to extract information from photometric (Sec. 3.5) and spectroscopic (Sec. 3.6) frames.

3.2 Instrumentation

The VLT at Cerro Paranal, in the Atacama Desert, is ESO's premier site for observations in visible and IR (<http://www.eso.org/instruments/>). It is composed of four unit telescopes (UT) of 8.2 m diameter each, which are individually in operation with different instruments (see Fig. 3.2, top panel). However, thanks to a combined focus, the four individual telescopes can work together, as the VLT Interferometer (VLTI). The telescopes act as a single, giant telescope, as large as the entire group. Our observations were performed using the FORS2 instrument (<http://www.eso.org/instruments/fors1/>). It is one of the two visual and near UV FOcal Reducer and low dispersion Spectrograph for the VLT of the European Southern Observatory (ESO). FORS2 is designed for the wavelength range from 3300 Å to 11000 Å and its detector consists of an array of two $2k \times 4k$ MIT CCDs (pixel size of $15 \times 15 \mu\text{m}$). In the standard resolution mode (which we used for the observations) the image scale in the default readout mode (2×2 pixel binning) is $0.25''/\text{pix}$, providing a field of view of $6.8' \times 6.8'$. FORS2 is mounted on the Cassegrain focus of the telescope. A schematic view of the instrument is represented in Fig. 3.2 (bottom panel). The main instrument components are:

1. The *Top Section* with the focal plane equipment for spectroscopy (slits and masks) and the calibration units (with calibration lamps).
2. The *Collimator Section* with the collimators and the electronic cabinets.
3. The *Filter/Camera Section* with the wheel for the Wollaston prism and the optional optical analysers (filters and/or grism), the grism wheel and the broadband filter wheel in the parallel beam.
4. The camera, the interference filter wheel in the converging beam and the exposure shutter in front of the CCD.
5. The detector in a liquid N_2 cooled dewar.

For a more detailed description of the instrument see http://www.eso.org/sci/facilities/paranal/instruments/fors/doc/VLT-MAN-ESO-13100-1543_v80.pdf.

3.3 Datasets

We performed broadband imaging and long slit spectroscopy of 67P/C-G in the visible wavelength range in April 2004, June 2004, May 2006, August 2006 and July 2007. The observational circumstances for each observing night are summarized in Table 3.6. At the time of the observations 67P/C-G was at heliocentric distance larger than 4.6 AU moving along its aphelion arc, as sketched in Fig. 3.3, where each triangle corresponds to the position of the comet at each observing epoch.

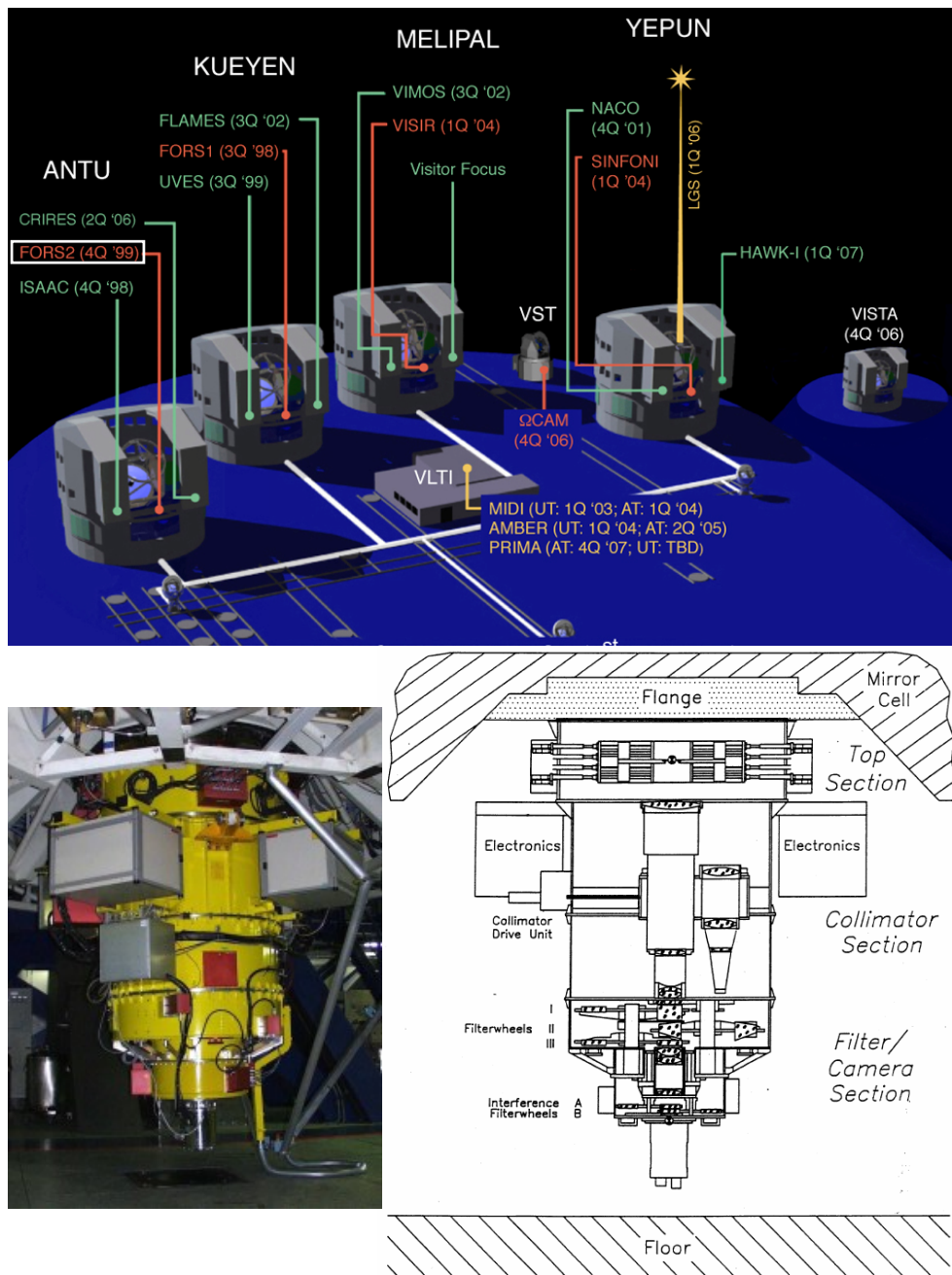


Figure 3.2: Top panel: schematic representation of VLT. The instruments mounted in each UT are indicated. Image adapted from <http://www.eso.org/sci/facilities/paranal/instruments/overview.html>. Bottom panel: photo together with a schematic view of FORS2. Images from <http://www.eso.org/projects/odt/Fors2/Fors2u.html> and FORS2 user manual, respectively.

Photometric observations of 67P/C-G were done with B, V, R and I Bessell filters. We obtained spectra of the comet using the low resolution grism 150I+27. Technical characteristics of the filters (i.e. transmission curves and central wavelengths) and of the grism (i.e. wavelength range, dispersion and efficiency curve) used are summarized in Appendix A. 67P/C-G is a moving target, therefore the observations were performed with the tele-

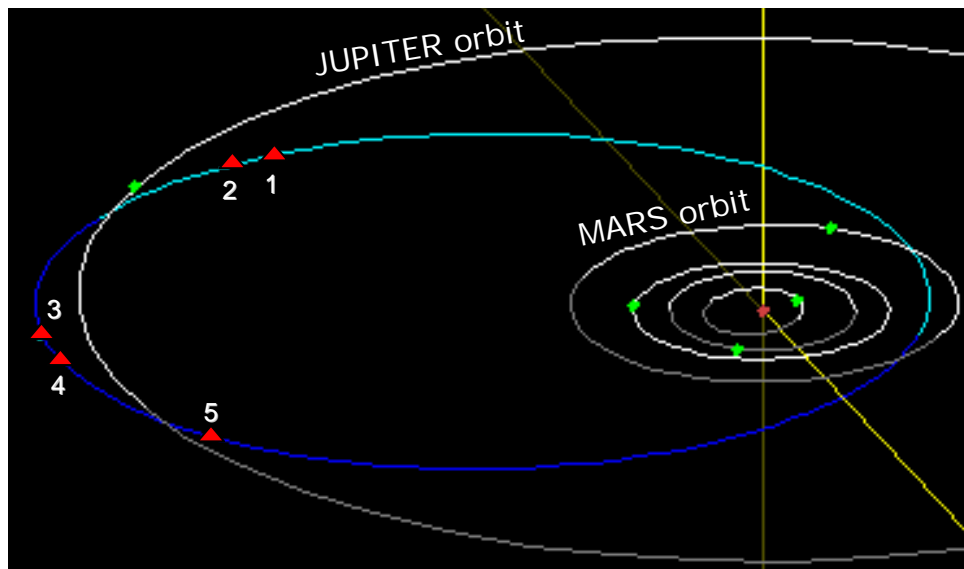


Figure 3.3: Orbit of 67P/C-G. The red triangles represent the position of the comet at each observing epoch: 1 = April 2004, 2 = June 2004, 3 = May 2006, 4 = August 2006, 5 = July 2007. In this image 67P/C-G moves in counterclockwise direction along its orbit. The orbits of Mercury, Venus, Earth, Mars and Jupiter are also shown.

scope tracking at the proper motion rate of the comet.

During each night of observation, in addition to science frames we obtained also calibration frame: bias and flat fields to perform standard data reduction, photometric standard star fields to flux calibrate comet images, solar analogue star spectra to remove the solar spectrum from 67P/C-G ones and arc-lamp spectra to wavelength calibrate comet and solar analogue star spectra.

The aim of each observing run was different, and therefore also the strategy of the observations, as described in the following sections. Information about photometric and spectroscopic calibrations obtained at all observing run is summarized in Sec. 3.3.6.

3.3.1 April 2004

The main purpose of this observing run was the determination of the light curve of the nucleus of 67P/C-G, its size, axis-ratio and colors. Two full nights of observation were granted to fulfill the aforementioned goals. One night was lost due to bad weather conditions and 67P/C-G was observed on April 14, 2004. At the time of the observation the comet was at heliocentric distance of 4.7 AU moving towards aphelion. The run consists of 50 broadband images of 67P/C-G in R Special, V Bessell, I Bessell filters; the number of exposures per filter is summarized in Table 3.1. To ensure a good signal-to-noise ratio ($S/N \sim 50$), we used an exposure time of 300 s for the V and R filter images; in order to avoid saturation of the CCD by sky background light, the I filter images were split in two exposures of 150 s each.

3.3.2 June 2004

The aim of this observation was the detection and characterization of the trail-like structure associated with the comet. Three hours of observation were allocated on June 16, 2004. The comet was at heliocentric distance of 4.9 AU, moving towards aphelion. The observation consists of three consecutive series of VRI broadband images, one series per filter, for a total of 38 images (for details see Table 3.1). The exposure times used are the same as in the April 2004 run.

3.3.3 May 2006

In May 2006 we observed 67P/C-G to characterize the physical properties of its nucleus and its dust environment. Four full nights of observations were granted in order to fulfill the following goals:

1. Assessment of the nucleus activity around aphelion and, if no activity was detected,
2. Accurate determination of the nucleus size and of the light curve over rotational phase for a refinement of the the rotational period of 12.41 ± 0.41 h (Lamy et al. 2006) and 12.72 ± 0.05 h (Lowry et al. 2006) and to achieve a firm reference for later studies of changes in the rotational period due to nuclear activity, and light curve shape along the comet's orbit due to changes of viewing geometry.
3. Measurement of possible VRI color variations with rotational phase.
4. Detection of potential minerals and absorptive materials on the nuclear surface through reflectance spectroscopy.

Since the rotational period of 67P/C-G is estimated to be of about 12 h, a full night of observation (8 – 9 h long) covers a good fraction of the rotational light curve. Three full nights of observations with one night gap in between would allow to sample the full comet light curve. Moreover, the time gap between the observing nights allows to achieve a higher accuracy in the rotational period determination. This is because the total time interval span by the time series (magnitude versus time) is longer.

Following the aforementioned criteria the observations were scheduled on May 25, 30, 31 and June 1, 2006. Due to bad weather conditions the last night was lost and 67P/C-G was observed on May 25, 30 and 31, 2006. The comet was at heliocentric distance of about 5.6 AU, post-aphelion, and at galactic latitude of about 15° , thus in front of a star-rich background. At the time of the observations, 67P/C-G was at phase angle between 0.5° and 1.3° , an interesting range to assess the opposition effect of the comet.

A total of 197 broadband images of 67P/C-G were taken during the three nights of observations in VRI filters. Also in this case, we used the same exposure times as in April 2004.

Reflectance spectra of the comet were obtained using a 1.3" slit and the low resolution grism 150I+27. The slit of the spectrograph was placed parallel to the direction of proper motion of the comet. Unfortunately, the spectrum observed on May 30 was too weak and it could not be used for analysis.

Additional details about images and spectra of 67P/C-G are summarized in Tables 3.1 and 3.2.

3.3.4 August 2006

We performed R filter imaging of 67P/C-G in parallel with scheduled Spitzer observations of the comet. We obtained 3 images of the comet per epoch, for a total of 4 epochs on August 17, 18, 22 and 23, when the comet was at about 5.5 AU from the Sun (post aphelion) and at phase angle slightly more than 10° . To have a reasonably good signal-to-noise ratio, the exposure time of each image was set to 350 s. For additional details see Table 3.1.

3.3.5 July 2007

One full night of observation was granted on July 16, 2007 during which we performed broadband photometry and long slit spectroscopy of 67P/C-G to verify the results obtained during the previous observing runs. At the time of the observation the comet was at heliocentric distance of about 4.6 AU and phase angle of about 6° .

A total of 156 images of 67P/C-G were taken in BVRI filters. To insure a reasonably good signal-to-noise ratio we used an exposure time of 100 s in R and V filters, 140 s in I filter and 420 s in B filter.

As in May 2006, reflectance spectra of the comet were obtained using the low resolution grism 150I+27. Also in this case the slit of the spectrograph (1.3" width) was placed parallel to the direction of proper motion of the comet.

Additional details about images and spectra of 67P/C-G are summarized in Tables 3.1 and 3.2.

date	filter	number frames	exposure time [s]	AM
April 2004	R	30	300	1.0 - 2.2
	V	7	300	1.0 - 2.0
	I	13	150	1.0 - 1.7
June 2004	R	10	300	1.1
	V	10	300	1.0 - 1.1
	I	18	150	1.0 - 1.1
May 2006	R	165	300	1.0 - 2.6
	V	8	300	1.0 - 1.6
	I	24	150	1.0 - 1.8
August 2006	R	12	350	1.0 - 1.8
July 2007	R	143	100	1.0 - 2.8
	V	3	100	1.2 - 1.3
	I	7	140	1.3 - 1.5
	B	3	420	1.4 - 1.5

Table 3.1: Summary of the photometric science frames obtained during all observing runs. The filters used (R = R special, V = V Bessell, I = I Bessell, B = B Bessell) as well as the number of frames per filter and the exposure times are listed. AM is the airmass range covered during the observations.

date	slit ["]	grism	number frames	exposure time [s]
May 25, 2006	1.3	150I+27	6	900
May 30, 2006	1.3	150I+27	2	900
May 31, 2006	1.3	150I+27	6	900
July 2007	1.3	150I+27	3	700

Table 3.2: Summary of the spectroscopic science frames obtained during May 2006 and July 2007 observations. Slit and grism used as well as the number of frames and the exposure times used are listed.

3.3.6 Photometric and spectroscopic calibrations

During each observing night, standard calibration frames were taken: bias (5 frames), sky flat fields (4 frames per filter), lamp flat fields (4 frames) and arc-lamp spectra (1 frame). In addition to the aforementioned standard calibration frames photometric standard star fields and solar analogue star spectra were observed, with the instrument in the same configuration as for the science frames (comet images and spectra, respectively). Since they are bright objects, the exposure time used was usually less than 1 s.

Tables 3.3 and 3.4 summarize the details about photometric standard star fields and solar analogue stars observed, respectively.

On May 25, solar analogue star spectra were obtained with a 1.3" slit, while the slit width used on May 30 and 31 was 1.0" (see Table 3.4). In fact, in parallel to the observations of 67P/C-G we also observed the asteroid (132524) 2002JF₅₆ (Tubiana et al. 2007), which required, on May 30 and 31, spectra obtained with a 1.0" slit. The slit width for the solar analogue spectra was set accordingly to the one of the asteroid spectra.

3.4 Data reduction: instrumental calibration of photometric and spectroscopic frames

In this section we describe data reduction of photometric and spectroscopic frames. First we introduce the calibration frames (bias, dark current, flat field and arc-lamp spectra), how they are obtained and what they are used for. Then we address the problem of the background subtraction.

A raw CCD image contains information about the science object (in our case 67P/C-G), but it contains also noise, both random and systematic. While the random noise can only be measured to understand which contribution it gives to the signal from the object (S/N ratio), the “known” part of the systematic noise can be eliminated through the calibration of the images. There are two types of CCD calibration data: one type corrects for additive systematic noise (bias and dark current) and the other for multiplicative systematic noise (flat field).

Bias: it is an electrical offset which is applied to the CCD before readout, first, to make the CCD working and, second, to shift the zero-level of the CCD to a positive value. Bias is constant in time but varies from pixel to pixel (see Fig. 3.4, top panels). Bias frames

3.4 Data reduction: instrumental calibration of photometric and spectroscopic frames

date	field name	filter	AM
April 2004	PG1323-086	R, V, I	1.4
	PG1633-099	R, V, I	1.2
	Mark-A	R, V, I	2.1
June 2004	PG1323-086	R, V, I	1.1
May 25, 2006	PG1047+003	R, V, I	1.1
	SA98-670	R, V, I	2.1
	PG1528+062	R, V, I	1.2
	SA92+249	R, V, I	1.7
	SA110	R, V, I	1.6
May 30, 2006	PG1047+003	R, V, I	1.1
	SA98-670	R, V, I	2.3
	PG1528+062	R, V, I	1.2
	SA92+249	R, V, I	1.6
	SA110	R, V, I	1.3
May 31, 2006	PG1047+003	R, V, I	1.1
	SA98-670	R, V, I	2.2 - 2.3
	PG1528+062	R, V, I	1.2
	SA92+249	R, V, I	1.5
	SA110	R, V, I	1.8 - 1.9
August 2006	PG1633+099	R	1.2
July 2007	PG1657+078	R, V, I, B	1.7
	PG1323+086	R, V, I, B	1.1
	PG2331+055	R, V, I, B	1.2

Table 3.3: Summary of the standard star fields observed during all observing runs. The filters used (R = R special, V = V Bessell, I = I Bessell, B = B Bessell) together with the airmass range covered during the observations are listed.

are obtained with a very short exposure (ideally a zero-seconds exposure) and the shutter closed. We create a *bias median* image median-averaging a series of bias frames. We subtract this *bias median* image from the science frames and flat fields.

Dark current: thermal agitation in the silicon layers of the CCD produces electrons which are indistinguishable from photoelectrons (produced by the light from the object incident on the CCD). Thermal electrons give rise to a *dark current* which, in absence of light, follows the law:

$$I_d = A \cdot e^{-\frac{B}{kT}} \quad (3.1)$$

where A and B are constants, k is the Boltzmann constant and T is the device temperature. Dark images are obtained with the shutter closed and with an exposure time much longer than the one used for the science frames. If the CCD is properly cooled down, the dark current is negligible for exposure times up to few 10 minutes. In our case, the dark current is always neglected.

date	field name	slit ["]	grism
May 25, 2006	HD89010*	1.3	150I+27
	SA102-1081	1.3	150I+27
	SA110-361	1.3	150I+27
	SA112-1333	1.3	150I+27
	SA115-271	1.3	150I+27
May 30, 2006	SA102-1081	1.0	150I+27
	SA110-361	1.0	150I+27
	SA112-1333	1.0	150I+27
	SA115-271	1.0	150I+27
May 31, 2006	SA102-1081	1.0	150I+27
	SA110-361	1.0	150I+27
	SA112-1333	1.0	150I+27
	SA115-271	1.0	150I+27
July 2007	SA107-998	1.3	150I+27
	SA115-271	1.3	150I+27

Table 3.4: Summary of the solar analogue stars observed during May 2006 and July 2007 runs. The slit and grism used are listed. The star spectra marked by the asterisk (HD89010) were saturated and could not be used.

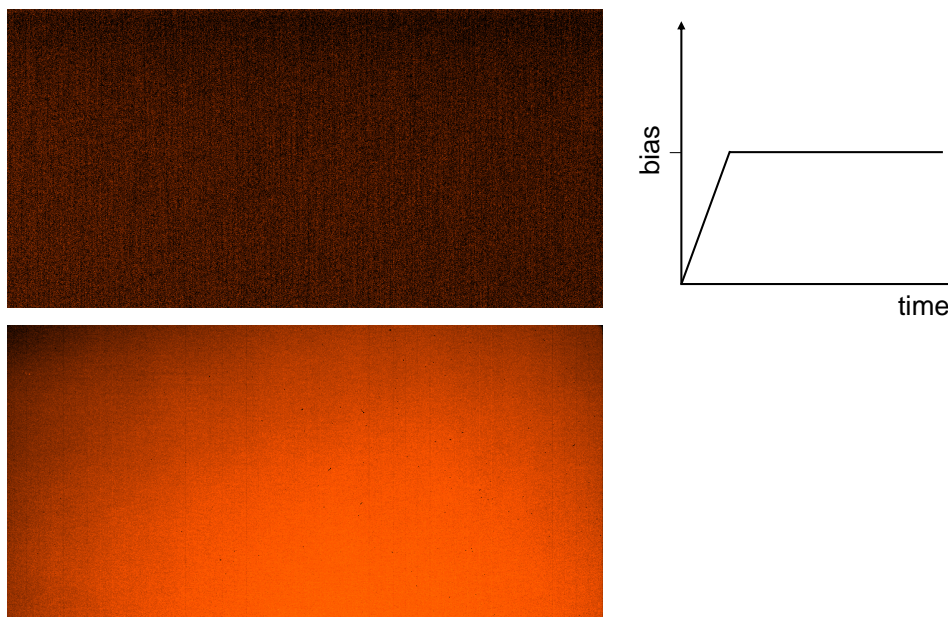


Figure 3.4: Top panels: example of bias frame and bias versus time. Bottom panel: example of flat field image.

Flat field: it corrects for the non-uniform sensitivity of the CCD. Two kinds of non-uniformities can be distinguished: a pixel-to-pixel variation and a gradient across the chip. Thus, when the CCD is exposed to a uniform radiation, the resulting image is not uniform, as shown in Fig. 3.4, bottom panel. In order to eliminate these spatial variations, the science frames are divided by the *flat field*.

To reduce photometric images different kinds of flat field exist:

1. twilight flat field: images of the sky obtained just after sunset or before sunrise, when the sky better approximates uniform illumination. These images are taken with the same settings (exposure time, filter) as for the science frames. The advantage of twilight flat fields is that the light enters the telescope in a very similar way as during the night. The disadvantage is that the sky brightness changes rapidly during twilight and it can be difficult to obtain several frames with high signal-to-noise ratio. In addition, twilight flat fields can contain stars, in particular if they are taken when the twilight brightness is low.
2. dome flat field: images of an uniformly illuminated screen inside the dome. Usually dome screens are not quite as uniform as the twilight sky, thus twilight flats are usually flatter than dome flats. Moreover, the direction of entry of the light is different from that during the night. The advantage of dome flat fields, instead, is that it is easy to obtain several frames with high signal-to-noise ratio. For big telescopes, as for instance VLT, dome flat fields are not possible, mainly due to the difficulty to obtain an homogeneous illumination of the dome screen, since its surface is very extended. Instead instrument screen flat fields are used. In this case the screen is inside the instrument and it has a much smaller size. If the advantage of instrumental screen flat fields is to obtain a more homogeneous illumination, the disadvantage is that the light from a lamp does not go through the telescope optics, but only through the instrument.
3. superflat field: obtained as a median-average of many night exposures. The advantage is that the color of this flat field is representative of the night sky. A major disadvantage is their very low signal-to-noise ratio, due to the very low counts of the background night sky.

Often superflat fields are a better choice rather than twilight or screen flat fields. When the night sky background is very crowded, as i.e. when observations take place at low galactic latitude, the median combination of science frames might not work very efficiently in removing background stars. Thus, their remnants might be visible in the superflat field and will create dark spots in the reduced images. Figure 3.5 shows the comparison between the superflat field and the twilight flat field corresponding to the same dataset, obtained in the aforementioned situation. Remnants of stars can also occur in the superflat field due to a too small number of images used to create the superflat field.

In the reduction of our datasets for broadband imaging we use superflat fields where possible, otherwise we used a median-average of twilight flat fields.

In case of spectroscopy, twilight flat fields cannot be used because light from the twilight sky does not produce white light. Incandescent lamps are employed to create flat field images, since they produce a continuum spectrum. A lamp flat field is obtained in two ways: either the telescope is aimed at a dome screen illuminated by lamps, or the light from a lamp is brought to focus on the slit.

The reduced images are obtained as follows:

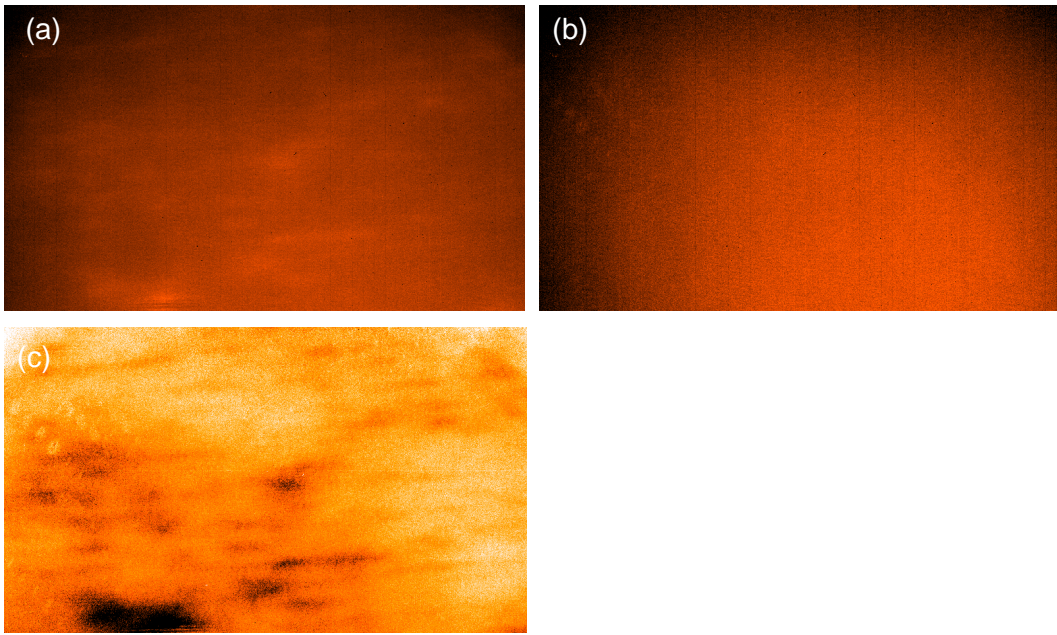


Figure 3.5: Example of superflat field (a) and twilight flat field (b) in R filter corresponding to the same dataset. The superflat field has been obtained from night exposures which are very crowded from background objects. Remnants of stars are visible in the superflat field image. The ratio between the two images is displayed in (c).

$$reduced\ image = \frac{image - bias}{flat\ field - bias} \quad (3.2)$$

Reduced images are then: a) cosmic rays corrected, replacing the intensity of the pixels hit by cosmic rays with the median value of the intensities of the neighbouring pixels; b) exposure time normalized to 1 s and c) sky background subtracted.

The procedure of sky background subtraction is different for photometric and spectroscopic images and it is described in the following.

In case of spectroscopy, the reduced frames have to be wavelength calibrated before to be sky background subtracted. The wavelength calibration is done using an arc-lamp spectrum in which the wavelengths of the emission lines are known (Fig. 3.6).

In case of low dispersion spectroscopy argon, mercury and neon arc-lamps are a good choice, while iron and thorium are often used for high dispersion spectroscopy, since their spectra contain a large number of emission lines. Arc-lamp spectra are obtained with the same instrumental configuration as for spectroscopic science frames. Comparing the pixel position of the emission lines with their tabulated wavelength, the wavelength calibration or dispersion curve is determined as a polynomial fit to the pixel-wavelength correspondence. It is then be applied to all comet and solar analogue star spectra.

The procedures of sky background subtraction for photometric and spectroscopic frames are described hereafter.

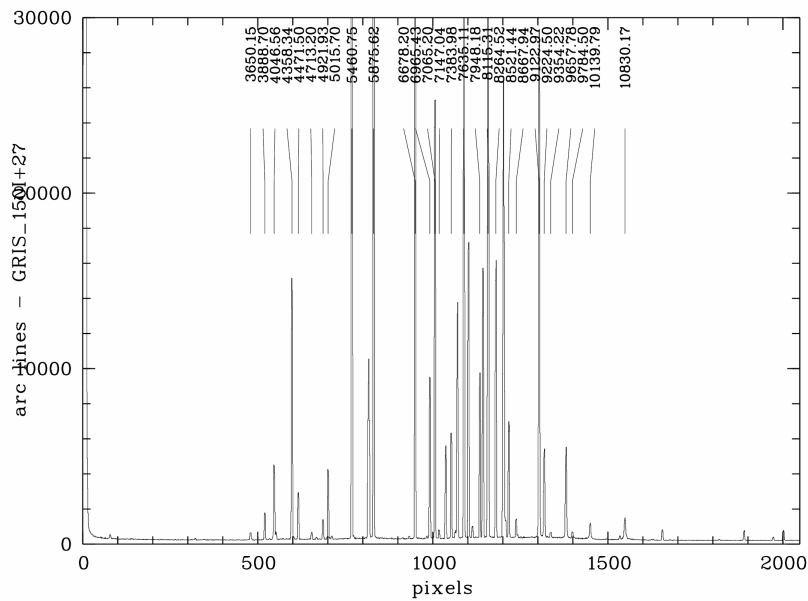


Figure 3.6: Arc-lamp spectrum for wavelength calibration of spectroscopic frames. The wavelength of the emission lines (in Å) is shown in the top part of the figure.

Photometric images: in each image we select an area where no stars are present; this selected area has to be the same region of the sky for all the images of one dataset. We calculate the median average inside this area and subtract the median average per pixel to each pixel of the image.

Photometric images are now fully reduced and the comet's magnitude can be measured from each frame. Figure 3.7 shows a science frame before (left panel) and after reduction (right panel).

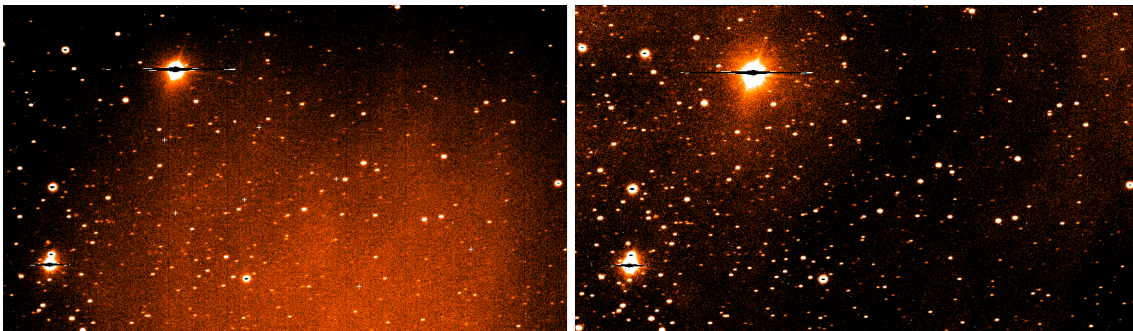


Figure 3.7: A science frame before (left panel) and after reduction (right panel).

The reduction procedure just described has to be applied also to photometric standard star frames, which are used to flux calibrate the comet's magnitude.

Spectroscopic images: one of the most delicate aspects of the spectra reduction is the removal of the sky emission lines. Figure 3.8 (a) shows a 2D spectrum of the comet before the sky emission lines subtraction is applied. The comet spectrum is the faint

horizontal line close to the bottom of the image. Sky emission lines (vertical lines) are very well visible. In order to achieve a very accurate background subtraction we split each measurement of the object in two exposures at two different slit positions A and B, 20" apart. Since the slit, in the aforementioned image, is placed parallel to the y-axis, this results in two spectra of the comet placed at two different y position. Subtracting spectrum A and B from each other, a very accurate background subtraction is achieved, as shown in Fig. 3.8 (b) and (c). In order to increase the signal-to-noise ratio, the positive spectra resulting from A - B and B - A subtractions are aligned and summed-up (Fig. 3.8 (d)). After sky lines subtraction, the comet spectrum has to be extracted from the 2D image. The extraction region has to be wide enough not to leave out signal from the spectrum, but at the same time not too wide to avoid to include too much background in it. We do not use a fixed width for the extraction area (i.e. 3-sigma), but we choose the most appropriate one for each spectrum through visual inspection. Unfortunately, not all the background is removed during the sky lines subtraction. Thus, an additional background subtraction is applied during the spectrum extraction procedure. Two regions for the background determination are selected, usually one above and one below the spectrum. For faint objects this additional background subtraction is not always applied since it adds noise to the extracted spectrum.

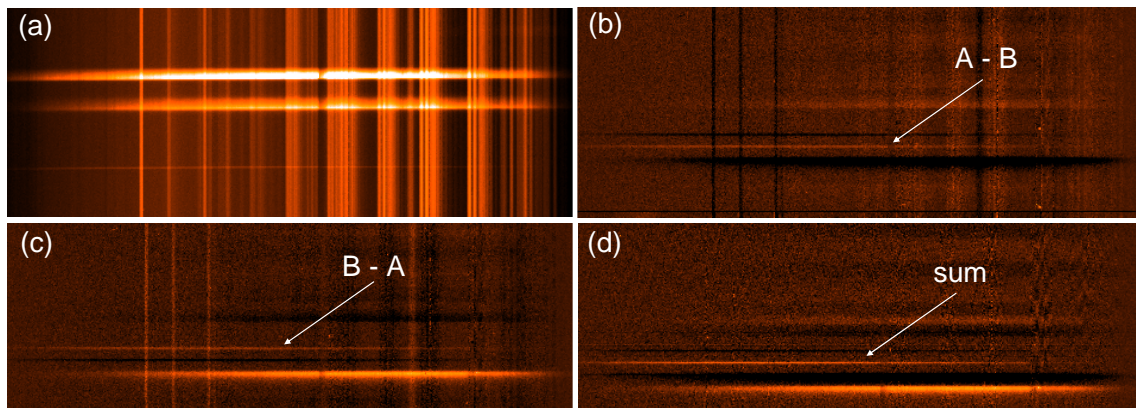


Figure 3.8: In each image wavelength is on the x-axis (increasing from left to right). The intensity of the spectra is color coded (with increasing intensity from black to white). (a): 2D spectrum of the comet before sky emission lines subtraction. The comet spectrum is the thin horizontal line in the bottom part of the image. Sky emission lines (vertical lines) are well visible. (b) and (c): 2D spectra of the comet resulting from A-B and B-A subtraction respectively. The position of the positive comet spectra is marked. Most of the sky lines have been removed. (d): image resulting from the sum of the previously described images aligned on the positive spectrum of the comet. Sky background lines are very well removed at short wavelength while some remnants are still visible at longer wavelength. In all panels, the thick lines are star spectra.

The reduction procedure just described for the comet spectra has to be applied also to solar analogue star spectra, which are used to remove the Sun spectrum from the comet one.

The last step in the spectra reduction is the removal of the solar spectrum from the

comet one. This is achieved through the division of the comet spectrum by the average of solar analogue spectra obtained with the same slit width. Finally, comet spectra are normalized to unity at 6380 Å (central wavelength of the R filter).

For the analysis of photometric and spectroscopic images (from the instrumental calibration to the extraction of information from the science frames) we used the ESO-MIDAS software (for details see <http://www.eso.org/sci/data-processing/software/esomidas/>).

3.5 Photometry: methods & calibrations

3.5.1 Methods

Once the photometric images are fully reduced, the comet's magnitude is measured. For all datasets we used the technique of *aperture photometry*. More details about this technique are presented in Appendix B.1.

For the June 2004 and May 2006 datasets the measurement of the comet's magnitude was rather straightforward. In the latter epoch, 67P/C-G was at low galactic latitude and therefore the field was very crowded of background stars and galaxies. Due to its motion, the comet passed close by or even across a number of background objects, making the photometric measurements difficult and in some cases even impossible. Thus, when a background star was contaminating the comet image or the sky background around, we discarded the image for photometric measurements.

In August 2006 and July 2007 an additional treatment of the images had to be applied before to measure the comet's magnitude. In both dataset, 67P/C-G passed in the vicinity of plenty of stars and it was not possible to discard all the images where the comet was contaminated by their presence. To remove the star's contamination we proceeded in the following way: first we rebinned each image to a new pixel size of 0.2×0.2 pixel (the image flux is conserved during rebinning). Then we aligned the images on a star; thanks to the rebinning to a smaller pixel size, we achieved a very precise alignment of the images. Finally we subtracted two rebinned aligned images to obtain a final frame in which the comet was free from contaminations. Figure 3.9 show the comparison between the original frame and the one after the subtraction. The star contamination is successfully removed from the vicinity of the comet. Three saturated stars (which display a white region close to their center) are visible in the original image. Since saturation is different from frame to frame, those stars cannot be completely removed during subtraction and their remnants are visible in the subtracted frame (Fig. 3.9).

To achieve an accurate result, some expedients have to be taken:

1. The two images used for the subtraction have to be taken with seeing values as close as possible. Seeing affects the star profile and to have a good star removal, the star profiles have to be as similar as possible. For each frame we determined the full width half maximum (FWHM) of a star, which gives the value of the seeing at the moment at which the image was taken.
2. The comet position does not have to overlap in the two images used for subtraction, to avoid comet's flux removal during subtraction. When the comet is not active, a

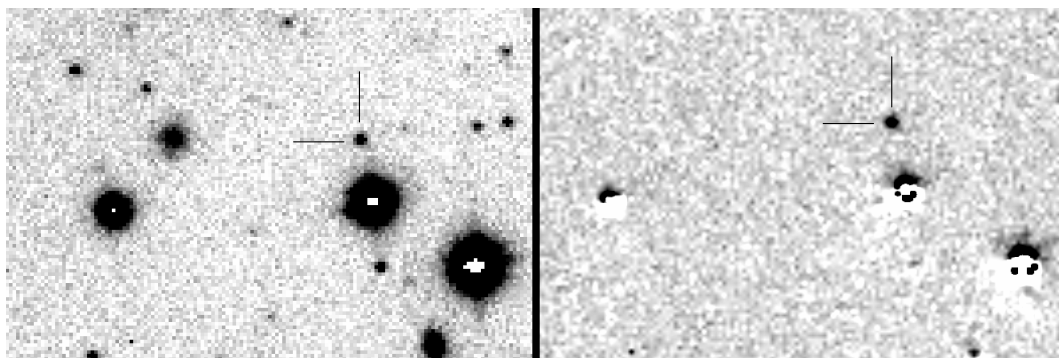


Figure 3.9: Example of subtraction between two images to remove the star contamination from the vicinity of the comet. The original frame is shown in the left panel, while the subtracted frame is displayed in the right one. In both cases the comet position is marked. Remnants of saturated stars are visible in the subtracted frame.

distance between the comet positions of about 3 – 5 times the diameter of the comet is enough to avoid comet's flux removal during subtraction.

The closer the comet is to the star, the less are the chances to obtain a good removal of the star contamination. In addition, the closer the comet flux is to the one of the contaminating star, the better the contamination is removed.

In August 2006 the observations were split in 4 nights. Due to the small motion rate of the comet, part of the star field in the first night overlaps with part of the star field in the second night and part of the field of the third night overlaps with part of the field of the fourth night. Since the seeing was rather constant during all nights of observation, we subtracted rebinned images of different nights centered on the same star.

In July 2007 we had only one night of observation and the motion rate of the comet was very low, which implied that the position of the comet in consecutive images was very similar. In addition, strong seeing variations (between 0.5" and 1.5") took place during the night. To achieve an accurate star removal we had to subtract images as close as possible in time (to have as small as possible seeing variations) but paying attention that the position of the comet in the two images was well separated.

Finally, for both datasets we measured the comet magnitude using aperture photometry on the rebinned subtracted images.

In April 2004 the night of observation was not photometric. Thus, in July 2007 we observed the same star field as in April 2004 (using the same instrumental configuration) and we used it to cross-calibrate the April 2004 dataset. A comparison between one of the images taken in April 2004 and the calibration field observed in July 2007 is shown in Fig. 3.10. In the calibration field we selected a certain number of stars which could be used to calibrate the April 2004 dataset. Those stars are labelled in the aforementioned figure. The stars have to be:

1. Non variable,
2. Bright enough to have a reasonable high S/N ratio also when the seeing is bad but at the same time non saturated when the seeing is good (in all April 2004 images and in the calibration field).

3. Isolated, to determine their magnitude with aperture photometry.

Only stars E, F and H fulfilled the previously described requirements. Stars A, B, C and D are saturated in the images when the seeing is good and star G has a too low S/N ratio when the seeing is bad. When stars are not variable, variations in their magnitude from one frame to the other and with respect to the calibration field are due to seeing and extinction variations. These variations (seeing and extinction) affect the star's magnitudes and the comet's magnitude in the same frame in the same way. If the comet would not be variable the difference between star and comet magnitude (in the same frame) would be constant in time. Thus, changes in the aforementioned difference are "produced" by the comet (shape and/or composition).

For the determination of the comet's magnitude we proceeded in the following way:

1. In the calibration field we measure the magnitude of star E, F and H with the technique of aperture photometry. We flux calibrate the measured magnitudes with zero points, color and extinction coefficients determined for the July 2007 dataset.
2. In each frame taken in April 2004 we measured the magnitude of the comet and of stars E, F and H always with the technique of aperture photometry.
3. Image by image, per each star we compute the difference:

$$\Delta m_{star,i} = [m_{star,i}]_{calib} - [m_{star,i}]_{April2004} \quad (3.3)$$

where $i = E, F, H$, $[m_{star,i}]_{calib}$ is the star's apparent magnitude in the calibration field and $[m_{star,i}]_{April2004}$ is the measured magnitude of the same star in the April 2004 image. $\Delta m_{star,i}$ is a "calibration coefficient" which corrects the comet's magnitude for extinction and seeing variations.

4. The comet's apparent magnitude is:

$$m_{apparent} = m_{meas} + \Delta m_{star} \quad (3.4)$$

We obtain three values of comet's magnitude per frame.

3.5.2 Flux calibration of photometric images

Once the magnitude of the comet has been measured in each image, it has to be "flux calibrated": corrected for the effects produced by the transit of the reflected light from the comet through the Earth's atmosphere and for the color sensitivity of the optical system used.

The flux calibrated measured magnitude of the object is called apparent magnitude and it is determined using:

$$m_{apparent} = m_{meas} + m_{zero\ point} - k \cdot AM + A \cdot color, \quad (3.5)$$

The derivation of Eq. 3.5 is treated in Appendix B. The flux calibration coefficients are determined using fields of photometric standard stars

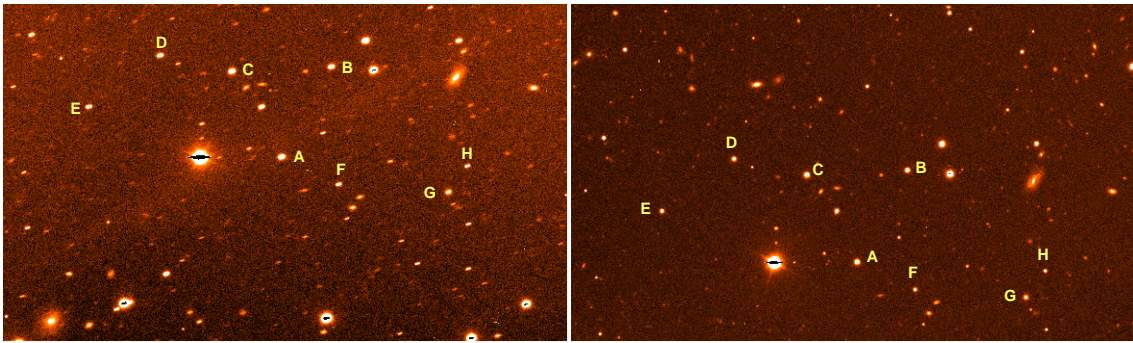


Figure 3.10: Comparison between one image taken in April 2004 (left panel) and the calibration field observed in July 2007 (right panel). The selected stars to calibrate the April 2004 data are labelled.

(Landolt 1992). For those stars the visual magnitude together with their colors B-V, U-B, V-R and R-I, obtained using a standard photometric system (for instance the original Bessell filters), is tabulated.

A detailed description of the method employed in the determination of the flux calibration coefficients is presented in Appendix B.

We determined the flux calibration coefficients for the different observing runs in the way described hereafter.

June 2004: with the standard star field observed during the night (PG1323-086) we determined the zero points, adopting color coefficients and extinction coefficients as provided by ESO for the period when the observations were carried out (http://archive.eso.org/bin/qc1.cgi?action=qc1_browse_instrume&instrume=FORS2).

May 2006: since 22 photometric standard star fields were observed over a wide air-mass range during the three observing nights (Table 3.3), we determined all the photometric coefficients. We determined a unique solution for the three nights of observation. A unique solution avoids that artificial offsets have to be applied to match the light curves from different observing night, as would happen if the photometric calibration would be determined night by night.

To test the goodness of the determined photometric coefficients, we used one of the observed photometric standard stars as it would have been our target and we calculated its magnitude using the determined coefficients. Since the obtained star magnitude coincided with its tabulated values, we concluded that the flux calibrations coefficients were reliable.

August 2006: the standard star field PG1633+099 was used to determine the zero point, assuming color and extinction coefficients as determined from the May 2006 measurements.

July 2007: we determined zero points and extinction coefficients from the various standard star fields observed during the night at different air mass (Table 3.3). Regarding the color coefficients, we adopted the ones determined in May 2006 for V, R, I filters,

while for the B filter we used the value provided by ESO for the night when the observation was carried out. In fact in May 2006 no B filter observations were carried out and thus no color coefficient for this filter was available.

The flux calibration coefficients for all nights of observations are summarized in Table 3.7.

3.5.3 Correction for heliocentric and geocentric distances and phase angle

Once the magnitude of an object (i.e comet) has been flux calibrated, it is independent from the instrument with which it has been determined and the atmospheric extinction. But it still depends on the heliocentric and geocentric distance of the comet at the time of the observation and on the phase angle:

$$m_{\text{apparent}} = m(r, \Delta, \alpha). \quad (3.6)$$

To compare with other measurements of the same objects performed in other locations or in other periods, the apparent magnitude has to be scaled as if the object would have been observed at heliocentric and geocentric distances of 1 AU and at zero phase angle:

$$H \equiv m(1, 1, 0) = m_{\text{apparent}} - 5\log(r\Delta) + 2.5\log[\Phi(\alpha)], \quad (3.7)$$

where the second term on the right-hand side of the equation corrects for heliocentric (r) and geocentric (Δ) distances, respectively, and the third one for the phase angle (α). H is called *absolute magnitude*.

Two approximations for the phase function $\Phi(\alpha)$ are used:

1. the linear phase function approximation (Lamy et al. 2004), which assumes a linear increase of brightness with decreasing phase angle:

$$2.5\log[\Phi(\alpha)] = -\alpha \cdot \beta \quad (3.8)$$

where α and β are the phase angle and the linear phase coefficient, respectively.

2. IAU-adopted phase law, which includes the opposition effect at small phase angles (Meeus 1998):

$$2.5\log[\Phi(\alpha)] = 2.5\log[(1 - G)\Phi_1 + G\Phi_2] \quad (3.9)$$

with

$$\Phi_1 = \exp\left[-3.33\left(\tan\frac{\alpha}{2}\right)^{0.63}\right] \quad (3.10)$$

$$\Phi_2 = \exp\left[-1.87\left(\tan\frac{\alpha}{2}\right)^{1.22}\right] \quad (3.11)$$

where α is the phase angle and G the ‘‘slope parameter’’.

Both the linear phase coefficient and the slope parameter indicate how magnitude varies with respect to phase angle.

3.5.4 Errors on photometric measurements

For the photometric error estimation we consider three contributions: the error on the aperture measurement, the error of the flux calibration coefficients and one due to the “non-flatness” of the flat field used. The error on the aperture measurements is determined automatically by MIDAS per each measurement. The Gaussian error propagation of Equation 3.5 produces the part of error on the apparent magnitude due to the first two contributions (aperture measurement and flux calibration coefficients).

The error due to the “non-flatness” of the flat field used is significant for absolute photometry, but frequently is not taken into account. We determined this error in the following way. Per each image (in the case of R filter images obtained in April 2004, May 2006 and July 2007 we selected part of the images) we measured the gradient across the CCD in four directions: along the two diagonals, along a horizontal line and a vertical one. Even though the comet is usually placed close to the center of the CCD, we measured the gradients across the whole CCD, since the photometric standard stars used for the flux calibrations are located in different parts of the frame and not only close to the comet’s position. The error due to the “non-flatness” of the CCD per each observing epoch is summarized in Table 3.5.

observing epoch	$\sigma_{flatness}[\%]$
April 2004	3
June 2004	3
May 2006	2
August 2006	4
July 2007	5

Table 3.5: Errors due to the “non-flatness” of the flat field used.

The final error on the apparent (and therefore relative and absolute) magnitudes is:

$$\sigma = \sqrt{\sigma_{a,f}^2 + \sigma_{flatness}^2} \quad (3.12)$$

where $\sigma_{a,f}^2$ is the error due to aperture measurement and flux calibration coefficients and $\sigma_{flatness}^2$ is the contribution from the “non-flatness” of the flat field used.

3.6 Spectroscopy: method

As we will discuss in Sec. 4.4, the comet spectra do not show any absorption or emission feature both in May 2006 and in July 2007. They present only a reddening. For each spectrum we determined the slope of the reddening through a linear fit of the normalized reflectance versus wavelength.

3.6.1 Uncertainties on the spectra

The signal-to-noise ratio of the spectra is wavelength dependant, therefore also the uncertainties on the spectra. For the May 2006 spectra we determined relative errors in 3

wavelength regions: around 5000 Å, 6500 Å and 8000 Å. For the July 2007 spectrum the relative errors were calculated, in addition to the three aforementioned wavelength regions, also around 4300 Å and around 7800 Å. For each of this regions we calculated the standard deviation in an interval of 140 Å, which directly provides the signal-to-noise ratio at that wavelength.

start time [UT]	end time [UT]	r [AU]	Δ [AU]	α [°]	GL [°]	sky condition	observation type	observing mode
15.04.04 00:58	15.04.04 08:40	4.67	3.68	2.1	47.4	CLR/non PHO	IM	V
16.06.04 23:20	17.06.04 02:17	4.89	4.29	10.3	52.6	CLR	IM	S
26.05.06 01:00	26.05.06 09:42	5.62	4.61	1.3	14.7	CLR	IM & SP	V
31.05.06 00:28	31.05.06 09:33	5.61	4.60	0.6	15.3	CLR	IM & SP	V
01.06.06 00:17	01.06.06 09:46	5.61	4.60	0.5	15.5	CLR	IM & SP	V
18.08.06 01:42	18.08.06 02:03	5.51	5.27	10.5	21.3	CLR	IM	S
19.08.06 01:29	19.08.06 01:48	5.51	5.28	10.5	21.2	CLR	IM	S
23.08.06 02:32	23.08.06 02:52	5.50	5.34	10.6	21.1	CLR	IM	S
23.08.06 23:30	23.08.06 23:53	5.50	5.35	10.6	21.1	CLR	IM	S
16.07.07 23:51	17.07.07 08:00	4.63	3.72	6.0	0.6	CLR	IM & SP	V

Table 3.6: Details of the observations of 67P/C-G: date and start & end time of the observations, r and Δ are the heliocentric and geocentric distance, respectively, α is the phase angle and GL the galactic latitude of the comet. The average sky conditions during the night are reported (PHO = photometric, CLR = clear) as well as the type of observations performed (IM = imaging, SP = spectroscopy) and the observing mode used (V = visitor mode, S = service mode).

date		R	V	I	B	source
June 2004	zero point [mag]	28.179 ± 0.019	27.908 ± 0.018	27.478 ± 0.008	–	our
	extinction coefficient [mag AM ⁻¹]	0.109 ± 0.010	0.122 ± 0.006	0.037 ± 0.007	–	ESO
	color coefficient	-0.041 ± 0.010	0.032 ± 0.004	-0.018 ± 0.004	–	ESO
	color [mag]	V-R	B-V	V-I	–	
May 2006	zero point [mag]	28.116 ± 0.011	27.874 ± 0.008	27.470 ± 0.016	–	our
	extinction coefficient [mag AM ⁻¹]	0.092 ± 0.007	0.130 ± 0.005	0.055 ± 0.011	–	our
	color coefficient	0.006 ± 0.008	0.029 ± 0.005	-0.045 ± 0.007	–	our
	color [mag]	V-R	V-R	V-I	–	
August 2006	zero point [mag]	28.125 ± 0.014	–	–	–	our
	extinction coefficient [mag AM ⁻¹]	0.092 ± 0.007	–	–	–	our*
	color coefficient	0.006 ± 0.008	–	–	–	our*
	color [mag]	V-R	–	–	–	
July 2007	zero point [mag]	28.168 ± 0.023	27.926 ± 0.022	27.516 ± 0.016	27.443 ± 0.021	our
	extinction coefficient [mag AM ⁻¹]	0.095 ± 0.016	0.121 ± 0.016	0.025 ± 0.011	0.179 ± 0.015	our
	color coefficient	0.006 ± 0.008	0.029 ± 0.005	-0.045 ± 0.007	-0.024 ± 0.008	our*/ESO
	color [mag]	V-R	V-R	V-I	B-V	

Table 3.7: Flux calibration coefficients determined for each observing epoch for the filters employed in the observations, as described in Sec. 3.5.2. “Color” is the filter combination used for the color coefficients determination. “Source” indicates if the photometric coefficient has been determined by us (our) or if we adopted the value provided by ESO. The * marks that we adopted the photometric coefficient determined in May 2006.

4 Results on 67P/C-G

This chapter summarizes all the results obtained from photometry and spectroscopy of 67P/C-G in April and June 2004, May and August 2006 and July 2007.

Examples of comet images in R filter for each of our observing runs are displayed in Fig. 4.1. Each panel displays only part of entire field of view. In May 2006 (Fig. 4.1 (c)), August 2006 (Fig. 4.1 (d)) and July 2007 (Fig. 4.1 (e)) 67P/C-G was at low galactic latitude; therefore the field was crowded with background objects, which makes accurate photometry of the comet a difficult task. The uneven diffuse background is due to galactic clouds. In each frame the comet's position is marked and image scale and orientation are shown.

With the technique of aperture photometry we measured the apparent magnitude $m(r, \Delta, \alpha)$ of the comet in each frame. The reduced magnitude $m(1, 1, \alpha)$ for each observing run is listed in Table C.1. Figures 4.2, 4.3 and 4.4 shows the R filter reduced magnitude versus time for the April 2004, May 2006 and July 2007 datasets, respectively.

The gaps in the time series are due to: 1) photometry of the comet done in different filters, 2) rejected measurements because of background object contaminations, 3) observations of spectra of 67P/C-G (only in May 2006 and July 2007).

The final error in the reduced magnitudes was obtained as described in Sec. 3.5.4. For the May 2006 and August 2006 datasets, although minor deviations exist for individual measurements (with smaller error estimates) we adopt a safe overall value of the photometric errors of 0.05 mag.

4.1 Activity at large heliocentric distance: coma

We investigated the presence of coma around the nucleus in all observing epochs. For all datasets we applied two methods:

1. We compared the point spread function (PSF) of the comet with the one of a neighbouring star following the approach described in Böhnhardt et al. (2002). Since the observations are performed with the telescope tracking the comet, stars are trailed. As reference star, we chose a star with a high signal-to-noise ratio. The profile of the reference star is produced from a perpendicular cut through the trail, averaged along the trail axis. The pixels on the edge of the trail are excluded. The radial profile of the comet, instead, is obtained measuring the flux in concentric rings (1 pixel wide) versus the radial distance from the center of the comet. Both star and comet profiles are normalized to have background level to zero and maximum value to one. Apart from minor offsets in the normalized peak magnitude (which is due to

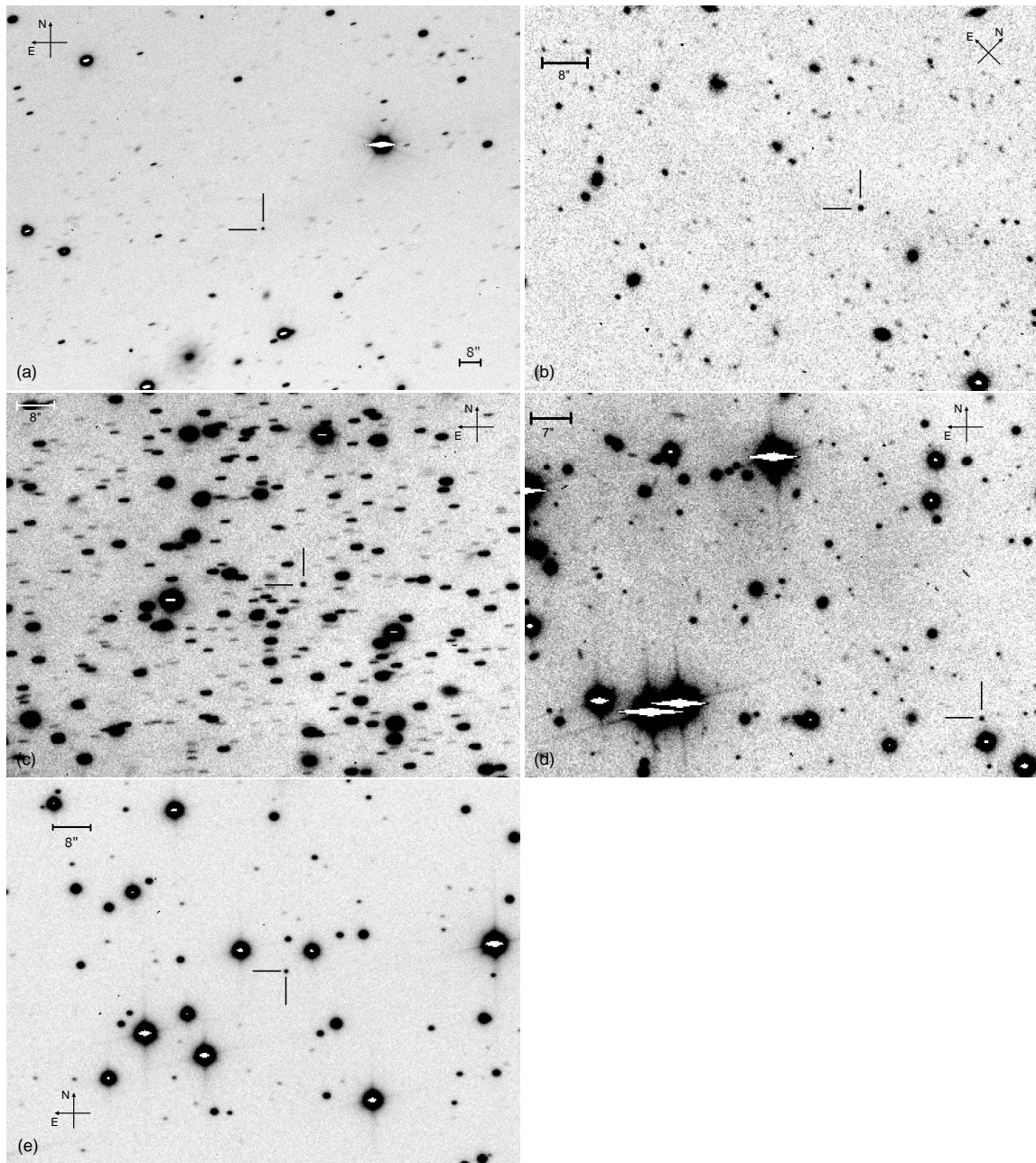


Figure 4.1: R filter images of 67P/C-G taken in April 2004, June 2004, May 2006, August 2006 and July 2007. Image scale and orientation are shown. The position of the comet in the frames is marked. The image taken on May 25, 2006 (c) illustrates the crowdedness of the field at low galactic latitude. Uneven diffuse background is due to galactic clouds.

statistical scatter of the brightest pixel position in the image center) the profiles of the comet and star images are identical, indicating that the PSF is undistinguishable from that of a point source (Fig. 4.5). Therefore, we conclude that no coma activity is detectable around the nucleus. Weak coma activity would be first detected by deviations of the comet PSF from that of the star in the inflection region, just before the profile becomes background-dominated.

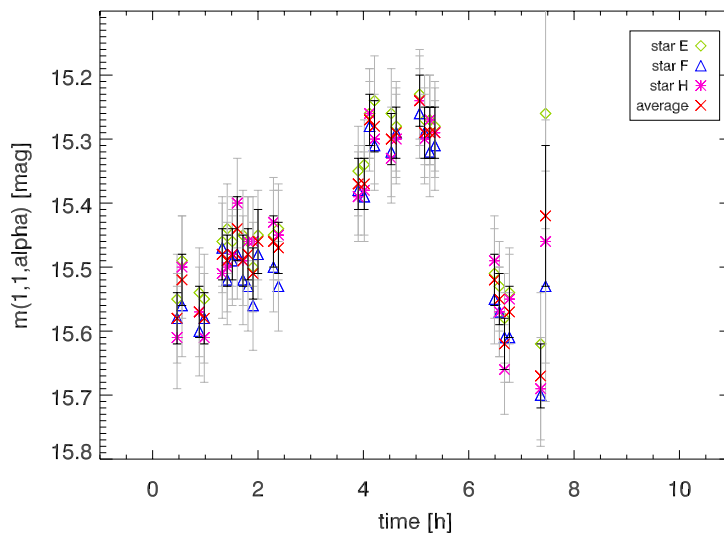


Figure 4.2: R filter reduced magnitude $m(1, 1, \alpha)$ versus time for the April 2004 observation. The comet's magnitude relative to each reference star and the average magnitude per frame are displayed. The time is in hours and it is normalized to April 15, 2004 00:00 UT. The gaps in the time series are due to photometry of the comet done in different filters and rejected measurements because of background object contaminations.

2. We co-add images centered on the comet and searched for diffuse structures around the nucleus in the co-added image. In addition, we applied a smoothing of the co-added images, in order to increase the S/N ratio. No extended structure is visible in the co-added images as well as in the smoothed ones. Figure 4.6 shows one example of co-added image before and after smoothing is applied.

In conclusion, for each observing epoch 67P/C-G appears like a point source, indicating that no coma is evident around the nucleus. For the May 2006 dataset, we estimated that the limiting detectable brightness in the co-added image is 29.8 mag.

Using an individual image of the May 2006 dataset, we determined a $3\text{-}\sigma$ upper limit for the dust production rate of $Af\rho \sim 1.94 \text{ cm}$, which corresponds to a dust production of $Q_d \sim 0.22 \text{ kg/s}$ using a simple heuristic relationship as described by Kidger (2004).

4.2 Rotational period and phase function of the nucleus

The nucleus of comet 67P/C-G, since it is inactive during our observations and presumably has an irregular shape, should exhibit periodic variations in brightness, stimulated by its rotation. This is because the nucleus changes its projected cross-section over the rotational cycle, thus its surface reflects different amounts of light. Assuming shape-dominated variability, the rotational phase profile should feature two main peaks of brightness separated by approximately half of the rotational phase. However, the actual light curve may be quite irregular due to possible irregular albedo and shape variations over the nucleus surface. Brightness changes in the reduced magnitude $m(1, 1, \alpha)$ are induced by the nucleus rotation and the phase darkening. Thus, to have valuable information on both

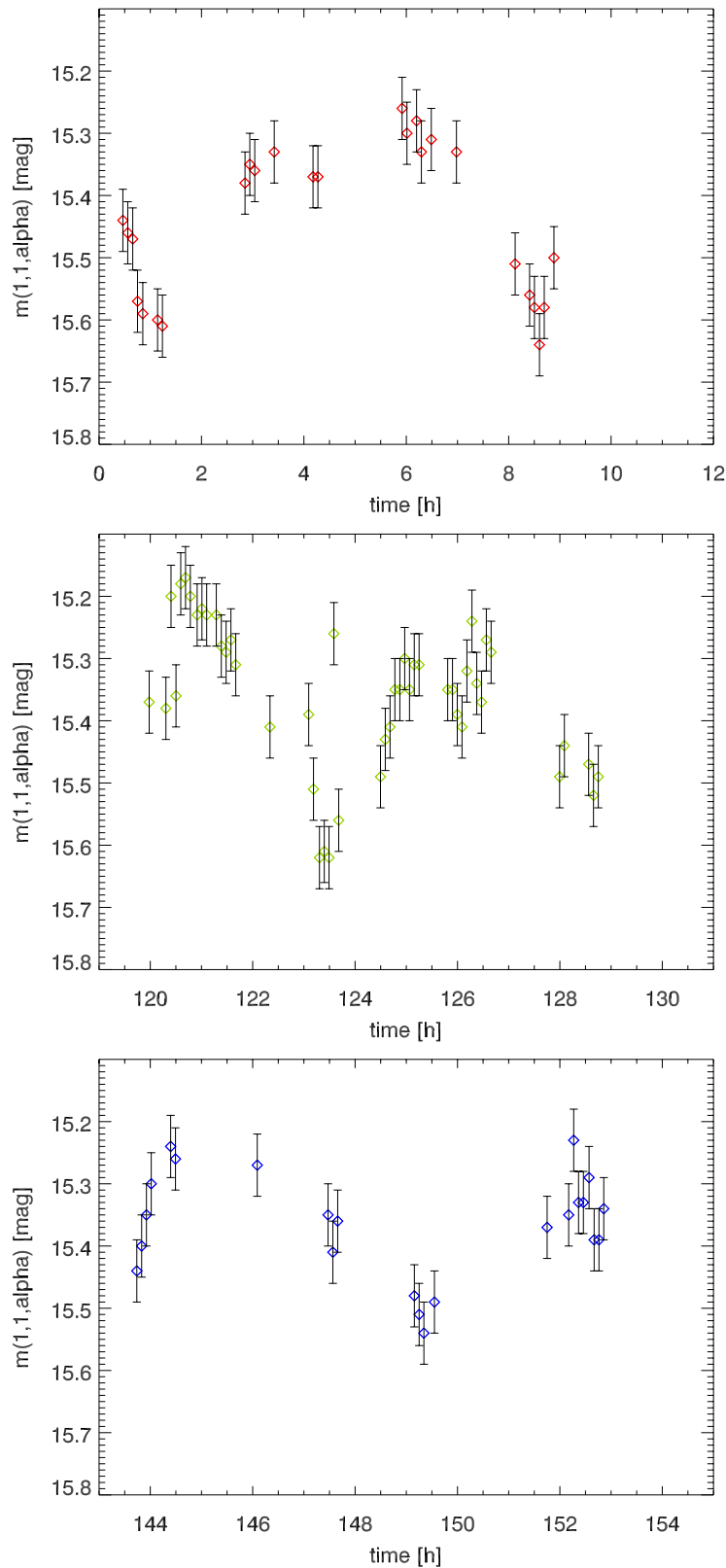


Figure 4.3: R filter reduced magnitude $m(1, 1, \alpha)$ versus time as measured in May 25, 2006 (top panel), May 30, 2006 (middle panel) and May 31, 2006 (bottom panel). The time is in hours and it is normalized to May 26, 2006 00:00 UT. The gaps in the time series are due to photometry of the comet done in different filters, rejected measurements because of background object contaminations and observations of spectra of 67P/C-G.

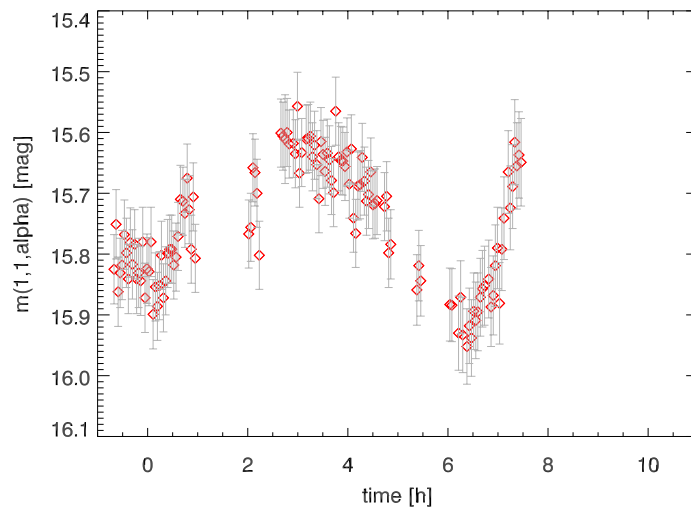


Figure 4.4: R filter reduced magnitude $m(1, 1, \alpha)$ versus time for the July 2007 observation. The time is in hours and normalized to July 17, 2007 00:00 UT. The gaps in the time series are due to photometry of the comet done in different filters, rejected measurements because of background object contaminations and observations of spectra of 67P/C-G.

effects the phase darkening and the nucleus rotation have to be considered and determined simultaneously.

4.2.1 Datasets

The May 2006 dataset is composed of three full nights of observations and spans a time interval of almost one week. Thus, it is most appropriate for a rotational period search. During the three nights of observations, 67P/C-G covered a phase angle range between 0.5° and 1.3° , too small to allow the determination of the phase function of the comet. Since in the other epochs 67P/C-G was at higher phase angle (see Table 3.6), we would like to combine datasets observed in different epochs to determine simultaneously the rotational period and the phase function of 67P/C-G.

First, we determine the rotational period of 67P/C-G combining the May 2006 and the August 2006 datasets. The combination of two datasets has two advantages: 1) the time interval covered by the combined dataset is long and thus the rotational period can be determined with very high accuracy; 2) since in August 2006 67P/C-G was at about 10° of phase angle, we can also determine the phase function of the comet simultaneously with the rotational period. The results from this analysis are described in Sec. 4.2.3.

Then, we performed the same analysis using also the July 2007 dataset in addition to the May 2006 and August 2006 ones (see discussion in Sec. 4.2.4). In July 2007 67P/C-G was at phase angle of about 6° , intermediate between the phase angle in May 2006 and August 2006. Thus, this dataset has an high importance in the determination of the phase function of the comet.

Combining datasets observed in different epochs brings the advantages described above, but also caution has to be taken. In fact, due to the orbital motion of the comet changes of the viewing geometry can occur, which can produce non negligible changes of the mean

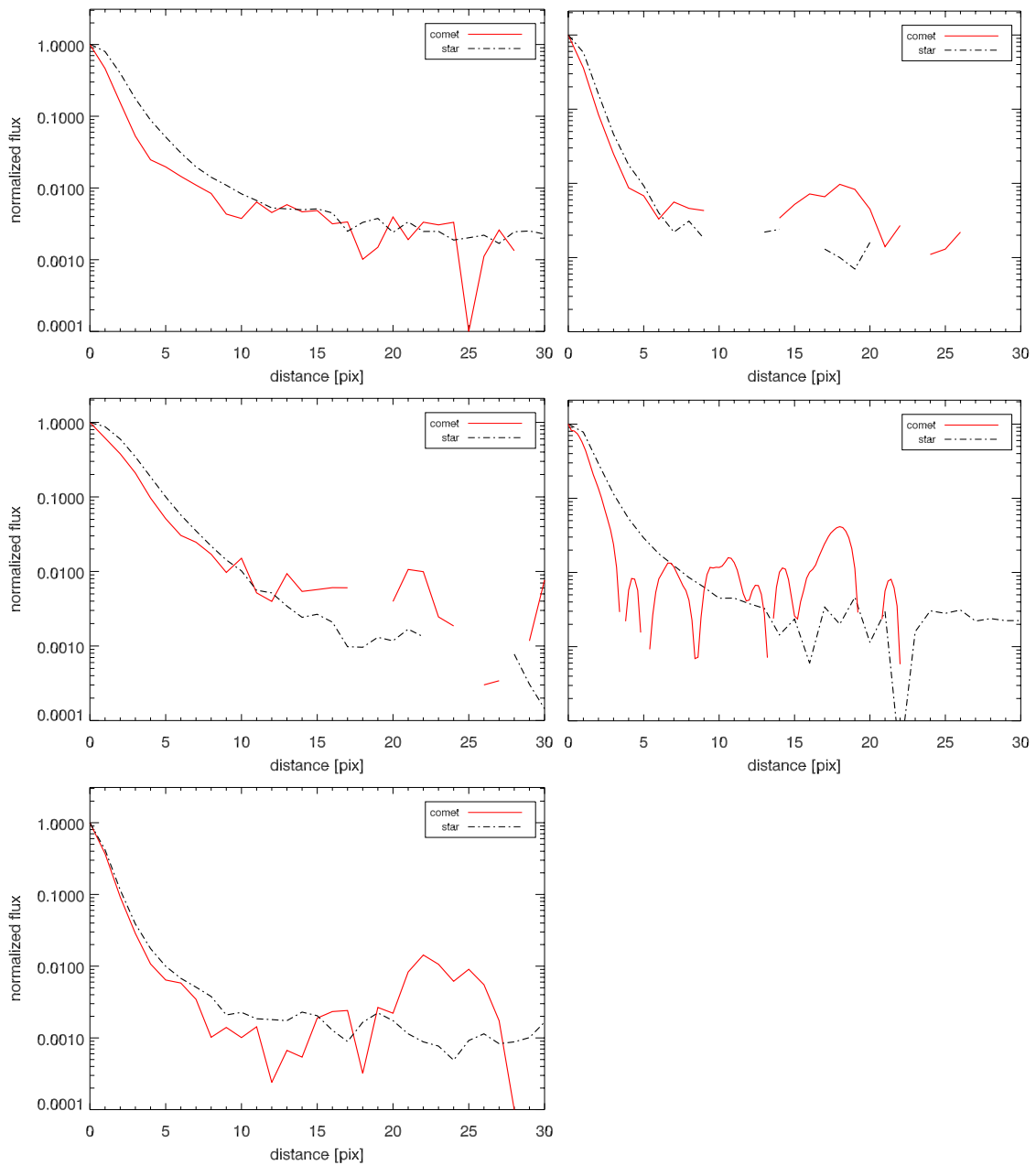


Figure 4.5: Comparison between the profile of the comet (red solid line) and the one of a neighbouring star (black dashed line). The normalized flux is plotted versus the distance (in pixels) from the center of the objects. Panel top left: April 2004 observation, panel top right: June 2004 observation, panel middle left: May 2006 observation, panel middle right: August 2006 observation, panel bottom left: July 2007 observation.

magnitude, amplitude and shape of the light curve. Following the approach of Drahus & Waniak (2006) who adopted the routine by Michałowski (1988), we calculated that the maximum phase shift induced by changes of the observing geometry of 67P/C-G between the May 2006 and August 2006 observations is less than 0.01 at 95% confidence level and the one between the May 2006 and July 2007 runs is 0.13 at 95% confidence level.

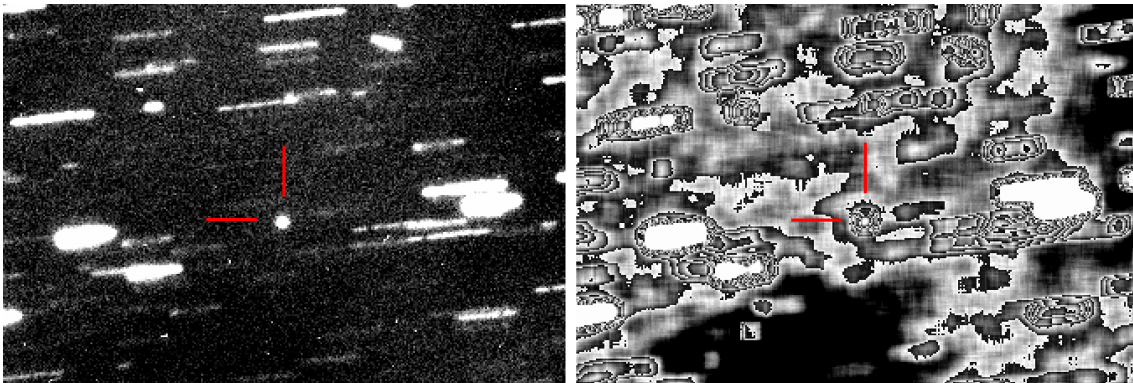


Figure 4.6: Left panel: co-addition of R filter images centered on the comet. The total integration time in the co-added image is 70 minutes. Right panel: co-added image after smoothing is applied. In both panels the position of the comet is marked; the elongated structures are stars.

As input data we used the reduced magnitude $m(1,1,\alpha)$. The May 2006 dataset consists of 95 data points, the August 2006 of 12 and the July 2007 of 126. Thus, the combined dataset May 2006 + August 2006 has 107 data points, while the May 2006 + August 2006 + July 2007 consists of 233 data points.

4.2.2 Method

Performing the periodicity analysis, we generally followed the approach of Drahus & Waniak (2006). Since 67P/C-G was inactive over the time interval considered for the analysis, we chose the phase function coefficient as a second free parameter to be estimated simultaneously with the rotational period. We adopted two approximations for the phase function: the linear approximation with linear phase function coefficient β (Eq. 3.8) and the IAU-adopted phase law with slope parameter G (Eq. 3.9). Two different methods were used as search kernels: the Phase Dispersion Minimization (hereafter PDM), originally proposed by Stellingwerf (1978), and the χ^2 minimization using a sum of harmonics fitted to the observations (hereafter χ^2 minimization). Both methods return, for each value of the trial rotational frequency f and phase coefficient, the quantity Θ whose minima indicate possible periodicities present in the light curve. For PDM, this parameter is defined as $\Theta = \frac{\sigma_{bin}^2}{\sigma_{tot}^2}$, where the numerator is the variance in the phased binned data and the denominator is the total variance of the measured points. For the χ^2 minimization it is defined as $\Theta = \frac{\sigma_{fit}^2}{\sigma_{tot}^2}$, where the numerator is the variance with respect to the smoothed curve and the denominator is the total variance of the measured points. The working parameters of the PDM algorithm are the number of bins N_b and the number of covers N_c . The single parameter of the χ^2 minimization method is the number of frequencies N_f , i.e. the number of harmonics including the base frequency that are used for fitting. For our analysis, we chose $N_b = 25$, $N_c = 5$ and $N_f = 5$. We checked that working with noticeably lower values of these parameters, the methods would not return the whole set of existing solutions, whereas for much higher values they did not provide any additional solutions and were at the same time also less stable due to the limited number of measurements

available. More details about the search kernels can be found in Appendix D. The errors in the frequency (or periodicity) and in the phase function coefficient were retrieved through a Monte Carlo method:

1. Using the χ^2 minimization method, a smooth curve is calculated for the individual data points. Note that here the χ^2 minimization is used for two different purposes: as a method for periodicity search and in order to get a noiseless representation of the phase profile.
2. The smooth profile is modified by “data noise” calculated individually for each observing point, producing a set of simulated light curves. We assumed a Gaussian noise distribution, with its variance given by the square of the error bar.
3. We repeat the procedure for 1000 noise realizations and each of the simulated light curves is then analysed with the PDM and the χ^2 minimization methods. This provides 1000 frequencies and phase function coefficients for each method.

As errors in the frequency and in the phase function coefficient we adopted the standard deviations of these quantities, resulting from each set of the 1000 solutions. This approach naturally converts the observing uncertainties into the errors in the quantities determined.

4.2.3 Results using May 2006 + August 2006 datasets

We first consider the linear approximation for the phase function. We scrutinized the frequency f in the range $\Delta f = 0.02 - 0.8 \text{ h}^{-1}$ ($\Delta T_{rot} = 1.25 - 50 \text{ h}$) and the linear phase coefficient β in the range $\Delta\beta = 0 - 0.2 \text{ mag}^\circ$. Both the PDM and the χ^2 minimization methods show only one clear band of solutions, characterized by considerably deeper minima than any others, which is located around $f = 0.078 - 0.079 \text{ h}^{-1}$ and $\beta = 0.07 - 0.09 \text{ mag}^\circ$. For PDM, the global minimum of Θ was found at $f_1 = 0.078193 \text{ h}^{-1}$ ($T_{rot,1} = 12.7889 \text{ h}$) and $\beta_1 = 0.077 \text{ mag}^\circ$, whereas the χ^2 minimization method returned $f_2 = 0.078711 \text{ h}^{-1}$ ($T_{rot,2} = 12.7047 \text{ h}$) and $\beta_2 = 0.076 \text{ mag}^\circ$. A cross-cut through the whole periodogram for $\beta_2 = 0.076 \text{ mag}^\circ$ and $\beta_1 = 0.077 \text{ mag}^\circ$ and the whole range of frequencies scrutinized is shown in Fig. 4.7, together with a 50–times zoom of the region where the global minima are located. The periodograms clearly show that the band is very complex, featuring several individual solutions. However, the global minimum given by one method (either PDM or χ^2 minimization) is detected as second deepest minimum by the other one (either χ^2 minimization or PDM). This confirms the robustness of the minima found. The difference in frequency between the absolute minima from the two methods is equivalent to the uncertainty of one full rotational cycle between the May and August observing runs; thus for each of the solutions the data are phased very similarly. As mentioned before, also other solutions are visible in between f_1 and f_2 . They are characterized by different rotational phases of the August data and look less realistic (which is reflected by higher values of Θ), but they cannot be completely excluded. Therefore, f_1 and f_2 could also be considered as the extremes of a broader range of possible, although less likely, rotational frequencies. Solutions f_1 and f_2 have practically the same value of linear phase function coefficient β , which is mainly controlled by the large phase angle difference between the May and August observations (see Table 3.6). These best fit β

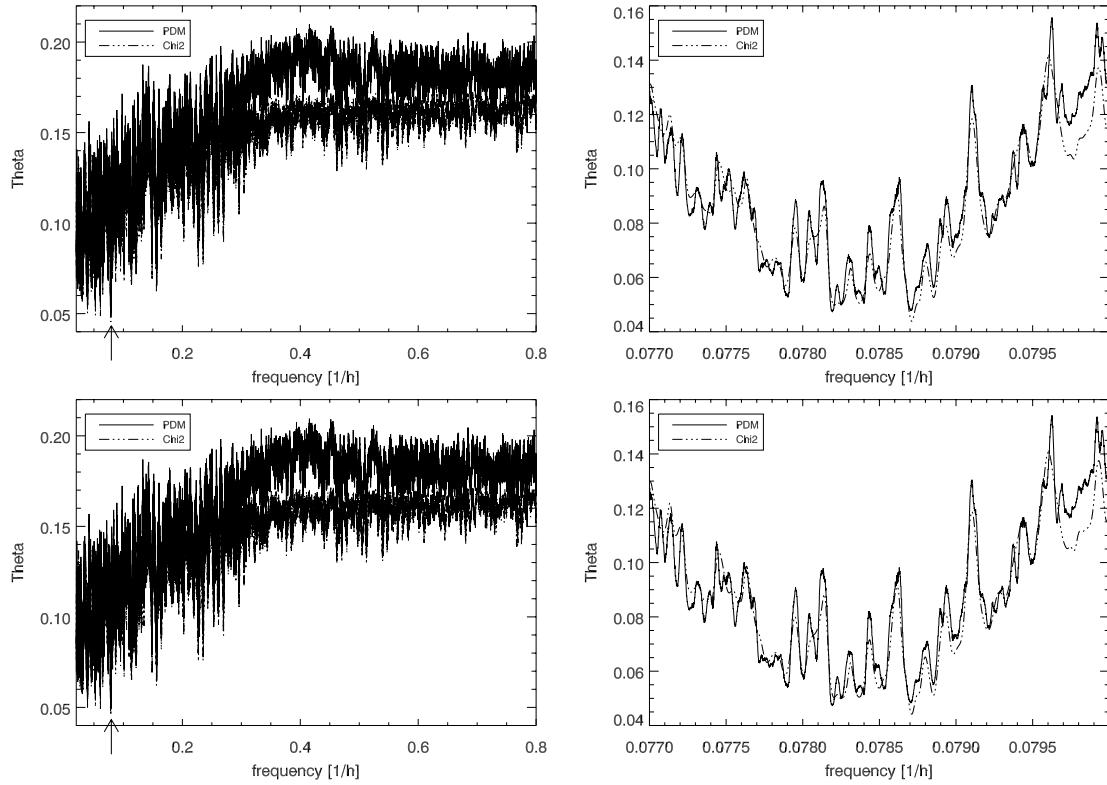


Figure 4.7: Cross-cut through the Θ periodograms for the whole range of frequencies scrutinized (left panels) for fixed values of the linear phase coefficient β ($\beta_2 = 0.076 \text{ mag}^\circ$ (top left panel), $\beta_1 = 0.077 \text{ mag}^\circ$ (bottom left panel)). The regions of the global minima are marked by a black arrow and a 50–times zoom of these regions is plotted in the right panels ($\beta_2 = 0.076 \text{ mag}^\circ$ (top right panel), $\beta_1 = 0.077 \text{ mag}^\circ$ (bottom right panel)). The very low values of Θ result from the normalization of this parameter using the data points which were unphased and uncorrected for the phase angle dependence.

values ($0.077 - 0.076 \text{ mag}^\circ$) correspond to a very steep brightness dependence on phase angle. As described above, for both solutions, the uncertainties of the rotational frequency (and thus the rotational period) and the linear phase function coefficient were estimated using 1000 realizations of Gaussian noise superimposed on smooth representations of the corresponding phase profiles. The smooth fit was calculated with $N_f = 8$, which offers the most realistic curve, such that the dispersion of the data points about the fit was closest to the RMS error of the measured photometry. For both solutions the derived uncertainty in the rotational period T_{rot} is below 5 sec, and the error in the linear phase function coefficient β is 0.003 mag° .

As second step, we consider the IAU-adopted phase law as approximation of the phase function. Since with the previous analysis we identify the frequency region where the minima are located, we restrict the search for periodicities to the aforementioned range. We scrutinized the frequency f in the range $\Delta f = 0.077 - 0.08 \text{ h}^{-1}$ and the slope parameter G in the range $\Delta G = -0.5 - 0.5$. For PDM, the global minimum of Θ was found at $f_3 = 0.078705 \text{ h}^{-1}$ ($T_{rot,3} = 12.7057 \text{ h}$) and $G_3 = -0.08$, whereas the χ^2 minimization method

returned $f_4 = 0.078715 \text{ h}^{-1}$ ($T_{rot,4} = 12.7041 \text{ h}$) and $G_4 = -0.09$. A cross-cut through the periodogram for $G = -0.084$ (mean value of G_3 and G_4) and the frequency region where the global minima are found ($f = 0.077 - 0.08 \text{ h}^{-1}$), is shown in Fig. 4.8.

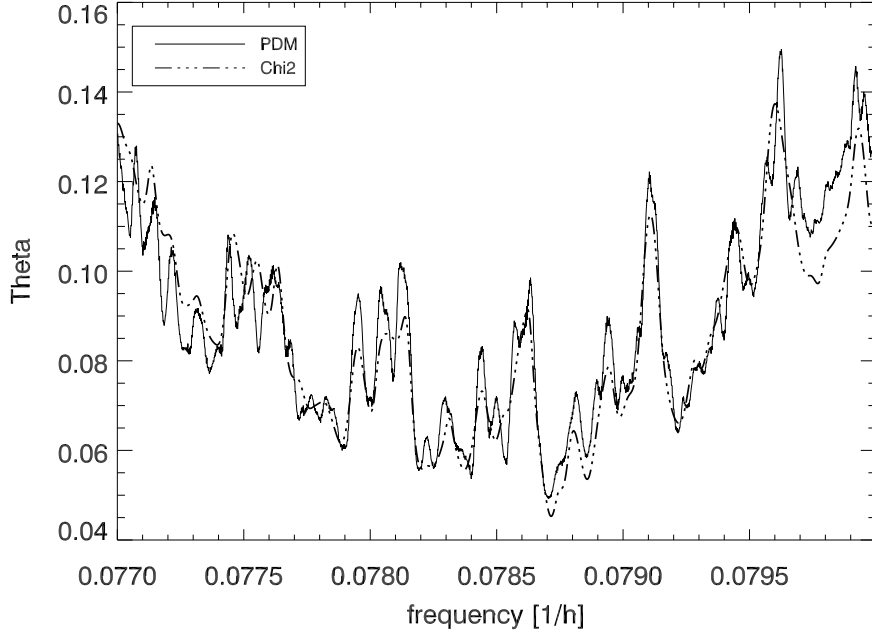


Figure 4.8: Cross-cut through the Θ periodogram for $G = -0.084$ (mean value of G_3 and G_4) and the frequency region where the global minima are found ($f = 0.077 - 0.08 \text{ h}^{-1}$).

Both search kernels found a global minimum located at almost the same frequency and with almost the same slope parameter. Thus, for the determination of the uncertainties in frequency and slope parameter, we considered the mean frequency $f_{mean} = 0.078710 \text{ h}^{-1}$ and the mean slope parameter $G_{mean} = -0.084$. Again, the uncertainties were estimated using 1000 realization of Gaussian noise superimposed on smooth representations of the phase profile. The smooth fit was calculated, in this case, with $N_f = 5$. The PDM method gives an error in the frequency of 0.000009 h^{-1} and in G of 0.021, while the χ^2 minimization method provides an uncertainties of 0.000007 h^{-1} and 0.018 in frequency and slope parameter, respectively. Thus, the effective error in the mean frequency is 0.000008 h^{-1} and the effective error in the mean slope parameter is 0.019.

	$T_{rot} [\text{h}]$	$\beta [\text{mag}^\circ]$
Solution 1	12.7889 ± 0.0009	0.077 ± 0.003
Solution 2	12.7047 ± 0.0011	0.076 ± 0.003
	$T_{rot} [\text{h}]$	G
Solution 3-4	12.7049 ± 0.0013	-0.084 ± 0.019

Table 4.1: Best solutions for rotational periods and phase coefficients of 67P/C-G using the May and August 2006 photometry of the nucleus. Solutions 1 and 2 have been obtained assuming a linear approximation of the phase function, while solution 3-4 assuming the IAU-adopted phase law.

The results obtained with both phase function approximations are summarized in Table 4.1 and the phase profiles corresponding to these rotational periods and phase coefficients are plotted in Fig. 4.9 and Fig. 4.10.

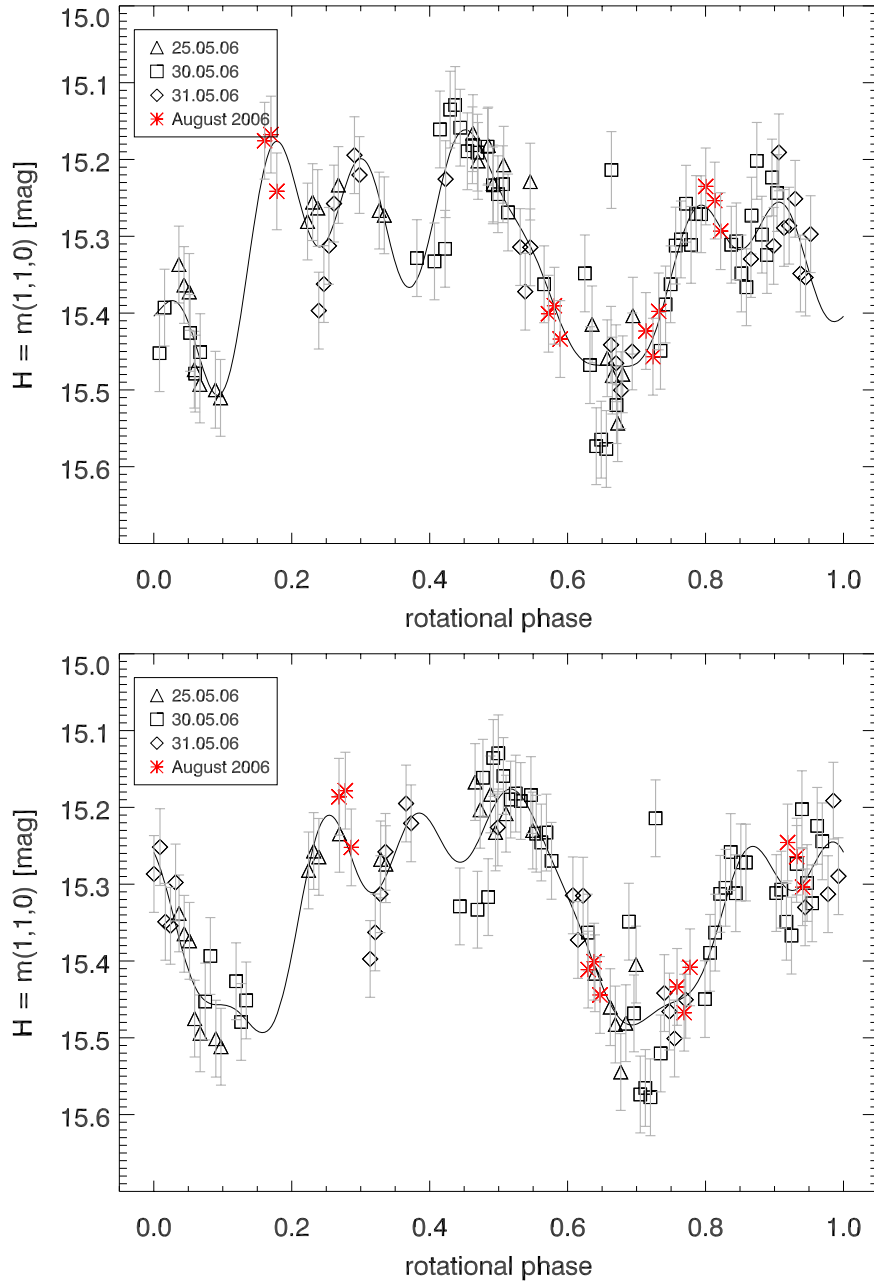


Figure 4.9: Rotational phase profiles of both solutions for the fit assuming a linear phase function (top panel: $T = 12.7889 \pm 0.0009$ h, $\beta = 0.077 \pm 0.003$ mag/°; bottom panel: $T = 12.7047 \pm 0.0011$ h, $\beta = 0.076 \pm 0.003$ mag/°). The smooth curves were calculated using the χ^2 minimization method with $N_f = 8$. They were used as reference profiles for calculating the errors of the solutions.

The global minimum obtained using the IAU-adopted phase law is identical within the uncertainties to solution 2 obtained with the linear phase function approximation. This

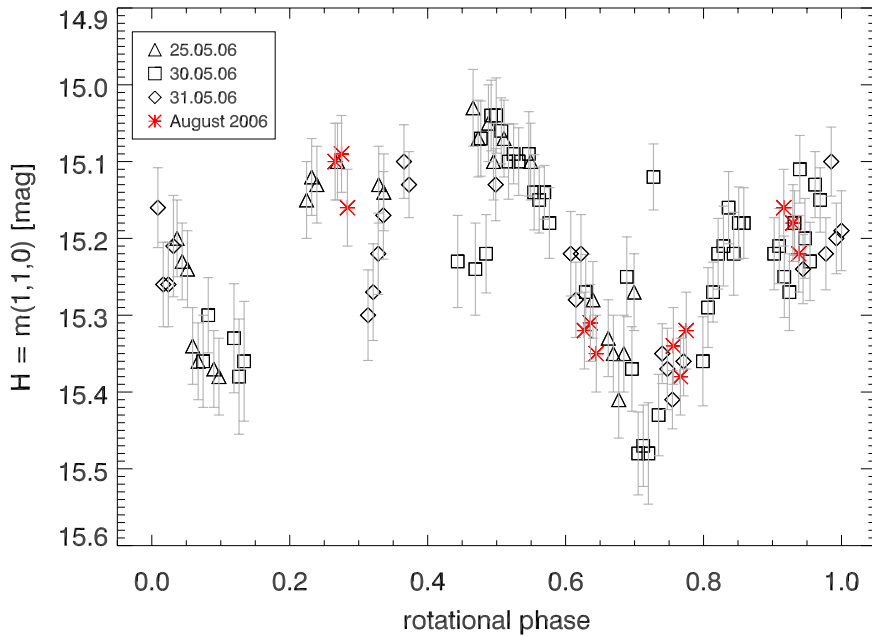


Figure 4.10: Rotational phase profiles for the solution assuming the IAU-adopted phase law as approximation of the phase function ($T = 12.7049 \pm 0.0013$ h, $G = -0.084 \pm 0.019$).

suggests that solution 2 is very robust, being insensitive to the mathematical form of the phase function used.

4.2.4 Results using May 2006 + August 2006 + July 2007 datasets

We restricted the ranges of variability of the parameters (frequency, linear phase coefficient and slope parameter) to the ones where the solutions were found with the previous analysis employing the May 2006 and August 2006 datasets. Thus, we scrutinized the frequency f in the range $\Delta f = 0.077 - 0.08$ h⁻¹, the linear phase coefficient β in the range $\Delta\beta = 0.04 - 0.1$ mag/° and the slope parameter G in the range $\Delta G = -0.15 - 0.45$. Both the PDM and the χ^2 minimization methods returned a number of possible solutions for the rotational period and phase coefficient of 67P/C-G, as shown in Fig. 4.11, where adaptive cross-cuts through the Θ periodogram for the range of frequencies scrutinized are displayed.

While for the May 2006 + August 2006 datasets we extract cross-cuts through the Θ periodogram for fixed values of phase coefficient, in this case for each frequency value we select the phase coefficient (β or G) value for which Θ is minimum.

The quality of the periodogram, indicated by the Θ parameter, obtained using the linear approximation of the phase function is systematically better than the one obtained from the IAU-adopted phase law. Comparing Fig. 4.7 and 4.8 with Fig. 4.11, it is obvious that the difference in the quality of the periodograms obtained using the two different phase function approximations, is much more pronounced when employing also the July 2007 dataset in the analysis. We conclude that, considering the aforementioned dataset, obtained when 67P/C-G was at phase angle of about 6° , the linear approximation best represents the phase function of 67P/C-G. Thus, from now on, we focus our attention only

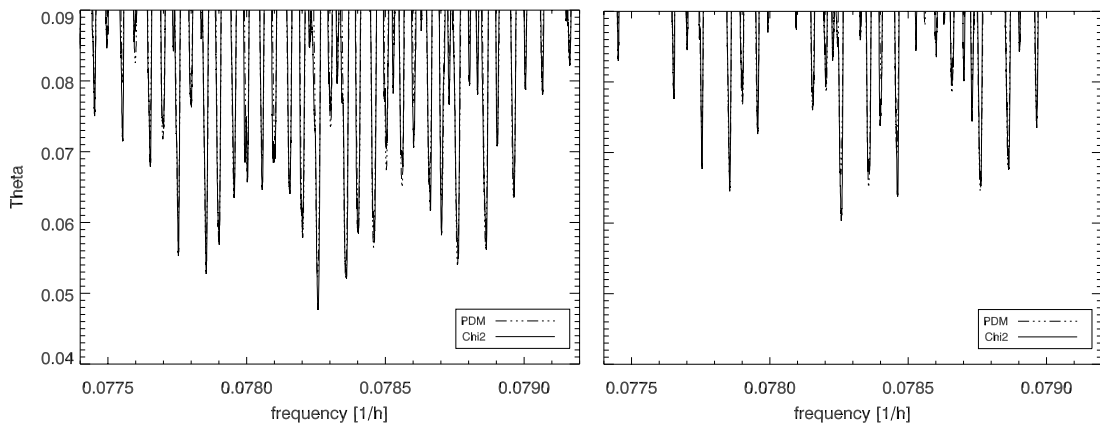


Figure 4.11: Adaptive cross-cuts through the periodograms for the PDM and the χ^2 methods using the linear approximation for the phase function (left panel) and the IAU-adopted one (right panel).

on the results obtained assuming a linear phase function approximation. Table 4.2 summarizes the best solutions for rotational period and linear phase coefficient of 67P/C-G. Since the PDM and the χ^2 minimization methods returned, per each solution, very close values of rotational period and linear phase coefficient, for each solution we determined their mean values. The corresponding rotational phase profiles are displayed in Fig. 4.12 and 4.13. Based on the values of the linear phase coefficient, the solutions displayed in Table 4.2 can be divided in two groups. Group 1 (solutions 5,6,8,9,12,13) represents a steeper dependence of brightness with phase angle, while in group 2 (solutions 7,10,11) the dependance is shallower. The linear phase coefficients in group 1 coincide, within the uncertainties, with the β value determined employing the May 2006 + August 2006 datasets only.

The overall shape of the rotational phased light curve is the same for all the rotational periods and linear phase coefficients used. 67P/C-G shows an asymmetric double peak profile. The main peak is wider and brighter than the secondary one and it presents a modulation which is not seen in the secondary peak. The minima in the light curve are narrow.

The July 2007 dataset is phased differently depending if the rotational period used belongs to group 1 or to group 2. In fact, in the former case the main peak of the July 2007 partial light curve is located at rotational phase of about 0.5, while in the latter case at rotational phase of about 0.9. Also the August 2006 dataset is phased in slightly different ways according to the rotational period and linear phase coefficient considered. If we assume that the light curve did not change over the orbital motion of the comet, the three solutions belonging to group 2 display the August 2006 dataset systematically offset with respect to the May 2006 and July 2007 datasets. Thus, under this hypothesis, the aforementioned solutions look less realistic than the others, and they might be rejected. Ignoring the hypothesis of no light curve changes over the orbital motion, a discrimination among solutions is not uniquely possible.

The minima in the periodogram (Fig. 4.11) are equally wide, which indicates that the uncertainties in the rotational period and linear phase coefficient are comparable for all solutions. Thus, we calculate the errors only for one solution (solution 9) and we

	T_{rot} [h]	β [mag/°]	method	$T_{rot,mean}$ [h]	β_{mean} [mag/°]
solution 5	12.6805	0.075	χ^2	12.6803 ± 0.0002	0.074 ± 0.002
	12.6801	0.073	PDM		
solution 6	12.6968	0.074	χ^2	12.6966 ± 0.0002	0.073 ± 0.002
	12.6964	0.072	PDM		
solution 7	12.7546	0.063	χ^2	12.7546 ± 0.0002	0.063 ± 0.002
	12.7546	0.063	PDM		
solution 8	12.7621	0.075	χ^2	12.7619 ± 0.0002	0.075 ± 0.002
	12.7617	0.075	PDM		
solution 9	12.7786	0.075	χ^2	12.7786 ± 0.0002	0.074 ± 0.002
	12.7785	0.073	PDM		
solution 10	12.7874	0.064	χ^2	12.7875 ± 0.0002	0.064 ± 0.002
	12.7875	0.064	PDM		
solution 11	12.8370	0.062	χ^2	12.8369 ± 0.0002	0.062 ± 0.002
	12.8368	0.061	PDM		
solution 12	12.8446	0.073	χ^2	12.8446 ± 0.0002	0.073 ± 0.002
	12.8446	0.073	PDM		
solution 13	12.8612	0.074	χ^2	12.8612 ± 0.0002	0.075 ± 0.002
	12.8611	0.075	PDM		

Table 4.2: Best solutions for rotational period and linear phase function coefficient β for 67P/C-G using the May 2006, August 2006 and July 2007 photometry of the nucleus. $T_{rot,mean}$ and β_{mean} are the mean values of the rotational periods (T_{rot}) and linear phase coefficients (β), respectively, determined with the PDM and the χ^2 minimization methods.

adopt them for all the other solutions. Moreover, since the PDM and the χ^2 minimization methods returned, per each solution, very close values of rotational period and linear phase coefficient, for the determination of the uncertainties we consider their mean values. Also in this case, the uncertainties were estimated using 1000 realization of Gaussian noise superimposed on smooth representations of the phase profile. The smooth fit was calculated with $N_f = 8$. The effective error in the the rotational period is 0.0002 h and the one in the linear phase coefficient is 0.002 mag/°.

4.2.5 Discussion

The quality of the periodogram, indicated by the Θ parameter, is systematically better when we employ in the analysis the linear approximation of the phase function rather than the IAU-adopted one. Thus, we consider the linear approximation the more realistic representative of the phase function of 67P/C-G. This could be interpreted that for 67P/C-G, the opposition effect is rather not very pronounced. This conclusion is also supported by the behaviour of the reduced magnitude $m(1, 1, \alpha)$ versus phase angle for all our datasets, as shown in Fig. 4.14, where the mid-point R filter magnitude is plotted versus phase angle. The mid-point magnitude is defined as the mean value between the maximum and the minimum magnitude of the light curve. Since in August 2006 the phase angle is almost constant during the nights of observation, one single value has been calculated

4.2 Rotational period and phase function of the nucleus

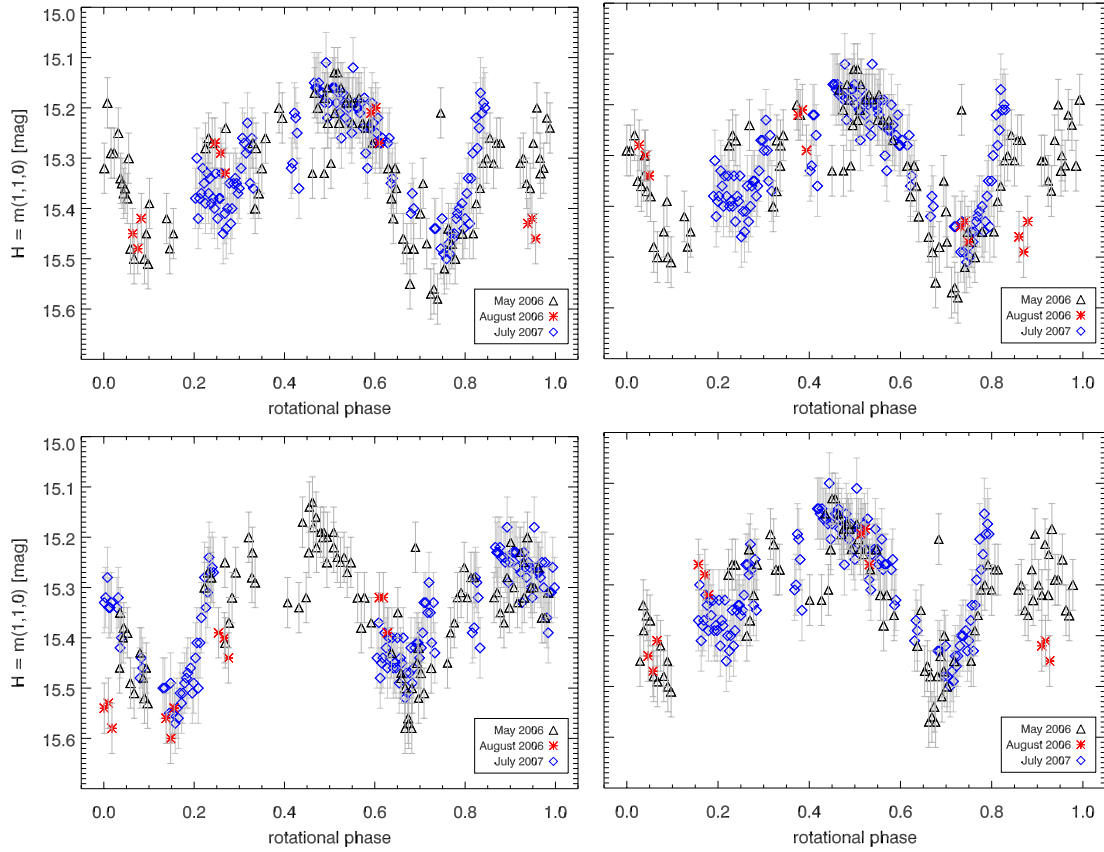


Figure 4.12: Rotational phase profiles for the solutions $(T_{rot,mean}, \beta_{mean})$ summarized in Table 4.2 (solutions 5 to 8).

for the whole observing run. The data show a very steep increase of brightness with decreasing phase angle and they support the hypothesis of a constant linear increase. The slopes corresponding to a linear phase coefficient $\beta = 0.076 \text{ mag}^\circ$, representative for solutions of group 1, and $\beta = 0.063 \text{ mag}^\circ$, representative, instead, of solutions belonging to group 2, are overplotted to the data. The steeper brightness dependence on phase angle ($\beta = 0.076 \text{ mag}^\circ$) seems to be in a better agreement with the data.

We determined the absolute magnitude of the April 2004 and June 2004 runs using $\beta = 0.076 \text{ mag}^\circ$ and $\beta = 0.063 \text{ mag}^\circ$. The partial light curves from the April 2004 and June 2004 observations are overplotted to the phase profiles of 67P/C-G previously determined, after being arbitrarily shifted in rotational phase to match best (estimated by eye) the rotational light curve (Fig. 4.15).

The difference between the two phased profiles is given by the June 2004 and August 2006 datasets, mainly. Since they have been observed at phase angle of about 10° , they are most sensitive to changes of the linear phase coefficient.

Under the hypothesis of no light curve changes over the orbital motion of the comet, we can conclude that the brightness dependence on phase angle is very steep and it is not well reproduced by linear phase coefficient of $\beta = 0.063 \text{ mag}^\circ$. This is supported by the fact that the June 2004 and August 2006 datasets are systematically offset with respect to the other datasets. Ignoring this hypothesis, we can just conclude that light curve changes

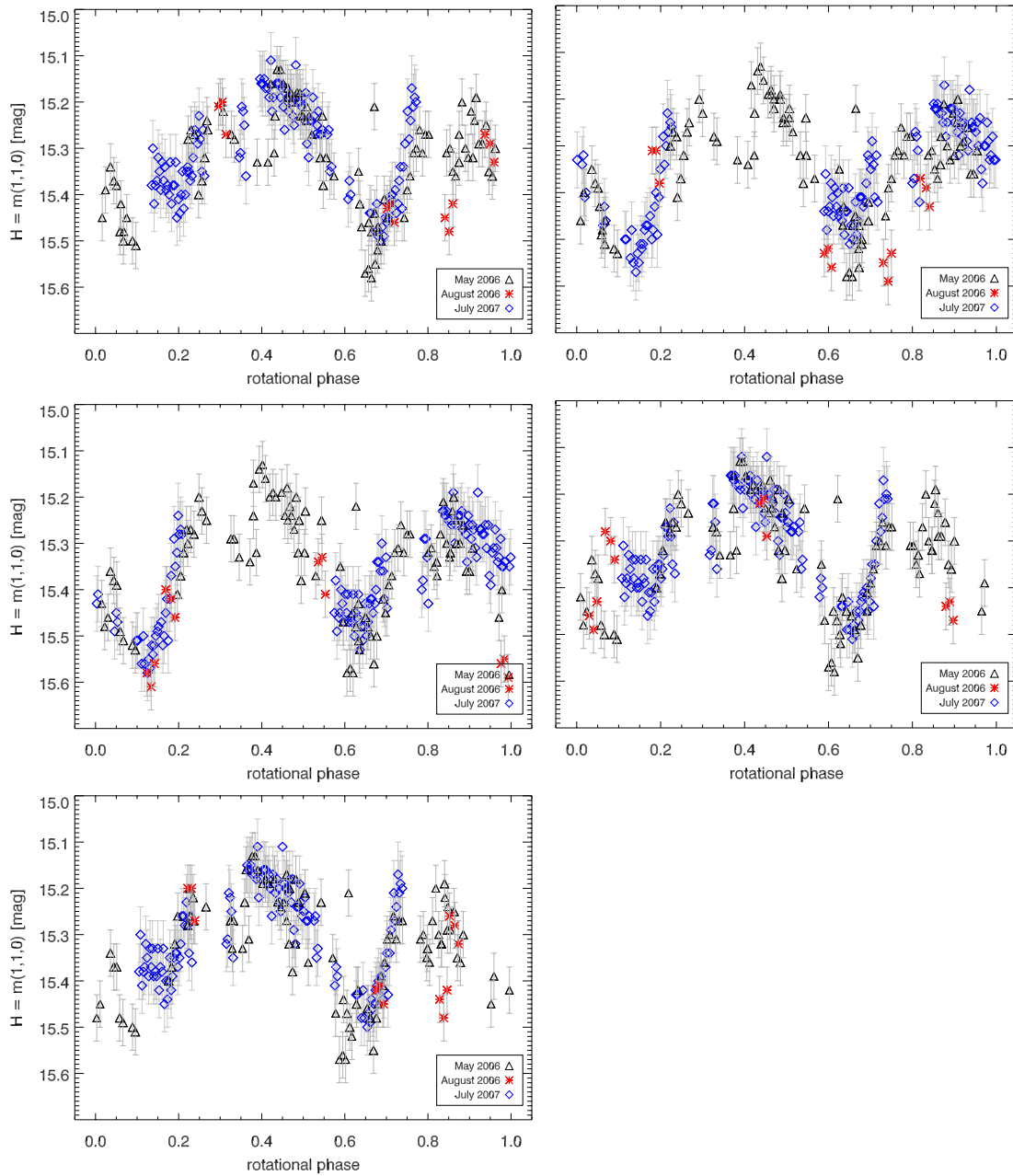


Figure 4.13: Rotational phase profiles for the solutions $(T_{rot,mean}, \beta_{mean})$ summarized in Table 4.2 (solutions 9 to 13).

took place over the orbital motion of 67P/C-G.

Considering also the July 2007 dataset in the determination of the rotational period and linear phase coefficient of 67P/C-G, the intrinsic accuracy of the period estimation is improved. Unfortunately, a discrimination among solutions is not uniquely possible. This is due to the large time gap between the different datasets used for the analysis. Thus, we can only conclude that the rotational period and linear phase coefficient of 67P/C-G are in the range $T_{rot} = 12.6801 - 12.8612$ h and $\beta = 0.061 - 0.076$ mag $^\circ$, respectively, which

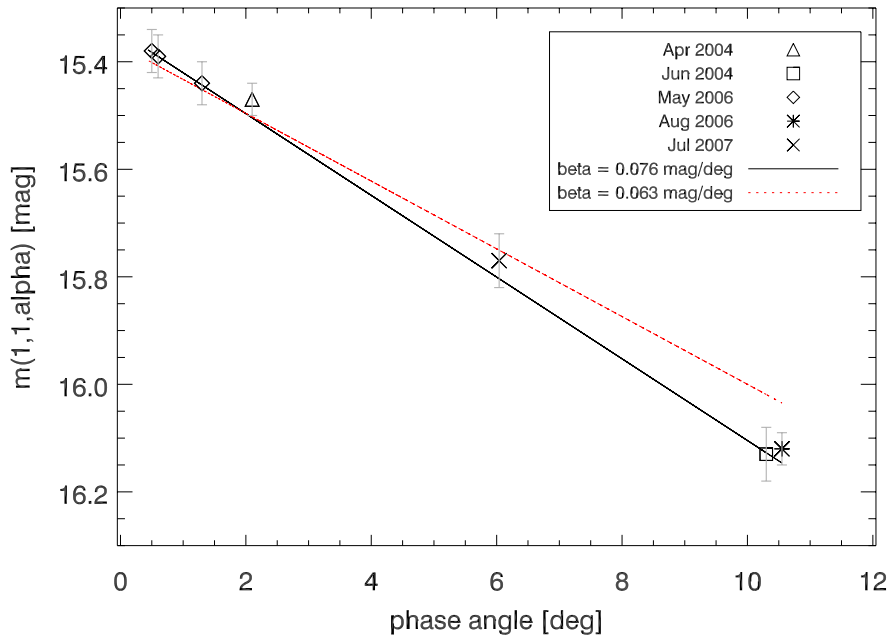


Figure 4.14: Reduced magnitude vs. phase angle. The values correspond to the mid-point magnitude in R filter. The different symbols correspond to the different datasets. The black solid line indicates the slope of $\beta = 0.076 \text{ mag}^\circ$, while the red dotted one represents the slope of $\beta = 0.063 \text{ mag}^\circ$.

contains also the solution obtained employing the May 2006 + August 2006 datasets only.

4.3 Shape and size of the nucleus

For the determination of shape and size of the nucleus of 67P/C-G we are interested in the amplitude of the light curve and on its mean brightness, as discussed in Sec. 1.1.1. These two parameters (amplitude and mean brightness) are independent from the rotational period and linear phase coefficient employed, since the overall shape of the light curve is not changing. The light curve has an asymmetric, double-peak profile with a maximum amplitude $\Delta m = 0.40 \pm 0.07 \text{ mag}$ and mean absolute R filter magnitude $H = 15.35 \pm 0.04 \text{ mag}$. Assuming an ellipsoidal shape for the nucleus, with semi-major axes a and b and constant surface albedo, we can estimate a lower limit for the axis ratio using:

$$\frac{a}{b} \geq 10^{-0.4 \cdot \Delta m} = 1.45 \pm 0.09. \quad (4.1)$$

Assuming an albedo of 0.04 (Lamy et al. 2004), the effective radius of the nucleus of 67P/C-G is:

$$R_{eff} = \left[\frac{10^{0.4[M_\odot - H]}}{A} \right]^{1/2} = 2.38 \pm 0.04 \text{ km}, \quad (4.2)$$

where M_\odot is the absolute magnitude of the Sun in the R filter, H the mean absolute R filter magnitude of the comet and A its albedo.

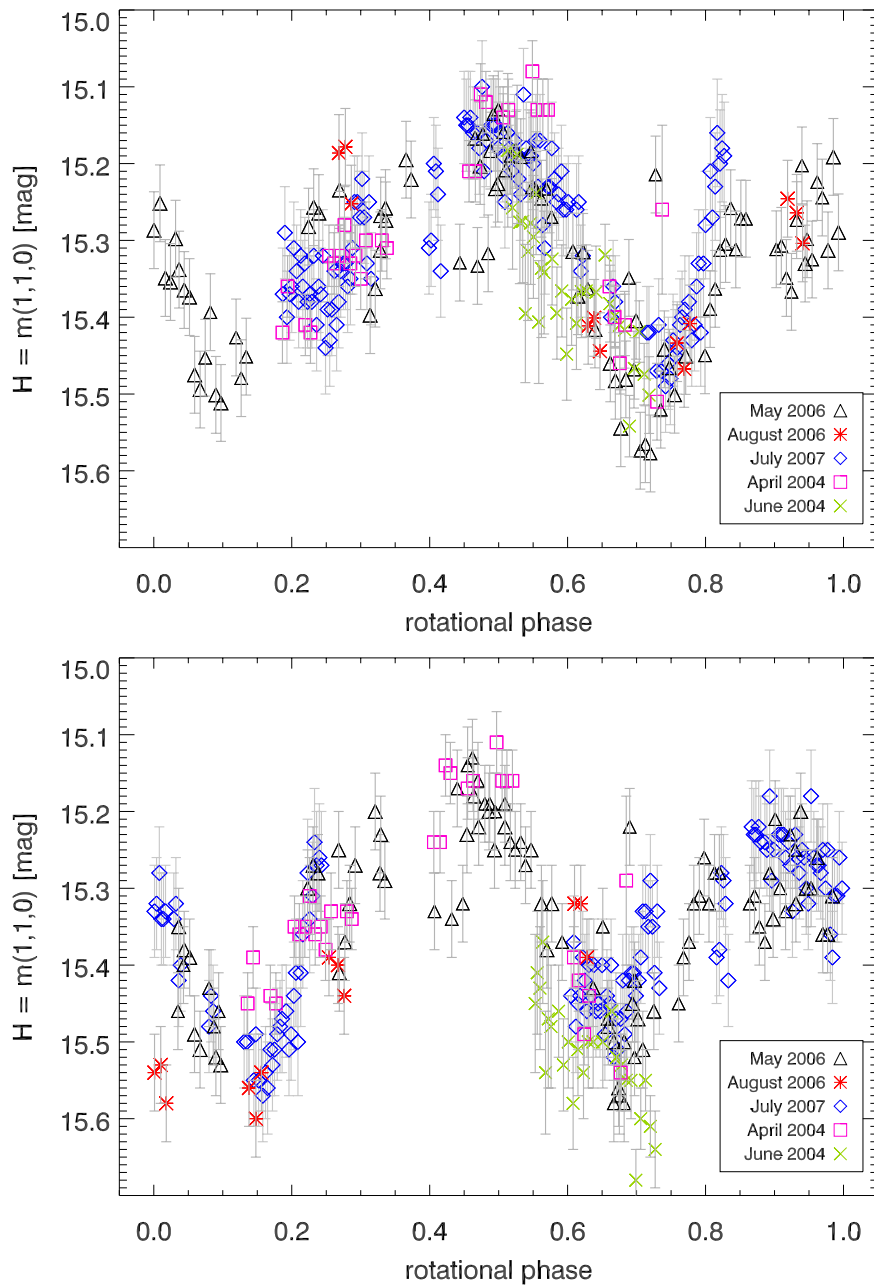


Figure 4.15: Phased light curves of 67P/C-G representative of group 1 (top panel) and group 2 (bottom panel), overplotted with the observations of April 2004 and June 2004 phase corrected using $\beta = 0.076 \text{ mag}^\circ$ (top panel) and $\beta = 0.063 \text{ mag}^\circ$ (bottom panel) and arbitrarily located in rotational phase.

4.4 Surface colors and reflectance spectra of the nucleus

The color indices V-R and R-I were obtained from the April 2004, June 2004, May 2006 and July 2007 observations. In the last epoch, thanks to observations also in the B Bessell filter, we determined also the B-R color index (see Table 4.3). The August 2006 observations have been performed in R filter only, thus the determination of color indices is

not possible. The color indices show that the nucleus of 67P/C-G is slightly redder than the Sun ($(V-R)_{\odot} = 0.36$ mag, $(R-I)_{\odot} = 0.33$ mag, $(B-R)_{\odot} = 1.03$ mag), as expected for cometary nuclei (Lamy et al. 2004). V, I and B filter images of the comet were obtained at different rotational phases, thus the resulting color indices sample different regions of the nucleus surface (Table 4.3). Since the July 2007 dataset is phased differently depending if the rotational period used belongs to group 1 or to group 2 (Sec. 4.2.4), the rotational phase of the color indices relative to this dataset has the same dependence. Thus, we determined the rotational phase for both cases.

	V-R [mag]	R-I [mag]	B-R [mag]	ϕ
April 2004	0.50 ± 0.04	0.51 ± 0.04	–	0.2
	0.55 ± 0.05	0.47 ± 0.05	–	0.3
	0.53 ± 0.03	0.47 ± 0.03	–	0.5
	0.53 ± 0.04	–	–	0.7
June 2004	0.38 ± 0.04	0.44 ± 0.06	–	0.6
25 May 2006	0.49 ± 0.06	–	–	0.1
	0.65 ± 0.07	0.45 ± 0.04	–	0.3
	0.66 ± 0.08	0.47 ± 0.05	–	0.5
30 May 2006	–	0.40 ± 0.09	–	0.6
	0.55 ± 0.08	0.39 ± 0.07	–	0.9
31 May 2006	0.44 ± 0.08	–	–	0.4
	0.46 ± 0.07	0.54 ± 0.06	–	0.8
	0.50 ± 0.06	0.57 ± 0.06	–	0.9
July 2007	0.54 ± 0.05	0.45 ± 0.04	1.37 ± 0.06	$0.7^*, 0.1^{\diamond}$
	–	0.47 ± 0.06	–	$0.7^*, 0.1^{\diamond}$

Table 4.3: Color indices of 67P/C-G as determined from the photometric observations in April 2004, June 2004, May 2006 and July 2007. ϕ is the rotational phase at which V, I and B filter images, used to determine the corresponding color indices, were taken. July 2007 dataset: the rotational phase relative to rotational periods belonging to group 1 is marked by a star, while the one relative to rotational periods belonging to group 2 is marked by a diamond.

The values for R-I index are rather uniform. The V-R indices, in particular on May 25, show a larger scatter, in parts due to the too small number of measurements performed in V filter. In fact, only one single V filter image was taken per epoch. Although slightly outside the error bars of the other V-R results, the higher V-R colors (0.65 ± 0.07 mag and 0.66 ± 0.08 mag) are still consistent with the measured spectra of the cometary nucleus (see Fig. 4.16). For each couple of V-R and R-I colors in Table 4.3, we determined the mean spectral reddening (Delsanti et al. 2001) and found it to be rather constant within the error bars, except for the June 2004 dataset. Thus, we conclude that color variations with the rotational phase are small, if present at all. The average color indices of the nucleus of 67P/C-G are summarized in Table 4.4, together with the corresponding mean spectral reddening. Note that in July 2007, since observations in B Bessell filter are also available, the mean spectral reddening has been determined in the wavelength range 4360 – 7970 Å in addition to the one in the wavelength range 5450 – 7970 Å. The mean spectral

reddening is the same for both wavelength ranges.

	V-R [mag]	R-I [mag]	B-R [mag]	reddening [%/1000 Å]
April 2004	0.53 ± 0.02	0.49 ± 0.02	–	12 ± 2
June 2004	0.38 ± 0.04	0.44 ± 0.06	–	5 ± 3
May 2006	0.54 ± 0.03	0.47 ± 0.03	–	11 ± 2
July 2007	0.54 ± 0.05	0.46 ± 0.04	1.37 ± 0.06	$10 \pm 2^\circ, 11 \pm 2^*$

Table 4.4: Average color indices of 67P/C-G as determined from the photometric observations in April 2004, June 2004, May 2006 and July 2007. The corresponding mean spectral reddening is shown. For April 2004, June 2004 and May 2006 it has been calculated in the wavelength range 5450 – 7970 Å. In July 2007, in addition to the one relative to the wavelength range 5450 – 7970 Å (marked by °), thanks to observations also in B filter we determined the mean spectral reddening also in the wavelength range 4360 – 7970 Å (marked by *).

Visible spectra of the comet were observed on May 25 and May 31, 2006 and July 16, 2007. Let us consider, first, the spectra obtained in May 2006. Two spectra have been discarded because of unreasonable spectral shapes possibly caused by a background object passing close to the comet slit position while integrating the spectrum. Each spectrum is binned to 70 Å/pix. Figure 4.16 shows the binned spectra (dotted line) of 67P/C-G with the smoothed ones (solid line) superimposed.

Spectra (a) and (b) have been observed at rotational phase between 0.4 and 0.5, while (c) and (d) at rotational phase between 0.8 and 0.95. The S/N ratios and the corresponding relative errors in the individual binned spectra are summarized in Table 4.5. The spectra do not show any absorption or emission features. In the wavelength range 5000 – 8500 Å the binned spectra display a reddening of rather constant slope of (11 ± 2) %/1000 Å (a), (10 ± 1) %/1000 Å (b), (13 ± 1) %/1000 Å (c) and (10 ± 2) %/1000 Å (d). The reddening obtained from the spectra agrees within the errors with the one calculated from the photometric color indices of the nucleus (see Fig. 4.16 and Table 4.4).

One spectrum of 67P/C-G was observed in July 2007; it is displayed in Fig. 4.17 (upper panel) with the binned spectrum superimposed (binning to 70 Å/pix). The S/N ratios and the corresponding relative errors in the binned spectrum at the different wavelengths are summarized in Table 4.6. The spectrum observed in July 2007 has a signal-to-noise ratio of about 3 times higher than the ones of May 2006.

Again the spectrum does not show any absorption or emission features and it displays a reddening of rather constant slope of (12 ± 1) %/1000 Å in the wavelength range 4300 – 8500 Å. In the wavelength range 5000 – 8500 Å (the same used for the May 2006 spectra) the spectral reddening is (11 ± 1) %/1000 Å, in agreement with the result obtained for the May 2006 photometry and spectroscopy.

Color indices and the reflectance spectrum were obtained at different rotational phases, thus they sample different regions of the nuclear surface. A good agreement exists between them (see Fig. 4.17, bottom panel) which suggests that no color variations took place with rotational phase.

In conclusion, all the spectra we observed do not show any absorption or emission feature. They display a constant spectral reddening with rotational phase which is also in

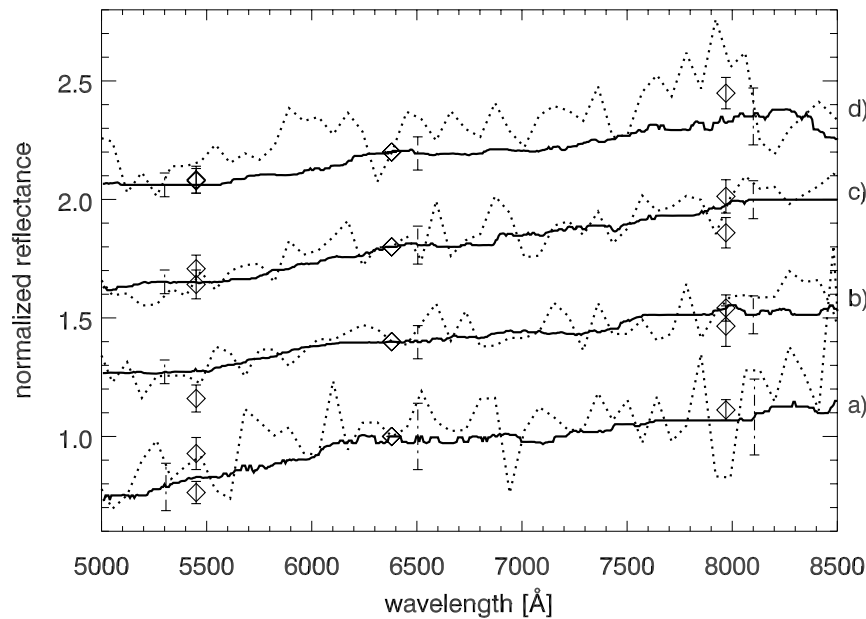


Figure 4.16: Spectra of 67P/C-G obtained in May 2006. To each binned spectrum (dotted line) the corresponding smoothed one (solid line) is superimposed. Spectrum (a) has been observed on May 25, while (b), (c) and (d) have been taken on May 31, 2006. The spectra are normalized to unity at 6380 Å and shifted for clarity. The diamonds superimposed to the spectra correspond to the spectral reflectivities obtained from the photometric color indices of the nucleus, closest in rotational phase. The dashed bars aside the diamonds show the uncertainties in the binned reflectance spectra in each wavelength region, as summarized in Table 4.5.

spectrum	λ [Å]	S/N	error
a	5000 – 5140	10	0.10
	6500 – 6640	7	0.14
	8000 – 8140	6	0.16
b	5000 – 5140	21	0.05
	6500 – 6640	14	0.07
	8000 – 8140	13	0.08
c	5000 – 5140	19	0.05
	6500 – 6640	13	0.08
	8000 – 8140	13	0.08
d	5000 – 5140	19	0.05
	6500 – 6640	15	0.07
	8000 – 8140	8	0.12

Table 4.5: Signal-to-noise ratio (S/N) and corresponding relative error in the binned spectra shown in Fig. 4.16. λ (Å) is the wavelength range used for the determination of S/N ratio and the error.

agreement with the previous conclusion of no (or only small) photometric color variation of the nucleus with rotational phase. Thus, we conclude that the nucleus color and/or

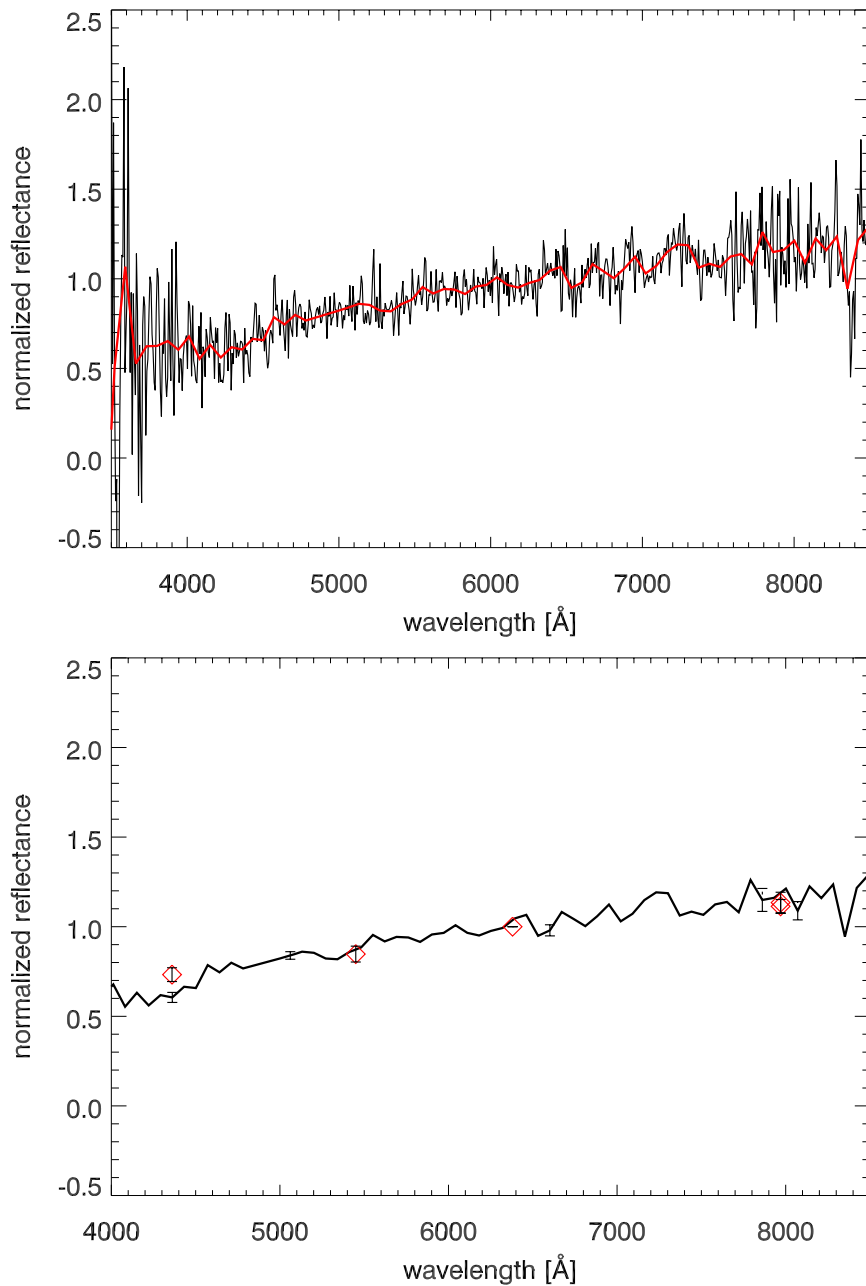


Figure 4.17: Spectrum of 67P/C-G obtained in July 2007. The spectrum is normalized to unity at 6380 Å. Upper panel: original spectrum (black line) with superimposed the binned one (red line). Lower panel: comparison between the binned spectrum and the spectral reflectivities obtained from the photometric color indices of the nucleus (diamonds). The dashed bars aside the diamonds show the uncertainties in the binned reflectance spectrum in each wavelength region, as summarized in Table 4.6.

reflectance does not vary much over rotational phase.

λ [Å]	S/N	error
4300 – 4440	36	0.03
5000 – 5140	48	0.02
6500 – 6640	32	0.03
7800 – 7940	16	0.06
8000 – 8140	20	0.05

Table 4.6: Signal-to-noise ratio (S/N) and corresponding relative error in the binned spectrum shown in Fig. 4.17. λ (Å) is the wavelength range used for the determination of S/N ratio and the error.

4.5 Tail-like structure

We tried to detect and characterize the tail-like structure associated with 67P/C-G in the visible wavelength range in all our observing epochs. Due to its low S/N ratio, this structure usually cannot be detected in a single exposure of the comet field. Thus, it is necessary to median-combine images centered in the comet. This procedure not only increases the S/N ratio of faint structures, such as the tail-like structure, but also removes stars and other objects from the background allowing an easier detection of low surface brightness features.

We could detect the tail-like structure associated with comet 67P/C-G in April 2004 (Fig. 4.18 (a)), June 2004 (Fig. 4.19) and May 2006 (Fig. 4.18 (c)). In June 2004 the tail-like structure was clearly detected in V, R and I filter images. Figure 4.19 shows the result of the median combination in I, R and V filter and the composite image, obtained as the average of the three filter exposures. In the other two epochs (April 2004 and May 2006), due to the too small number of images in V and I filter, we limited the search and characterization of the tail-like structure to R filter images. In May 2006 the field of view was very crowded with bright objects from the galactic disc. Even though the quality of the median combined image is not very good (Fig. 4.18 (c)), the tail-like structure is detectable.

In August 2006 only three exposures of the comet were performed per observing night. The median combination of the three images does not remove efficiently background objects, thus we do not consider this epoch for detection and characterization of the tail-like structure.

Figure 4.18 (b) shows the median combination of R filter images obtained in July 2007. The tail-like structure is not detected, while the linear structures present in the image are produced by stars.

At all epochs the tail-like phenomenon appears as a faint and linear structure extending from the nucleus in the direction of the heliocentric velocity vector of the comet projected in the sky. A shorter structure is visible also in the opposite direction. We determined the exact orientation of this structure measuring its position angle ($PA_{measured}$ ($^{\circ}$)) counter-clockwise North over East (Table 4.7). The anti-solar direction for the observing nights when the tail-like structure has been detected is given in Table 4.7. In June 2004 the tail-like structure is projected in sunward direction.

To determine the surface brightness of the tail-like structure, we extracted from the median combined image a rectangular window with the longer side perpendicular to the

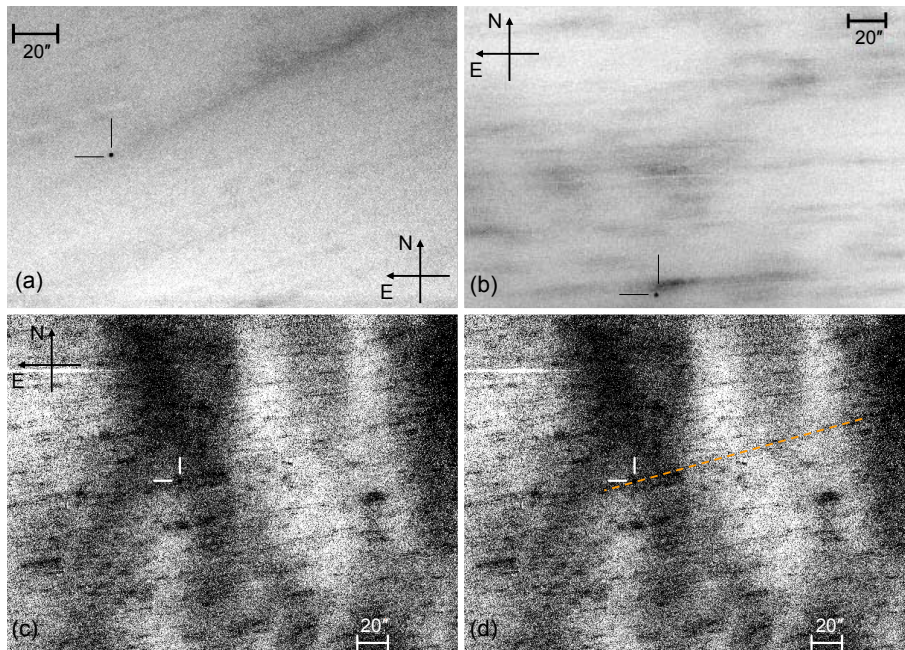


Figure 4.18: Median combination of R filter images taken in April 2004 (a), July 2007 (b) and May 2006 (c) and (d). The orientation of the image is shown and the position of the comet is marked. (a): April 2004. The tail-like structure is clearly detected and it has an extension of more than 143.7" and a width of about 25", corresponding to $\sim 3.9 \times 10^5$ km and $\sim 6.7 \times 10^4$ km at the projected comet distance, respectively. (b): July 2007. The tail-like structure is not detected. The linear structures seen in the frame close to the comet position are produced by stars. (c) and (d): May 2006. The image quality is very poor. Due to the crowdedness of the field, the median combination technique did not work well in removing background objects and their "remanences" produce artificial linear structures in the median-combined image. Moreover, interstellar clouds of the galaxy could contribute to the large-scale dark structures present in the background. However, a faint structure is detectable and to better enhance its direction an orange dashed line is superimposed to it in (d). The tail-like structure has an extension of more than 151.5" and a width of about 7.5", which correspond to $\sim 5.1 \times 10^5$ km and $\sim 2.5 \times 10^4$ km at the projected comet distance, respectively.

tail-like structure axis. The window was then collapsed along the direction parallel to the tail-like structure axis, giving rise to the cross-cut profile. The cross-cut profile had to be extracted in a region as free as possible from background object contaminations. Thus, the location of extraction was different for each epoch. In June 2004, the cross-cuts have been extracted in the same location for all three filters. Figure 4.20 displays the tail-like structure R filter cross-cut profiles from April 2004 (black line), June 2004 (red line) and May 2006 (blue line).

The April 2004 cross-cut profile was extracted at a distance of $\sim 24.25''$ ($\sim 6.5 \times 10^4$ km at the projected distance of the comet) from the nucleus of the comet. It has a mean surface brightness of (27.5 ± 0.1) mag/m² in R filter and a width of about 20". The mean surface brightness has been determined in the following way. We selected the region of the cross-cut profile which corresponds to the tail-like structure. After subtracting the background,

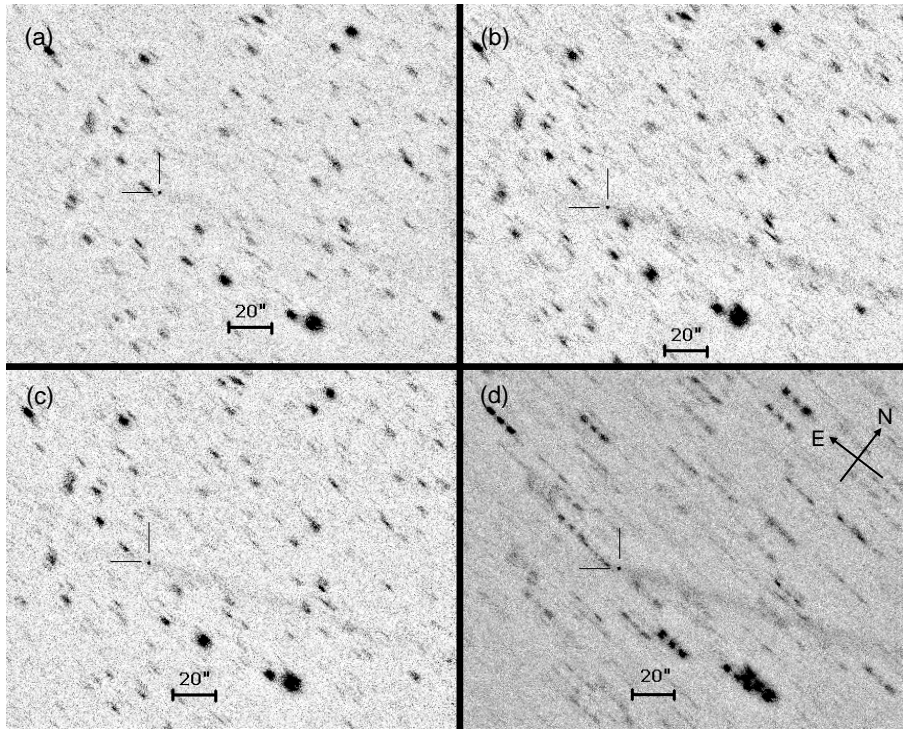


Figure 4.19: Tail-like structure of 67P/C-G in I filter (a), R filter (b), V filter (c), composite VRI image (d) as detected in June 2004. All subpanels have the same orientation, which is shown in (d). The position of the comet is marked. The tail-like structure has an extension of more than $153.25''$ and a width of about $8''$, respectively $\sim 4.8 \times 10^5$ km and $\sim 2.5 \times 10^4$ km at the projected comet distance.

date	$PA_{measured}$ [$^{\circ}$]	PA_v [$^{\circ}$]	t_{tot} [s]	filter	SB [mag/m^2]	d [10^5 km]	Υ [$^{\circ}$]
April 2004	295.7 ± 0.2	296.8	7800	R	27.5 ± 0.1	~ 0.65	272.6
June 2004	298.1 ± 0.2	297.2	3000	R	28.1 ± 0.1	~ 1.5	112.3
	298.1 ± 0.2	297.2	3000	V	29.0 ± 0.1	~ 1.5	112.3
	298.1 ± 0.2	297.2	2700	I	27.7 ± 0.1	~ 1.5	112.3
May 2006	285.6 ± 0.2	285.4	6600	R	28.5 ± 0.2	~ 3.8	11.8

Table 4.7: Summary of the details about the tail-like structure as determined from our images. $PA_{measured}$ is its position angle measured counterclockwise North over East. The filter in which the structure has been detected as well as the total integration time (t_{tot}) of the median combined images used for the detection are indicated. The mean surface brightness (SB) of the tail-like structure is reported together with the distance (in km at the projected distance of the comet) from the nucleus where the cross-cut to determine it has been extracted. PA_v is the direction of heliocentric velocity vector of the comet projected in the sky (from <http://ssd.jpl.nasa.gov/horizons.cgi>). The last column (Υ) indicates the anti-sunward direction.

we average the flux in the aforementioned region. The so determined mean flux is then converted in surface brightness, giving rise to the mean surface brightness. The profile is rather symmetrical with respect to the tail-like structure axis.

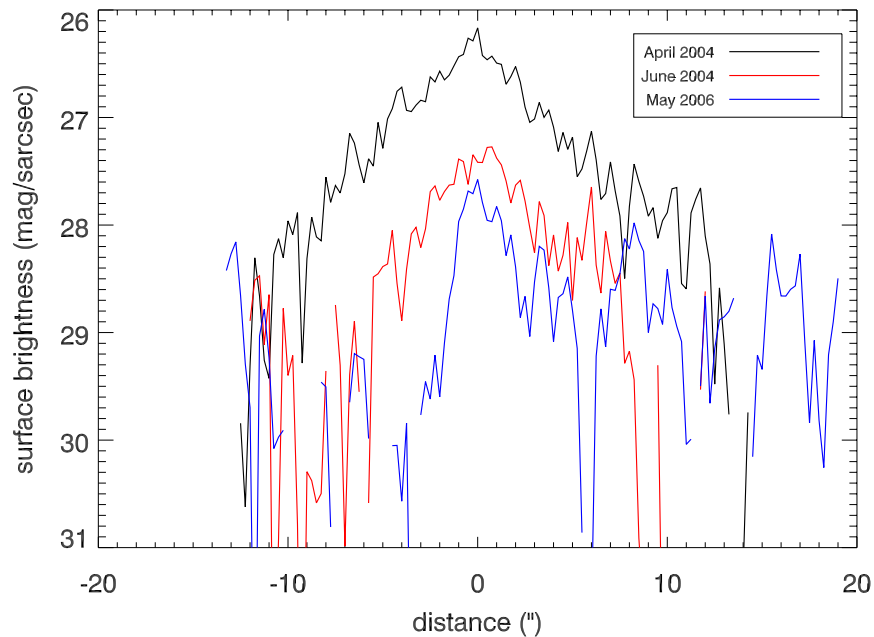


Figure 4.20: R filter cross-cut profile of the tail-like structure from April 2004 images (black line), June 2004 (red line) and May 2006 (blue line). y-axis: surface brightness in $\text{mag}/\text{sarcsec}$. x-axis: direction perpendicular to the tail-like structure in arcsec. The nucleus of the comet is located at $x = 0''$.

In June 2004 we extracted the cross-cut profiles of the tail-like structure with the same window size and at the same distance from the nucleus in all three filters. We chose a region at $\sim 47''$ ($\sim 1.5 \times 10^5$ km at the projected distance of the comet) from the nucleus which is free as much as possible from background object contaminations in all three filters. The cross-cut profiles have a width of about $8''$. The R filter profile is displayed in Fig. 4.20 (red line). We measured a mean surface brightness of the tail-like structure of $(28.1 \pm 0.1) \text{ mag}/\text{sarcsec}$ in R filter, $(29.0 \pm 0.1) \text{ mag}/\text{sarcsec}$ in V filter and $(27.7 \pm 0.1) \text{ mag}/\text{sarcsec}$ in I filter. We determined for the first time the visible colors of the tail-like structure: $V-R = 0.95 \pm 0.14 \text{ mag}/\text{sarcsec}$ and $R-I = 0.39 \pm 0.14 \text{ mag}/\text{sarcsec}$. The corresponding reflectance presents a steeper increase between 5500 \AA and 6400 \AA , while it becomes much shallower between 6400 \AA and 8000 \AA (Fig. 4.21). Over the whole wavelength range ($5500 - 8000 \text{ \AA}$) we obtained a mean spectral slope of $\sim 17 \text{ \%/1000 \AA}$. Thus, on the average, the tail-like structure looks redder than the nucleus of 67P/C-G (see Sec. 4.4).

We extracted the May 2006 cross-cut profile at a distance of $\sim 114''$ ($\sim 3.8 \times 10^5$ km at the projected distance of the comet) from the nucleus of 67P/C-G. The S/N ratio of the tail-like structure is low. Peaks relative to background objects are almost comparable with that of the tail-like structure. We determine a mean surface brightness of the tail-like structure in R filter of $(28.5 \pm 0.2) \text{ mag}/\text{sarcsec}$ and a width of about $8''$.

For an extended object of constant brightness the intensity of the reflected light per sarcsec should be proportional to $1/r^2$ in first approximation, where r is the heliocentric distance of the comet at the time of the observation. Hence, the surface brightness per sarcsec is expected to be a linear function of $\log(r)$. Figure 4.22 shows the mean R filter

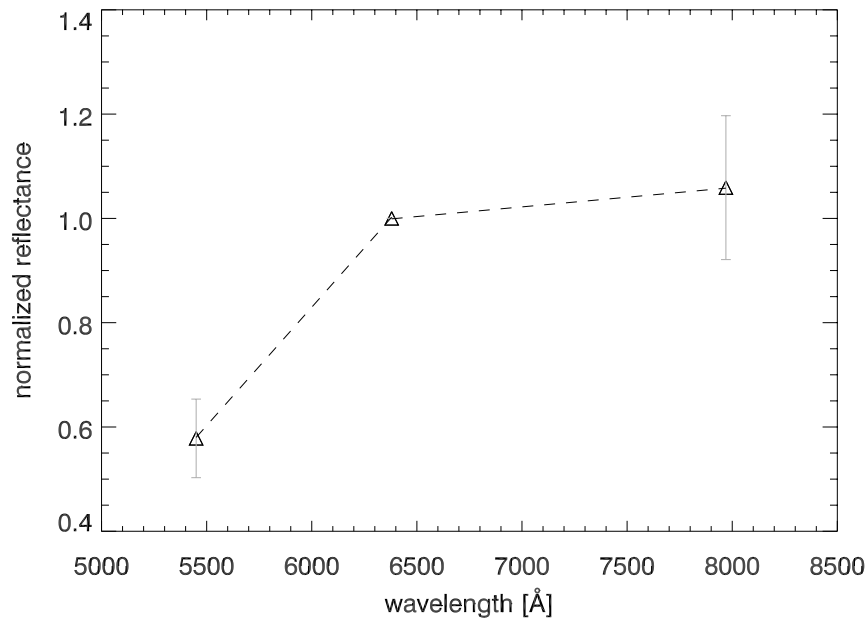


Figure 4.21: Normalized reflectance versus wavelength for the tail-like structure of 67P/C-G as measured in June 2004. It displays a steep increase between 5500 Å and 6400 Å, while it becomes much shallower between 6400 Å and 8000 Å.

surface brightness of the tail-like structure versus $\log(r)$ for April 2004, June 2004 and May 2006 observations.

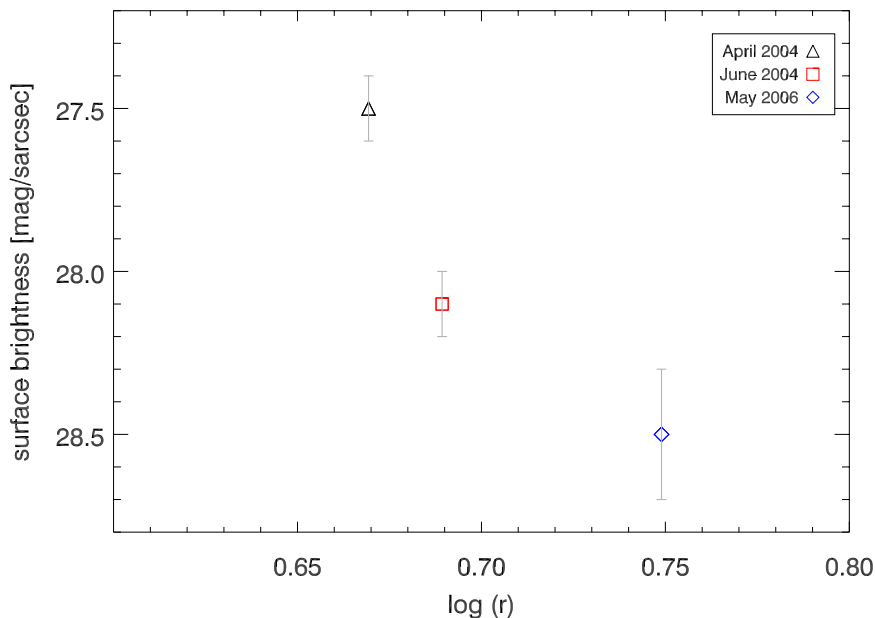


Figure 4.22: Mean R filter surface brightness of the tail-like structure versus $\log(r)$, where r is the heliocentric distance of 67P/C-G at the time of the observations.

The surface brightness of the tail-like structure, as measured in our images in April 2004, June 2004 and May 2006, is not a linear function of $\log(r)$. The decrease in the tail-

like surface brightness is very steep between April 2004 and June 2004 and it becomes shallower between June 2004 and May 2006. Based on the surface brightness of the tail-like structure in June 2004 and May 2006 we estimated that, if present and of similar surface brightness, the tail-like structure in July 2007 would have a surface brightness in R filter of $\sim 28 \text{ mag}/''^2$. Since this value is above the detection limit of the median combined image displayed in Fig. 4.18 (b), we conclude that the aforementioned structure is not present or has faded significantly from May 2006 to July 2007.

As last step in the characterization of the tail-like structure associated with comet 67P/C-G, we determined its brightness profile as function of the distance from the nucleus, for the April 2004 observation. The median combined image, where the tail-like structure is detectable, has been rotated to place the tail-like structure parallel to the x-axis. The brightness profile is displayed in Fig. 4.23.

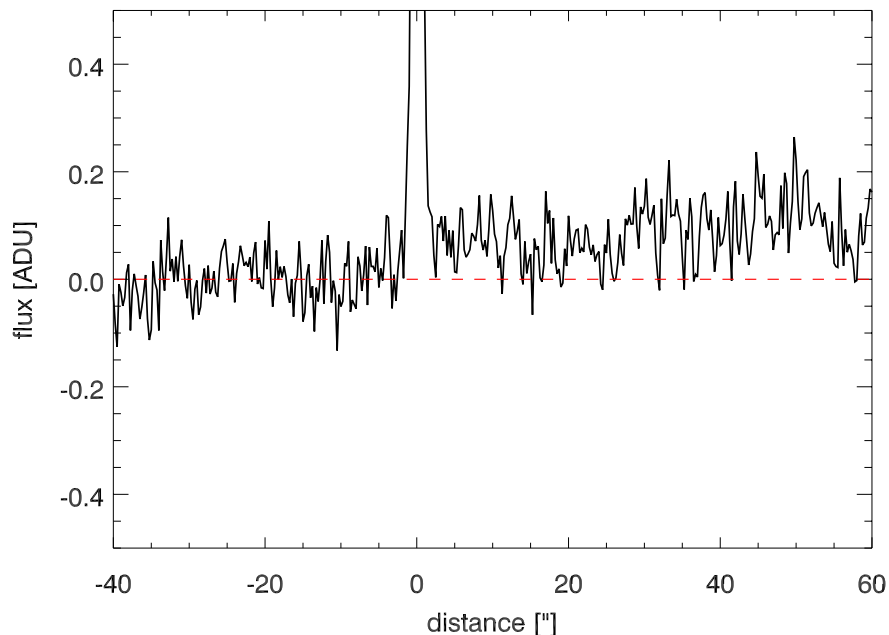


Figure 4.23: Brightness profile of the tail-like structure as function of the distance from the nucleus. The peak located at $x = 0''$ is the nucleus of the comet and the systematic shift in the profile for $x > 0''$ is due to the presence of the tail-like structure.

The peak located at $x = 0''$ is the comet nucleus. On the right-hand side of the nucleus, the brightness profile is systematically shifted with respect to the zero level (dashed red line). This shift is due to the presence of the tail-like structure. We determined that the $3\text{-}\sigma$ detection limit of the surface brightness for an extended structure of about 100 pix is $27.8 \text{ mag}/''^2$.

5 Discussion of the results

In this chapter we discuss the results obtained from our observations of 67P/C-G (described in Chapter 4) and we compare them with what is already known about this comet and about JFCs in general. In the last section we compare 67P/C-G especially with comets 1P/Halley, 9P/Tempel 1, 19P/Borrelly and 81P/Wild 2, the targets of spacecraft fly-bys in the past.

5.1 Activity at large heliocentric distance

Our observations of 67P/C-G were carried out between April 2004 and July 2007, when the comet was moving in its aphelion arc between 4.6 AU pre-aphelion and 4.6 AU post-aphelion. 67P/C-G appeared point-like at all observing epochs (see Fig. 4.5 and Fig. 4.6), indicating that no coma was present around the nucleus.

Weiler et al. (2004) compared the annual light curve of 67P/C-G relative to the 1982/83, 1995/96 and 2002/03 apparitions (Fig. 2.1). Since a similar dependence of activity from heliocentric distance is observed during the last apparitions, a possible conclusion is that no significant changes of activity of 67P/C-G took place in the last orbital passages. Moreover, images of 67P/C-G taken at the beginning of June 2008, when the comet was at heliocentric distance of ~ 3 AU, show that 67P/C-G was active (Tozzi, private communication). This is in agreement with the comet's behaviour observed in the previous orbital passages.

We, therefore, draw the following conclusions: 1) since 67P/C-G displayed the same behaviour during the last at least three orbital passages, we could expect that this behaviour will not change during the current and next orbit. Thus one can expect that 67P/C-G will not be active at large heliocentric distance, where ROSETTA will make its first approach to the comet. A first hint of a repetitive comet's behaviour in the current orbit is the detection of activity at 3 AU pre-perihelion. 2) 67P/C-G behaves as a rather typical JFC, based on the fact that it does not show activity at large heliocentric distance. Moreover, we can infer that supervolatiles like CO do not play a role for distant activity and may be either absent in the top surface layers or covered by a temporary crust or confined to regions not exposed to sunlight during aphelion.

5.2 Rotational period

The multiple solutions for the rotational period of 67P/C-G, as determined from our observations, fall in the range $T_{rot} = 12.6801 - 12.8612$ h and are in general agreement with

the one published by Lowry et al. (2006), who found 12.72 ± 0.05 h. Although a final conclusion on the accurate T_{rot} cannot be drawn from our solutions, due to insufficient sampling of the long time interval of the observation (1 year), our rotational period estimates have a much higher intrinsic accuracy. The rotational period $T_{rot} = 12.41 \pm 0.41$ h, published by Lamy et al. (2006), is consistent with our results within its error, although by more than two orders or magnitude less accurate. By applying our procedures to the HST nucleus photometry of 67P/C-G by Lamy et al. (2006), we find plausible solutions for rotational periods of 6.1 h, 12.7 h, 16.1 h, and 18.4 h. The solution $T_{rot} = 12.7 \pm 0.2$ h, which corresponds to the one they published ($T_{rot} = 12.41 \pm 0.41$ h), is now well in agreement with our results.

The bulk of the nuclei of ecliptic comets have rotational period between 5 and 18 h (Lamy et al. 2004), although the ensemble of JFCs measured may be biased towards the short period range. The possible rotational period we determined for the nucleus of 67P/C-G is in the aforementioned range. Thus, concerning the rotational period, 67P/C-G is a typical JFC.

5.3 Phase function of the nucleus

The mid-point reduced magnitude from our datasets is shown in Fig. 5.1 together with the mid-point reduced magnitude from Lowry et al. (2006) and Lamy et al. (2006). While the value from Lowry et al. (2006) is in good agreement with ours, the mid-point reduced magnitude from Lamy et al. (2006) is much lower. Most likely this discrepancy is due to changes of the observing geometry due to orbital motion of the comet. In fact, while at the time of our and Lowry et al. (2006) observations 67P/C-G was at large heliocentric distance (at true anomaly between 151° and 209°), Lamy et al. (2006) observed the comet in March 2003, a few months after its perihelion passage when 67P/C-G was at true anomaly of $\sim 106^\circ$.

With our observations we sampled the phase angle range between 0.5° and 10° . We conclude that the linear phase function approximation is the one which better represents the measurements, compared to the IAU-adopted phase function, as shown in Fig. 5.1. In fact, the measurements obtained in April 2004 and July 2007, when 67P/C-G was at phase angle of about $\sim 2^\circ$ and $\sim 6^\circ$, respectively, show that the brightness dependence on phase angle is linear in the range between 0.5° and 10° . This is an indication that 67P/C-G does not show a significant opposition effect.

We determined that the magnitude dependence on phase angle is very steep, with the linear phase coefficient in the range $\beta = 0.061 - 0.076$ mag $^\circ$.

The phase function determination requires observations at different phase angle, but with constant aspect angle. This strict requirement makes its determination a difficult task and it is not really fulfilled by the available measurements, including ours. Nowadays, the phase function has been determined for about 10 comets (Lamy et al. 2004). Usually, for JFCs a linear phase function approximation with $\beta = 0.04 \pm 0.02$ mag $^\circ$ (Lamy et al. 2004) is assumed. However, a steep phase function is measured for instance for comet 2P/Encke with $\beta = 0.06$ mag $^\circ$ (Fernandez et al. 2000) and $\beta = 0.05$ mag $^\circ$ (Bönnhardt et al. 2008). Moreover, the phase function determined for comet 9P/Tempel 1 by Belton

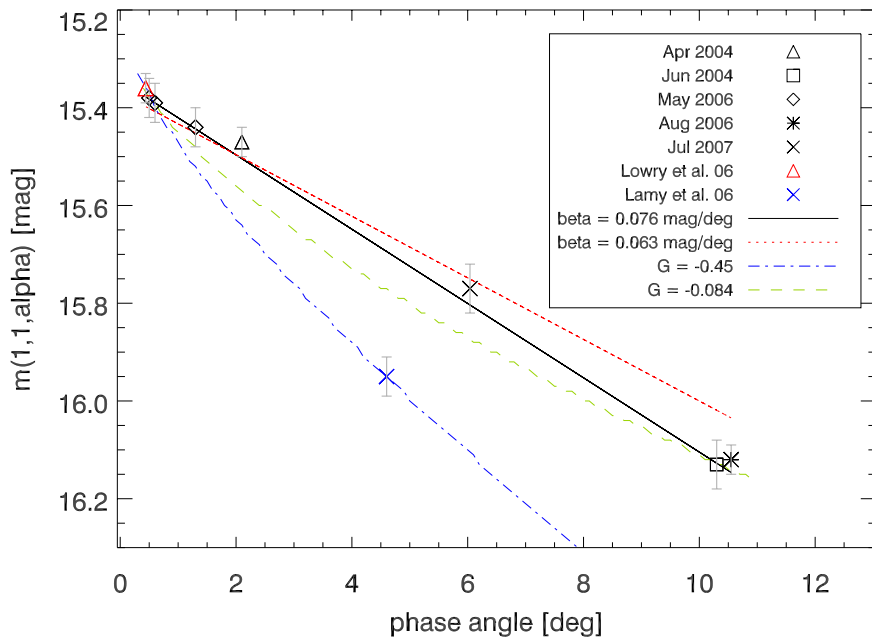


Figure 5.1: Reduced magnitude vs. phase angle. In addition to our results (displayed also in Fig. 4.14), the mid-point reduced magnitude from Lowry et al. (2006) and Lamy et al. (2006) are shown. The black solid line indicates the slope of $\beta = 0.076 \text{ mag/}^\circ$, while the red dotted one represents the slope of $\beta = 0.063 \text{ mag/}^\circ$. The blue dashed-dotted line represents the IAU-adopted phase law with $G = -0.45$, while the green dashed line the IAU-adopted phase law with $G = -0.084$.

et al. (2005), using many ground-based observations, displays a non-linear increase of brightness at small phase angles although a large scatter in the data is present.

The possible linear phase coefficient we obtain for 67P/C-G is steeper than the one usually assumed for JFCs while it is close to the one determined, for instance, for 2P/Encke, which seems to display also unusual polarimetric light scattering properties compared to other small bodies in the solar system (Bönhardt et al. 2008).

We cannot exclude that our β -factor of 67P/C-G is affected by changes in the nucleus aspect angle, although the light curve profile of the comet did not change noticeably during the aphelion arc, when the phase function of the nucleus was sampled.

A previous attempt in the determination of the phase function of 67P/C-G has been done by Lamy et al. (2007). They performed it combining HST (Lamy et al. 2006) and NTT (Lowry et al. 2006) observations, even though they stated that, due to the orbital motion of the comet, changes of observing geometry might have occurred. Assuming the IAU-adopted phase law as approximation of the phase function, they determined a slope parameter $G = -0.45$. Their result implies: 1) a very steep brightness dependence on phase angle, much steeper than the one we obtained; 2) a possible strong opposition effect. Our observations of 67P/C-G do not confirm neither of these results. We therefore believe that indeed aspect angle changes of the nucleus may be responsible for their measurements and that their phase function relation is not representing properly the light scattering behaviour of the nucleus of 67P/C-G.

The slope parameter G is indicative of the gradient of the phase curve. $G \approx 0$ indicates a shallow phase curve, while $G \approx 1$ a steep one (Bowell et al. 1989). The opposition effect is observed in asteroids and typical slope parameters are in the range $0 \leq G \leq 0.5$ (Bowell et al. 1989, Tedesco 1989). The slope parameter determined by Lamy et al. (2007) implies a very strong opposition effect, never observed even for asteroids.

In conclusion, 67P/C-G does not show opposition effect at small phase angles; it only displays a steep and linear brightness dependence on phase angle in the range between 0.5° and 10° . In this respect 67P/C-G behaves differently from the expectations which are based on the fact that for instance asteroids display opposition effect at small phase angles.

5.4 Light curve of the nucleus

The overall shape of the light curve of 67P/C-G is rather the same independently from the adopted rotational period and linear phase coefficient. 67P/C-G shows an asymmetric double peak profile. The main peak is wider and brighter than the secondary one and it presents a modulation which is not seen in the secondary peak. The minima are narrow. A comparison between our light curve and the ones obtained by Lowry et al. (2006) and Lamy et al. (2006) is shown in Fig. 5.2. All datasets are phased using the rotational period $T_{rot} = 12.7047$ h and phase angle corrected using $\beta = 0.076$ mag/ $^\circ$. Lowry et al. (2006) and Lamy et al. (2006) phase profiles are arbitrarily shift in rotational phase to match our light curve the best.

As previously mentioned, at the time of our and Lowry et al. (2006) observations the comet was in its aphelion arc. Instead, Lamy et al. (2006) observed 67P/C-G just after perihelion. The agreement between our light curve and the one obtained by Lowry et al. (2006) is very good in shape, amplitude and mean magnitude. The latter does not present the modulation in the main peak which is instead observed in our phase profile. The light curve of Lamy et al. (2006), instead, looks different both in shape and in mean magnitude. Also in this case, we iterate the conclusion that changes of observing geometry between Lamy et al. (2006) and the other observations might have taken place. Lamy et al. (2007) reconstructed a possible 3D-shape of 67P/C-G from the inversion of the HST and NTT light curves; the possible nuclear shape looks highly structured. However, only the global shape of the nucleus is constrained by the light curves and not the small scale variations which can be artifacts of the inversion. Since our light curve is very similar to the one of Lowry et al. (2006), it may also be compatible with the shape of the nucleus modelled by Lamy et al. (2007).

5.5 Size and shape of the nucleus

Table 5.1 summarizes the amplitude of the light curve of 67P/C-G, its mean absolute magnitude, effective radius and lower limit for the axis ratio as determined from our observations and from Lowry et al. (2006) and Lamy et al. (2006).

Note that both Lowry et al. (2006) and Lamy et al. (2006) assume a linear phase coefficient $\beta = 0.04$ mag/ $^\circ$ to determine the absolute magnitude of 67P/C-G used to estimate the effective radius of the comet, while we use a steeper one ($\beta = 0.076 \pm 0.003$ mag/ $^\circ$).

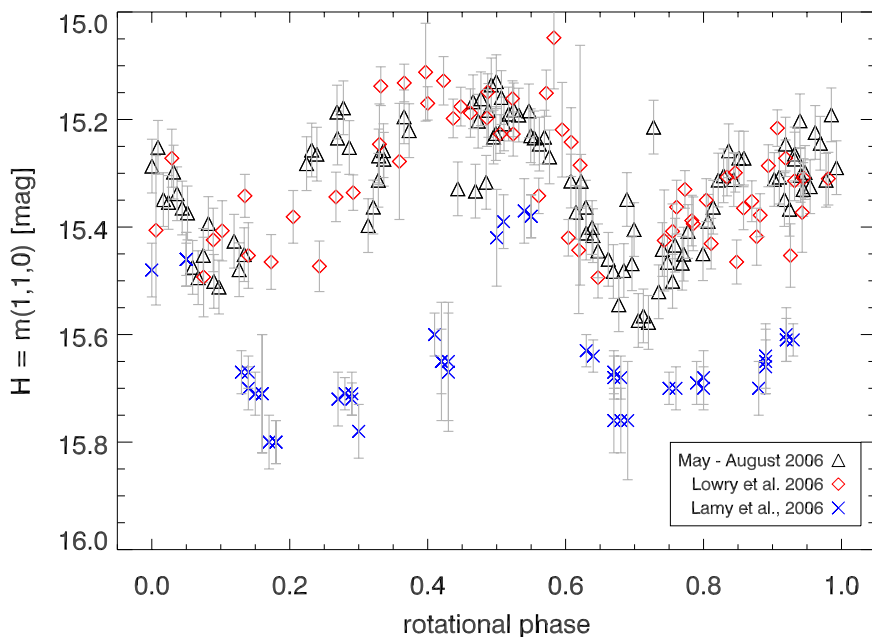


Figure 5.2: Comparison between the light curve of 67P/C-G obtained from our May 2006 + August 2006 data (black triangles) with the ones from Lowry et al. (2006) (red diamonds) and Lamy et al. (2006) (blue crosses). All datasets are phased using the rotational period $T_{rot} = 12.7047$ h and the datasets are phase angle corrected using $\beta = 0.076$ mag $^\circ$. Lowry et al. (2006) and Lamy et al. (2006) profiles are arbitrarily shifted in rotational phase to match our light curve the best.

	H_{mean} [mag]	R_{eff} [km]	Δm [mag]	a/b
our datasets	15.35 ± 0.04	2.38 ± 0.04	0.40 ± 0.07	$\geq 1.45 \pm 0.09$
Lowry et al. (2006)	15.34 ± 0.03	2.26 ± 0.03	0.38 ± 0.04	$\geq 1.42 \pm 0.05$
Lamy et al. (2006)	15.80	1.98 ± 0.02	0.44	≥ 1.5

Table 5.1: Mean absolute magnitude, effective radius, amplitude of the lightcurve and lower limit for the axis ratio for 67P/C-G as determined from our observations, from Lowry et al. (2006) and Lamy et al. (2006). Note that both Lowry et al. (2006) and Lamy et al. (2006) assume a linear phase coefficient $\beta = 0.04$ mag $^\circ$ to determine the absolute magnitude used to estimate the effective radius of the comet.

Moreover, as solar apparent R-filter magnitude we used $M_\odot = -27.14$ mag (Lang 1974), while Lamy et al. (2006) adopted $M_\odot = -27.09$ mag (Hardorp 1980) and Lowry et al. (2006) used $M_\odot = -27.26$ mag. To perform a proper comparison, we determined the mean absolute magnitude of 67P/C-G for Lamy et al. (2006) and Lowry et al. (2006) datasets using $\beta = 0.076$ mag $^\circ$. With the determined mean absolute magnitude we calculated the effective radius of the nucleus of 67P/C-G using $M_\odot = -27.14$ mag. We obtained:

1. Lowry et al. (2006) dataset: $H_{0.076} = 15.34 \pm 0.03$ mag, $R_{eff,Lowry} = 2.39 \pm 0.03$ km.
2. Lamy et al. (2006) dataset: $H_{0.076} = 15.63$ mag, $R_{eff,Lamy} = 2.09 \pm 0.02$ km.

Since the Lowry et al. (2006) dataset has been observed at very small phase angle, changes

in the linear phase coefficient do not produce changes in the absolute magnitude. The new determination of the effective radius ($R_{eff,Lowry}$) is in very good agreement with our result. The discrepancy in the effective radius between our and their published result, as shown in Table 5.1, is due to the value adopted for the solar apparent R filter magnitude. The mean absolute magnitude of Lamy et al. (2006) dataset changes when a steeper linear phase coefficient is employed. The new determined effective radius $R_{eff,Lamy}$ is still smaller than our result and it is still not in agreement with our estimation within the uncertainties. This disagreement is most likely again an effect of changes in the viewing geometry of the comet between our observations and Lamy et al. (2006) one.

All light curves show similar amplitude and thus similar lower limit for the axis ratio. Ecliptic comets have usually radius in the range 0.2 – 15 km, with a peak in the distribution for $R_{eff} < 3$ km. Regarding the axis-ratio, although there are examples of high elongated JFCs with $a/b > 2$, as i.e. comet 19P/Borrelly, most of the cometary nuclei seem to differ from a spherical body by about 50% (Lamy et al. 2004). Both effective radius and lower limit of the axis-ratio of 67P/C-G are in the range of values determined for ecliptic comets. Moreover, they are close to the mean values of both distributions, as determined by Lamy et al. (2004). Thus, also in this aspect, 67P/C-G is a rather typical JFC.

5.6 Nucleus colors and reflectance

The average color indices and the corresponding mean spectral reddening of 67P/C-G, as determined from the photometric observations we performed, are summarized in Table 4.4 and Table 5.2, where they are also additionally compared with the reddening slope determined from our spectra of 67P/C-G.

	V-R [mag]	R-I [mag]	B-R [mag]	S_P [%/1000 Å]	S_S [%/1000 Å]
April 2004	0.53 ± 0.02	0.49 ± 0.02	–	12 ± 2	–
June 2004	0.38 ± 0.04	0.44 ± 0.06	–	5 ± 3	–
May 2006	0.54 ± 0.03	0.47 ± 0.03	–	11 ± 2	$\sim 11 \pm 2$
July 2007	0.54 ± 0.05	0.46 ± 0.04	1.37 ± 0.06	$10 \pm 2^\circ, 11 \pm 2^*$	$11 \pm 1^\circ, 12 \pm 1^*$

Table 5.2: Average color indices of 67P/C-G and the corresponding mean spectral reddening (S_P) as determined from the photometric observations in April 2004, June 2004, May 2006 and July 2007. S_S is the mean reddening slope determined from the spectra of 67P/C-G observed in May 2006 and July 2007. In April 2004, June 2004 and May 2006 S_P has been determined in the wavelength range 5450 – 7970 Å. In July 2007 it has been determined in the wavelength range 5450 – 7970 Å (marked by $^\circ$) and 4360 – 7970 Å (marked by $*$). In May 2006 S_S has been determined in the wavelength range 5000 – 8500 Å, while in July 2007 in addition to the one determined in the aforementioned wavelength region (marked by $^\circ$), we determined is also in the wavelength region 4300 – 8500 Å (marked by $*$).

The average color indices show that the comet nucleus is slightly redder than the Sun, as expected for cometary nuclei (Lamy et al. 2004). Lowry et al. (2006) determined a color index V-R = 0.41 ± 0.04 mag, slightly lower than the ones we obtained. It corresponds

to a mean spectral reddening of $\sim 6\%/1000\text{ \AA}$, in the wavelength range $5500 - 6500\text{ \AA}$. Lamy et al. (2006) claim a variation of the nucleus color across the surface of the nucleus, a result which is not confirmed by our photometry and spectroscopy. Their averaged V-R color index ($0.52 \pm 0.05\text{ mag}$) is in agreement with our results, and it corresponds to a photometric reflectivity gradient of $17\%/1000\text{ \AA}$ in the wavelength range $5500 - 6500\text{ \AA}$, slightly higher than the reflectivity slope we obtained from our spectra and photometry (Table 5.2). Since reflectance spectra provide a more detailed picture of the reddening behaviour, we favour our conclusion of rather uniform surface reflectance and colors of the nucleus of comet 67P/C-G. The absence of gas emission features in the spectra is not surprising, since the comet is found without coma as described in Sec. 4.1.

The nuclear colors we determined are slightly redder than the mean colors determined for ecliptic comets: $\langle V-R \rangle = 0.42\text{ mag}$, $\langle R-I \rangle = 0.38\text{ mag}$ (Lamy et al. 2004). The absence of absorption or emission features in our spectra and a rather constant spectral slope is in agreement with the results of Luu (1993), who obtained visible spectra of inactive comets. We iterate the conclusion that 67P/C-G is a rather typical Jupiter family comet concerning its spectral behaviour in the visible wavelength range.

5.7 Tail-like structure

We detected a tail-like structure in our images in April 2004, June 2004 and May 2006. The aforementioned structure was not present in July 2007. We did not consider the August 2006 images for the detection of the tail-like structure due to the too small number of frames available.

We tried to interpret the tail-like structure in terms of “old” dust trail or neck-line based on 1) geometric considerations (\equiv position angle) and 2) surface brightness variations with heliocentric distance.

The “old” trail is composed of large dust particles emitted during the previous orbits of 67P/C-G, i.e. 1995/96 and earlier, while the neck-line is made of large dust particles emitted during the last orbit (2002/03 apparition).

1. Geometric considerations

We compare the position angle of the tail-like structure as measured in our images ($PA_{measured}$) with:

1. The expected position angle of the “old” dust trail, as indicated by the direction of the heliocentric velocity vector projected in the sky (PA_v).
2. The expected position angle of the neck-line, as predicted by dust tail simulations by J. Agarwal ($PA_{NL,A}$) and by M. Fulle ($PA_{NL,F}$) for the dates of our observations (private communications).

All the aforementioned position angles are measured counterclockwise North over East and they are summarized in Table 5.3.

The main difference between the model of J. Agarwal (Agarwal 2007) and the one of M. Fulle (Fulle et al. 2004) is that the former one allows comet activity only around perihelion (from 300 days before to 300 days after perihelion), while the latter one does not

date	$PA_{measured} [^\circ]$	$PA_v [^\circ]$	$PA_{NL,A} [^\circ]$	$PA_{NL,F} [^\circ]$
April 2004	295.7 ± 0.2	296.8	295.9 ± 0.2	296.1
June 2004	298.1 ± 0.2	297.2	298.4 ± 0.2	298.7
May 2006	285.6 ± 0.2	285.4	285.7 ± 0.2	285.5
August 2006	–	288.9	289.6 ± 0.4	
July 2007	–	279.1	279.8 ± 0.3	279.2

Table 5.3: Geometry of the tail-like structure in 67P/C-G. $PA_{measured}$: position angle of the tail-like structure as measured in our image. PA_v : direction of the heliocentric velocity vector projected in the sky, which indicates the orientation of the “old” dust trail. $PA_{NL,A}$ and $PA_{NL,F}$: position angle of the neck-line as predicted by Agarwal (private communication) and Fulle (private communication), respectively. For the August 2006 run, we chose one of the nights (August 18) as representative of the observing run.

restrict the activity to a certain heliocentric range, but allows 67P/C-G to be active also at larger heliocentric distance.

The measured position angle of the tail-like structure is in better agreement with the ones predicted by J. Agarwal and M. Fulle rather than with the direction of heliocentric velocity vector projected in the sky. Thus, based on geometrical considerations, we conclude that the tail-like structure is more compatible with a neck-line activity of the comet during the recent perihelion passage rather with an “old” dust trail.

2. Surface brightness versus heliocentric distance

For an extended object of constant brightness the intensity of the reflected light per sarcsec should be proportional to $1/r^2$, where r is the heliocentric distance of the comet at the time of the observation. Hence, the surface brightness per sarcsec is expected to be a linear function of $\log(r)$. The measured surface brightness is independent of the geocentric distance Δ , because the amount of particles per unit solid angle is proportional to Δ^2 , while the radiation received from a single particle is proportional to Δ^{-2} . The surface brightness of the “old” dust trail should be a linear function of $\log(r)$, since the “old” dust trail is a more constant phenomenon over time. This assumes that the “old” dust trail is indeed not subject to major secular brightness variations due to for instance highly variable dust production profiles over the lifetime of the comet or major changes in the size distribution of the grains. The neck-line, instead, depends on activity within true anomaly of about 180° before the observation, thus its surface brightness can vary strongly and in shorter time scales, as consequence of activity variations along the respective orbit arc.

The surface brightness of the tail-like structure, as measured in our images in April 2004, June 2004 and May 2006, is not a linear function of $\log(r)$ (Fig. 4.22). The decrease in the tail-like structure surface brightness is very steep between April 2004 and June 2004 and it becomes shallower between June 2004 and May 2006. This strengthens our conclusion that the tail-like structure is better compatible with a neck-line phenomenon rather than with a “old” dust trail.

As a follow-up to this conclusion, we determined the true anomaly within which the large dust grains which compose the neck-line were emitted (true anomaly of 180° before the observation). The true anomalies are summarized in Table 5.4. All observing epochs correspond to earliest emission dates around perihelion, between ~ 1.4 AU pre-perihelion

and ~ 1.4 AU post-perihelion.

	Ω_{obs} [$^{\circ}$]	$\Omega_{emission}$ [$^{\circ}$]	$\Delta\Omega$ [$^{\circ}$]
April 2004	151	331	-29
June 2004	155	335	-25
May 2006	187	7	+7
August 2006	191	11	+11
July 2007	209	29	+29

Table 5.4: True anomaly relative to each observing epoch (Ω_{obs}) and the one corresponding to 180° before the observation ($\Omega_{emission}$). $\Delta\Omega$ is the difference between $\Omega_{emission}$ and perihelion. Negative values indicate starting emission pre-perihelion, while positive values starting emission post-perihelion.

How can we explain the changes that we measured in the neck-line surface brightness (Fig. 4.22) and the non-detection of the neck-line in July 2007?

A possible explanation is that the dust production and size distribution of the dust particles of 67P/C-G are rather symmetrical and that the total amount of dust in the vicinity of the comet has changed due to the action of the radiation pressure on the dust grains. In fact, the neck-line observed in April 2004 is formed by dust grains emitted from approximately the beginning of July 2002, thus almost 2 years before the observation. The dust grains which would give rise to a neck-line observable in July 2007 would have had to be emitted at about 1.4 AU post-perihelion or later, i.e. from approximately the beginning of October 2002. Therefore, the time between the beginning of their emission and their possible observation is slightly less than 5 years. In the latter case the time passed between the emission start and the observation is 3 years longer than in the former one. The drift of the dust grains from the vicinity of the comet by radiation pressure in the aforementioned three years can be significant and it can be a plausible explanation for the non-detection of the neck-line in July 2007 and also for the fading of the surface brightness between April 2004 and May 2006. However, this scenario has difficulties to explain the decrease of the neck-line surface brightness between April 2004 and June 2004, since they cover essentially the same period of dust emission.

Another possible explanation could be very rapid changes in the dust production and/or in the size distribution of the dust particles of 67P/C-G. However, these changes have to take place within a few days to explain the steep fading of the neck-line between April 2004 and June 2004. Moreover, these scenarios require that the dust production and/or size distribution display a strong asymmetry pre-to-post perihelion to explain the non-detection of the neck-line in July 2007.

In conclusion, we could not find a satisfactory - and simple - explanation for rapid changes in the neck-line surface brightness measured and the non-detection of the structure in July 2007. Refinements of numerical models are needed to find the best explanation of the observations.

On April 19-21 2004, observations of 67P/C-G in visible wavelength were performed by Agarwal (2007) with the Wide Field Imager (WFI) at the ESO-MPG 2.2m telescope on La Silla (Chile). The tail-like structure was clearly detected (Fig. 2.4). Since the

aforementioned observations were performed very close in time with our April 2004 run, we compared the cross-cut profile of the tail-like structure we obtained from our images with the one from Agarwal (2007). The comparison is shown in Fig. 5.3, where the black solid line corresponds to our cross-cut profile in R filter (displayed in Fig. 4.20), while the other four curves correspond to cross-cuts profiles obtained by Agarwal (2007) at about 25" and 47" from the nucleus and using two windows (of 9" and 36") to extract the cross-cut profile.

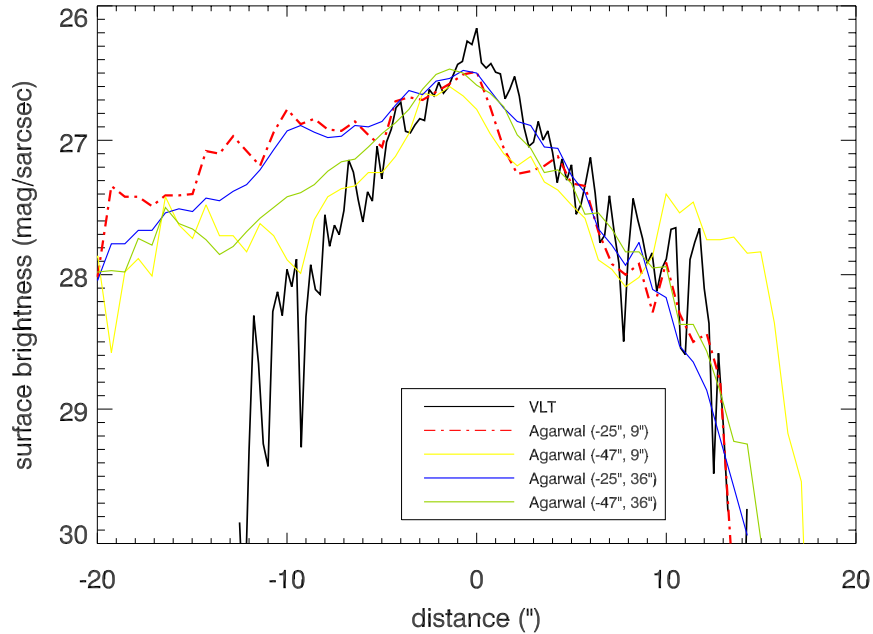


Figure 5.3: Comparison of a cross-cut profile of the tail-like structure obtained from our observations in April 2004 (black solid curve) and by Agarwal (2007). The four cross-cuts profiles from Agarwal (2007) have been extracted at 25" and 47" from the nucleus and employing a 9" and 36" window for the extraction. The profile which was extracted in the same location as our and with the same window is shown by the red dash dotted line (distance 25", window 9").

The profile which was extracted in the same location as our and with the same window is shown by the red dash dotted line (distance 25", window 9"). There is a good agreement between our cross-cut profile and the one from Agarwal (2007), in particular on the right-hand side of the image. Moreover, the cross-cut profile by Agarwal (2007) confirms the excess of brightness measured from our images in April 2004.

5.8 Dust and gas production

We complement our study of 67P/C-G, which focused on the comet behaviour at large heliocentric distance from the Sun, by a brief analysis of its near-perihelion activity using published results.

Production rates of different species (gas and dust) in comet 67P/C-G were determined by several authors (i.e. Hanner et al. 1985, A'Hearn et al. 1995, Osip et al. 1992, Schleicher

2006, Schulz et al. 2004, Weiler et al. 2004) for the 1982/83, 1995/96 and 2002/03 apparitions. A general conclusion is that all species present a perihelion asymmetry in the production rates, with a peak about one month after perihelion (see i.e. Fig. 2.2). This asymmetry might be typical for Jupiter family comets (A’Hearn et al. 1995). Observations obtained during the comet’s apparition in 1982/83 showed that the coma of 67P/C-G was depleted in C_2 with respect to CN ($C_2/CN \approx 0.49$) at a heliocentric distance of 1.4 AU (A’Hearn et al. 1995). The same depletion was also measured by Schulz et al. (2004) during the 2002/03 apparition at 2.9 AU post-perihelion ($C_2/CN < 0.62$). A depletion of the carbon-chain species C_2 and C_3 has been observed in many comets, most of them members of the Jupiter family (A’Hearn et al. 1995). Based on water production rate of 67P/C-G at 1.41 AU, A’Hearn et al. (1995) estimated an active area on the nucleus of 1.3 km^2 , yielding an active fraction of 2.6%. In a similar way, Schleicher (2006) measured a peak water production of $\sim 8 \times 10^{27} \text{ mol/s}$ at $\sim 1.35 \text{ AU}$ post-perihelion and determined an active area on the nuclear surface of $1.5 - 2.2 \text{ km}^2$. Assuming that the radius of the nucleus of 67P/C-G is $1.98 \pm 0.02 \text{ km}$ (Lamy et al. 2006) the effective active area corresponds to an active fraction of about 3 – 4%. Since according to our results, the effective radius of 67P/C-G is larger than the one determined by Lamy et al. (2006), the fraction of the nucleus which is active is smaller than the one determined by Schleicher (2006). The general conclusion is that a small fraction of the nuclear surface is active, as expected for JFCs (A’Hearn et al. 1995). Gas and dust production rates of 67P/C-G show similar behaviour during the last three apparitions, indicating that the comet’s activity did not change significantly during the last orbital passages (Schleicher 2006, Weiler et al. 2004). This behaviour was also observed for most short-period comets studied by A’Hearn et al. (1995). A dust production rate of $Af\rho \sim 450 \text{ cm}$ at 1.35 AU post-perihelion was determined by Schleicher (2006). At similar heliocentric distance Weiler et al. (2004) determined $Af\rho = 428.2 \pm 59.8 \text{ cm}$. Lamy et al. (2006), with observations of 67P/C-G performed at 2.5 AU post-perihelion in the 2002/03 apparition, determined $Af\rho = 40.2 \pm 0.3 \text{ cm}$. The coma of 67P/C-G looks red with a reddening slope of $32 \pm 6 \text{ \%}/1000 \text{ \AA}$ (Lamy et al. 2006), of $24 \pm 1 \text{ \%}/1000 \text{ \AA}$ (Storrs et al. 1992) and $30 \pm 42 \text{ \%}/1000 \text{ \AA}$ (Schleicher 2006) (although the latter reddening slope, due to the very large error bar, is not a very constraining result). Weiler et al. (2004), instead, obtained $-0.7 \pm 5.1 \text{ \%}/1000 \text{ \AA}$, which would imply a gray color of the coma dust of 67P/C-G. According to the reddening slopes determined by Lamy et al. (2006) and Storrs et al. (1992), the coma of 67P/C-G looks much redder than the nucleus of the comet, for which we determined a reddening slope slightly higher than $10 \text{ \%}/1000 \text{ \AA}$ based on photometry and spectroscopy (Table 5.2).

5.9 Comparisons with other “spaceflight” comets

Thanks to the observations we performed when 67P/C-G was at large heliocentric distance, a good characterization of the nucleus of the ROSETTA target comet and its dust environment far away from the Sun has been drawn. Based on the results summarized in Chapter 4 and discussed in the previous sections, 67P/C-G looks a rather typical Jupiter family comet.

We can compare the characteristics of 67P/C-G with those of well-studied cometary nu-

clei, i.e. 1P/Halley, 19P/Borrelly, 9P/Tempel 1 and 81P/Wild 2, fly-by targets of space missions. While 1P/Halley is a long-period comet, the other three are classified as Jupiter family comets.

Resolved images display irregular shaped and topologically diverse cometary nuclei (Fig 1.6). While comet 1P/Halley, 19P/Borrelly and 9P/Tempel 1 are well described by a prolate ellipsoid, the nucleus of comet 81P/Wild 2 is more rounded and has an oblate shape. Based on the lower limit for the axis ratio we determined from our light curve, the nucleus of 67P/C-G could be comparable to the one of 9P/Tempel 1, which display a ratio between the longest and the shortest dimension of ~ 1.55 . 1P/Halley and 19P/Borrelly nuclei are more elongated, with an axis ratio of 2.1 and 2.5, respectively. Moreover, the two aforementioned cometary nuclei have a larger size than comet 67P/C-G (Keller et al. 2004). The effective diameter of comet 1P/Halley is 9.8 ± 0.9 km (Ferrin 2005). A'Hearn et al. (2005) determined a mean radius of comet 9P/Tempel 1 of 3.0 ± 0.1 km, of the same order of magnitude of the nuclear radius of 67P/C-G. The nucleus of comet 81P/Wild 2 is best approximated by a tri-axial ellipsoid with radii of $1.65 \times 2.00 \times 2.75 \pm 0.05$ km (Brownlee et al. 2005). Thus, the effective diameter is 3.93 ± 0.10 km (Ferrin 2005), slightly smaller than the value we determined for the nucleus of 67P/C-G.

Ferrin (2005) and Ferrin (2007) present, among others, the annual light curves of comet 1P/Halley, 19P/Borrelly, 9P/Tempel 1, 81P/Wild 2 and 67P/C-G. For each comet they determined at which heliocentric distance before perihelion the activity starts and when after perihelion the comet becomes inactive. The turn-on distance of comet 1P/Halley is 6.15 ± 0.19 AU and its turn-off distance is 12.56 ± 0.02 AU. However, West et al. (1991) detected an outburst when 1P/Halley was at heliocentric distance of 14.31 AU. The activity of 19P/Borrelly started at 2.9 ± 0.1 AU pre-perihelion and the comet was still active at $r > 5$ AU post-perihelion. Comet 9P/Tempel 1 was detected active between 3.47 ± 0.05 AU pre-perihelion and 4.20 ± 0.05 AU post-perihelion. Observations of comet 81P/Wild 2 show that its activity starts at 4.4 ± 0.1 AU pre-perihelion and the turn-off point is 5.8 ± 0.8 AU (Ferrin 2005). It has to be noticed that, since the aphelion distance of 81P/Wild 2 is 5.3 AU, the aforementioned statement can be interpreted as the comet is always active, even at aphelion. Moreover, Pittichova and Meech (2001) found the comet is indeed active at heliocentric distance of 4.9 AU post-perihelion, which supports the hypothesis of activity in the aphelion arc. Finally, the turn-on point for comet 67P/C-G should be at 2.8 ± 0.1 AU pre-perihelion and the off-set of the activity might be around 4.0 ± 0.1 AU post-perihelion. Images of 67P/C-G, obtained at the beginning of June 2008 when the comet was at heliocentric distance of ~ 3 AU, show that the comet was active (Tozzi, private communication).

Comets 1P/Halley, 19P/Borrelly and 81P/Wild 2 are found active at large heliocentric distances. Thus, most likely this activity is driven by ices which sublimate at lower temperature with respect to water ice (i.e. CO, CO₂). Thanks to our observations, we can exclude that 67P/C-G shows significant activity in the aphelion arc. Also concerning activity, 67P/C-G looks similar to comet 9P/Tempel 1, which does not show activity at large heliocentric distance.

Osip et al. (1992) compared the $Af\rho$ of 67P/C-G with the one of comet 1P/Halley, obtaining that the one of 67P/C-G is about a factor of 40 below that of 1P/Halley. Resolved images of comets 1P/Halley, 19P/Borrelly, 81P/Wild 2 and 9P/Tempel 1 show that the activity is concentrated in localized regions of the nuclear surface. The water production

rate measured by different authors (i.e. A’Hearn et al. 1995, Schleicher 2006) implies that only a small fraction (few percents) of the nuclear surface of 67P/C-G is active. Even though more precise information will come only thanks to resolved images of the nucleus of 67P/C-G by cameras onboard the ROSETTA spacecraft, the aforementioned result indicates similarities between the nucleus of 67P/C-G and the ones of the other well-studied comets. Moreover, resolved images of the nucleus of 67P/C-G will allow to determine the exact shape of this cometary nucleus and compare the nuclear surface of 67P/C-G with the one of the other well-studied comets.

A common characteristic of 1P/Halley, 19P/Borrelly, 9P/Tempel 1 and 81P/Wild 2 nuclei is that their albedo is very low, locating cometary nuclei among the darkest objects in the Solar System. Combining visible and IR observations of 67P/C-G Lamy et al. (2004b) determined an albedo of 0.044 (in R filter). This value is close to the albedo measured for comet 1P/Halley and in agreement with the value usually assumed for comets.

6 Conclusions

The results we present in this thesis help to complete the portrait of the nucleus of 67P/C-G and its dust environment at large heliocentric distance. Based on its rotational period, size and shape, nuclear colors and visible reflectance spectra, activity at large heliocentric distance, 67P/C-G is a rather typical Jupiter family comet. The determination of its phase function emphasizes that the behaviour of some cometary nuclei at small phase angle might be different from that of asteroids, which display opposition effect. Moreover, it also underlines that the linear phase coefficient $\beta = 0.04 \text{ mag/}^\circ$, usually assumed for JFCs, might not be always a good representative for the dependence of brightness versus phase angle. For instance, already in two cases (67P/C-G and 2P/Encke) a steeper linear phase coefficient has been determined. In conclusion, this could indicate that comets display different light scattering properties compared to other small bodies in the solar system (i.e. asteroids).

No observations of 67P/C-G from previous aphelion passages are available which can be compared with our results to evaluate whether changes in the comet's behaviour at large heliocentric distance took place during the last apparitions. Since the activity of 67P/C-G in the perihelion arc did not change significantly during the last orbital passages (Schleicher 2006, Weiler et al. 2004), this might suggest that also the comet's behaviour at large heliocentric distance did not change from one orbital revolution to the other. Thus, we could expect that during its approach to 67P/C-G, ROSETTA will find the same conditions we detected during our observations.

In the current orbit, 67P/C-G was not active in the aphelion arc, between 4.6 AU pre-aphelion and 4.6 AU post-aphelion. The latter one is the location at which the first approach of the ROSETTA spacecraft to 67P/C-G will take place. Thus, the knowledge that we acquired about the dust environment of 67P/C-G at large heliocentric distance is relevant for a good planning of the ROSETTA spacecraft rendezvous with the comet.

A FORS2 filters and grism used in the observing runs

Photometric observations with FORS2 at the ESO VLT Observatory have been performed using Bessell B, V, R and I filters. Their transmission curves are plot in Figure A.1, while the central wavelength and the Full Width Half Maximum (FWHM) of each filter is summarized in Table A.1.

Filter	$\lambda_{central}$ [Å]	FWHM [Å]
B	4290	880
V	5540	1115
R special	6550	1650
I	7680	1380

Table A.1: Central wavelengths ($\lambda_{central}$) and Full Width Half Maximum (FWHM) of the Bessell filter used for imaging of 67P/C-G.

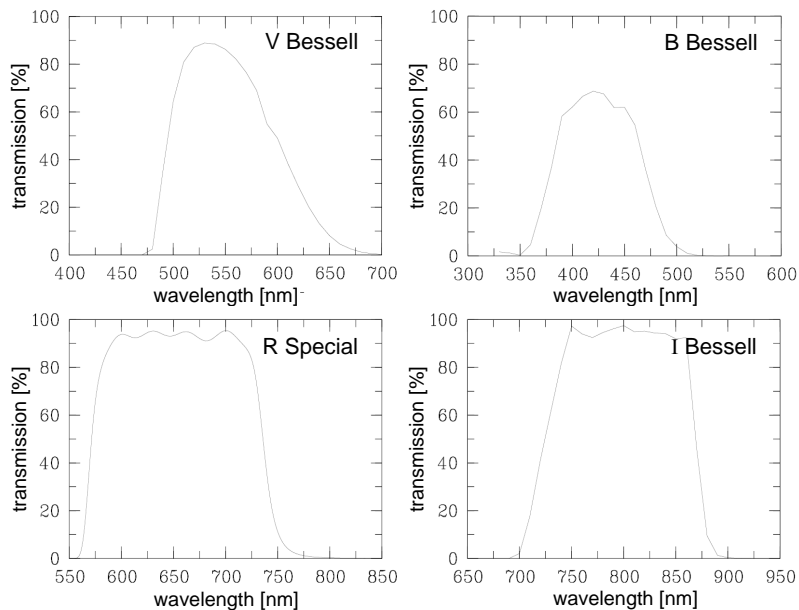


Figure A.1: Transmission curves of the Bessell filters used for the photometric observations of 67P/C-G. Figure adapted from FORS2 manual: http://www.eso.org/sci/facilities/paranal/instruments/fors/doc/VLT-MAN-ESO-13100-1543_v82.pdf.

Note that the transmission curve of the R special filter is more edge-shape compared to the normal Bessell R filter in order to exclude regions of bright sky lines.

Spectra of the 67P/C-G were obtained with the low resolution grism 150I+27. Its wavelength range is $\Delta\lambda = 3500 - 11000 \text{ \AA}$ and it has a dispersion of 3.45 \AA/pix . Its central wavelength is $\lambda_{central} = 7200 \text{ \AA}$ and the grism resolution for a 1" slit at $\lambda_{central}$ is $\lambda/\Delta\lambda = 260$. The efficiency curve of the grism 150I+27 is plotted in Figure A.2.

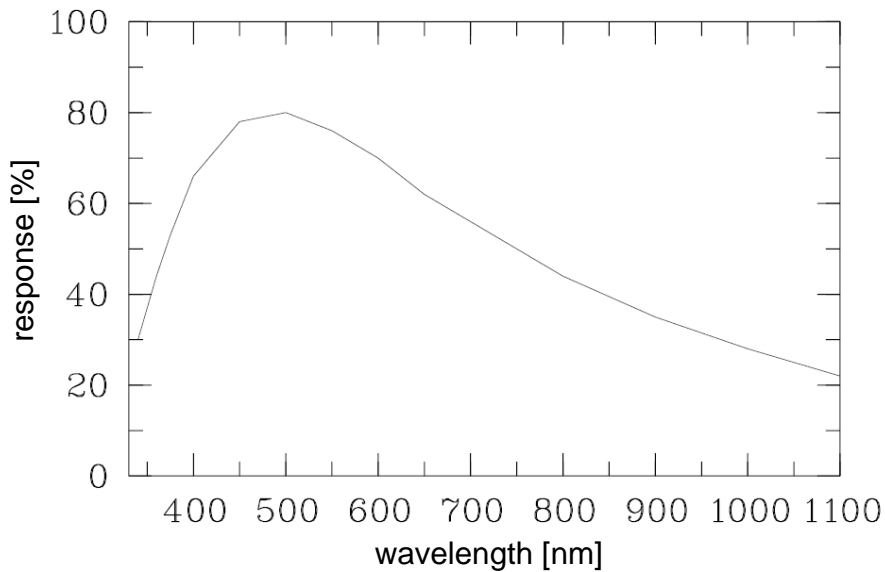


Figure A.2: Efficiency curve of the low resolution grism 150I+27. Figure adapted from FORS2 manual: http://www.eso.org/sci/facilities/paranal/instruments/fors/doc/VLT-MAN-ESO-13100-1543_v82.pdf.

B Flux calibration of photometric images

B.1 Aperture photometry

Aperture photometry is a simple approach to determine the measured magnitude of a point source, i.e. a star or a not-active comet. For our application using the MIDAS software package, three concentric circles are employed (Fig. B.1). The inner circle is used to measure the relative flux (or magnitude) of the object, while the external annulus is used to determine the sky background. The middle annulus is not employed in the measurement itself, but allows to change the location for the background determination.

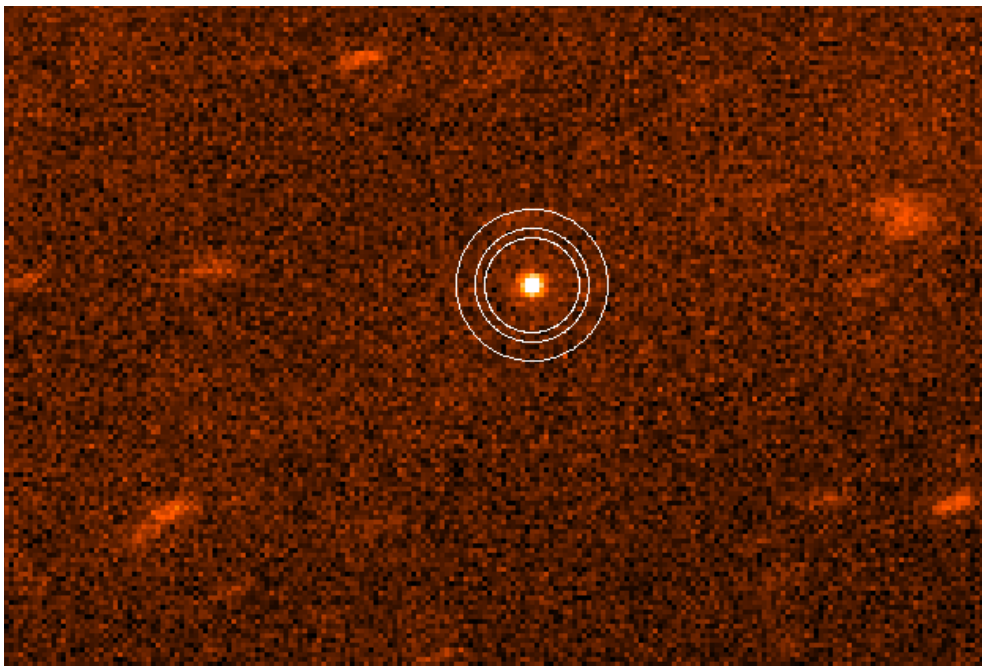


Figure B.1: Example of aperture photometry.

The inner circle has to be large enough to contain all the object flux, but at the same time small enough to avoid high background, which increases the noise compared to the object signal, i.e. decreasing the S/N ratio. This second requirement is of high importance in case of photometric measurements of faint objects. A good criterion is to choose a inner

circle diameter of $\geq 3 \times \text{FWHM}$ of the object. The sky background has to be determined in a region free from background object contaminations. Varying the amplitude of the middle annulus, the best location for the sky background determination can be selected. Since sky background variations can take place across the CCD, the closer to the object the sky background measurement is performed, the better it is.

A good rule is to use the same aperture (i.e. diameter of the inner circle) during the measurement of the object magnitude in images belonging to the same dataset. Unfortunately this is not always possible. For instance, when the seeing increases, the point spread function of the object is modified: its FWHM increases. Thus, to avoid to underestimate the object flux a larger aperture has to be employed.

B.2 Atmospheric extinction

Earth's atmosphere is not completely transparent. Dust particles, droplets of water and molecules scatter and absorb light as it passes through the air; the longer the path in the atmosphere, the greater this effect is. Absorption and scattering are wavelength dependent: the shorter wavelengths are affected more than the longer ones. Thus, the longer the path that the object light has to make in the Earth's atmosphere is, the dimmer and redder the object gets. This effect is called atmospheric extinction. Correcting for atmospheric extinction results in the object's magnitude and color as they would appear to an observer above the Earth's atmosphere.

The effect of extinction depends upon the altitude of the object above the horizon. The minimum path length is for an object in zenith; this thickness of the atmosphere is called, by definition, one air mass (AM). The air mass increases as the zenith angle (angle between the zenith, the observer and the object) increases (see Fig. B.2).

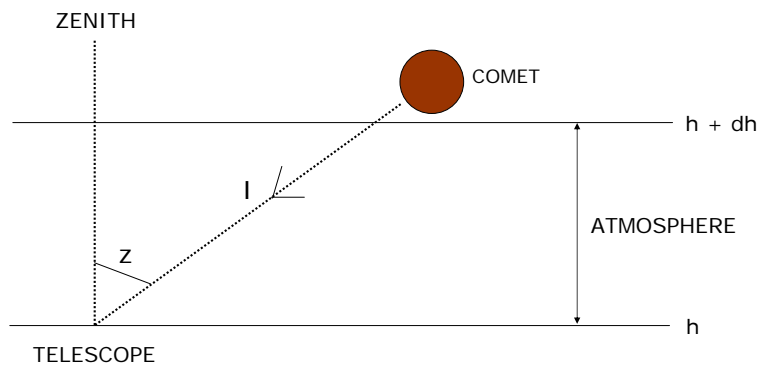


Figure B.2: I is the incoming light beam and z the zenith angle.

The expression to calculate the air mass is:

$$AM = \frac{\int_{h_0}^{h_1} \rho(h) \sec[z(h)] dh}{\int_{h_0}^{h_1} \rho(h) dh} \quad (\text{B.1})$$

where z is the zenith angle and $\rho(h)$ is the specific mass of air. Assuming an homogeneous

(no refraction), plane-parallel (Earth's curvature neglected) atmosphere, the air mass can be approximated as:

$$AM = \sec(z), \quad (\text{B.2})$$

where z is the zenith angle. Let's consider observations of a star as it approaches and passes through the zenith. Plotting the measured magnitude against the air mass, it is immediate to see that the measured magnitude decreases approximately linearly as the air mass increases (for $AM \leq 2.5$). The slope of the curve is the *extinction coefficient*. The measured magnitude (m_{meas}) of a star can now be corrected (in the first order) for extinction:

$$m_0 = m_{meas} - k \cdot AM, \quad (\text{B.3})$$

where m_0 is the magnitude that the star would have if it would be seen from above the Earth's atmosphere and k is the extinction coefficient (Bouguer's law).

Before we mentioned that extinction depends upon the wavelength and it is usually higher for blue light than for red one. Thus, making observations through different filters, we obtain different extinction coefficients.

When we perform an observation, we have to deal with three aspects: the spectral sensitivity (or response) of the detector in use, the transmission curve of the optical system which is usually determined by the filter transmission curve and the spectral energy distribution of the observed object. All of them are wavelength dependent, as shown in Fig. B.3.

The combined spectral sensitivity of the detector and the transmission curve of the filter (optical system) defines a wavelength range that in turn sets the color system which can be used for the observations.

The combination of the transmission curve of a filter with the spectral energy distribution of an object determines the distribution of energy in the transmitted beam. Thus the transmissivity of a filter depends upon the color of the incident light.

The color index is defined as the difference between magnitudes determined at two specific wavelengths (for example blue and red). Therefore, the true color index (outside the atmosphere) is given by:

$$C_0 = B_0 - R_0 = (B - k_B \cdot AM) - (R - k_R \cdot AM) = C - k_C \cdot AM, \quad (\text{B.4})$$

where $k_C = k_B - k_R$ is the *color coefficient* of the instrumentation used and $C = B - R$ is the measured color index.

Since the extinction coefficient of a blue star is different from the one of a red star, the color coefficient for a blue star is different from the color coefficient for a red star. A way to take into account of this effect is to introduce a second-order extinction correction. This correction is quite small in the visible and longer wavelengths and it can often be ignored, as we do for our observations.

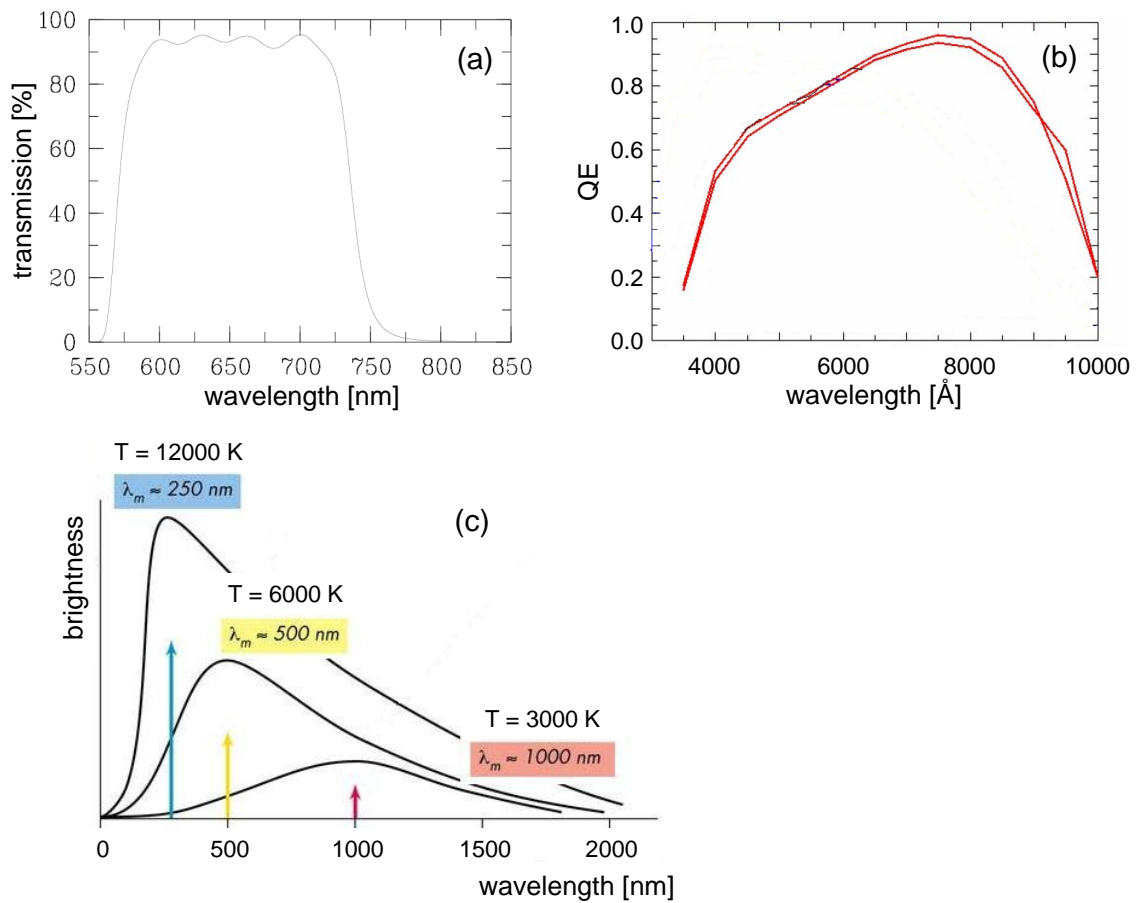


Figure B.3: (a): transmission curve of R special filter with transmissivity on the y-axis and wavelength (in nm) on the x-axis. Figure from FORS2 user manual. (b): quantum efficiency of the detector. Figure adapted from FORS2 spectral sensitivity image from FORS2 user manual. (c): blackbody radiation for different temperatures.

B.3 Color transformation

When observations of one object are performed, measurements depend upon the telescope, filter, detector and altitude of the observatory. All these characteristics define a photometric system. Once the data are extinction corrected, they have to be compared with data obtained at other sites, with other filters and detectors. Even working in well-established systems the instrumental responses of various equipment (i.e. CCD camera, filters) are rarely identical. For instance, the transmission curves and the central wavelengths of the original Bessell filters are different from the ones of the Bessell filters used for the observations. A *color transformation* is needed to transform data obtained with a particular photometric system to a standard system.

Many stellar sources have a spectral energy distribution that resembles the one of a blackbody. Thus we evaluate the color transformation for a blackbody. The energy distribution of a blackbody at temperature T is given by the Planck equation

$$L(\lambda) = \frac{2hc^2}{\lambda^5} \left[\exp\left(\frac{hc}{\lambda kT}\right) - 1 \right]^{-1}, \quad (\text{B.5})$$

where h and k are the Planck and Boltzmann constants, respectively. Examples of blackbody energy distribution for different temperatures are shown in Fig. B.3 (c).

The monochromatic magnitude of a blackbody at temperature T is:

$$m(\lambda) = 12.5 \log(\lambda) + 2.5 \log \left[\exp\left(\frac{hc}{\lambda kT}\right) - 1 \right] + C(\lambda). \quad (\text{B.6})$$

where $m(\lambda)$ is the object magnitude already corrected for extinction. The first term on the right side of the equation does not depend on characteristics of the energy source or of the atmosphere, but only on wavelength. It is a *zero-point* contribution and it can be incorporated in $C(\lambda)$, together with the sensitivity of the equipment which is also a function of wavelength. In the conditions of the Wien approximation ($hc/\lambda kT \gg 1$), Eq. B.6 becomes:

$$m(\lambda) = 2.5 \log(e) \left[\frac{hc}{\lambda kT} \right] + C(\lambda), \quad (\text{B.7})$$

where the magnitude is a linear function of $1/\lambda$ with a proportionality factor depending on the temperature T of the blackbody.

Similarly, a color index defined between wavelengths λ_1 and λ_2 includes a linear term in $\left[\frac{1}{\lambda_2} - \frac{1}{\lambda_1} \right]$:

$$m(\lambda_2) - m(\lambda_1) = 2.5 \log(e) \left[\frac{hc}{kT} \right] \left(\frac{1}{\lambda_2} - \frac{1}{\lambda_1} \right) + C(\lambda_2) - C(\lambda_1). \quad (\text{B.8})$$

We can assume now that a standard system is established with wavelengths λ_3 and λ_4 and the wavelengths of our instrumental photometric system (with which we measure blackbodies) are λ_1 and λ_2 , with $\lambda_1 \simeq \lambda_3$ and $\lambda_2 \simeq \lambda_4$, expressing that with our equipment we are trying to reproduce the standard photometric system.

Combining Eq. B.7 and B.8 we obtain the expression for $m(\lambda_3)$:

$$m(\lambda_3) - m(\lambda_1) = \frac{\frac{1}{\lambda_3} - \frac{1}{\lambda_1}}{\frac{1}{\lambda_2} - \frac{1}{\lambda_1}} \cdot [m(\lambda_2) - m(\lambda_1)] + C, \quad (\text{B.9})$$

where all zero-point terms have been grouped in C which is function of λ_1 , λ_2 and λ_3 . The color transformation necessary to bring the magnitude $m(\lambda_1)$ of a blackbody in the instrumental photometric system to the magnitude $m(\lambda_3)$ in the standard photometric system is:

$$m(\lambda_3) - m(\lambda_1) = A_3 \cdot [m(\lambda_2) - m(\lambda_1)] + C_3, \quad (\text{B.10})$$

where A_3 can be calculated from the values of wavelengths λ_1 , λ_2 and λ_3 , while the *zero-point* constant C_3 depends only on the characteristics of the observing equipment. A_3 is called *color coefficient*; it is an instrumental parameter and it should not vary with time. $[m(\lambda_2) - m(\lambda_1)]$ is the color of the blackbody. For the Sun the Wien approximation is not valid; a generalized first order approximation is used.

In summary, in order to compare observations performed in different locations and with different instruments, data have to be corrected for the presence of the atmosphere between the observer and the object and for the color sensitivity of the optical system. The flux calibrated measured magnitude of the object is called apparent magnitude and it is determined using:

$$m_{\text{apparent}} = m_{\text{meas}} + m_{\text{zero point}} - k \cdot AM + A \cdot \text{color}, \quad (\text{B.11})$$

where m_{meas} is the measured magnitude, $m_{\text{zero point}}$ the zero point, k and A the extinction and color coefficients, respectively, and “color” is the color of the object.

The color of the object is often not known. In first approximation the color of the Sun can be used instead of the color of the object and with an iterative process the color of the object can be determined. The error introduced using the color of the Sun as object “color” is usually smaller than the uncertainties on the other parameters in Eq. B.11 since the color coefficient A is small. Thus, often the iterative procedure is not applied and the Sun color is used instead by default.

B.4 Determination of flux calibration coefficients

Flux calibration coefficients (zero point, extinction coefficient and color coefficient) are determined using photometric standard star fields observed with the same instrument configuration (optic filter, detector and operation mode) as for the science frames. For those stars the visual magnitude together with their colors B-V, U-B, V-R and R-I, obtained using a standard photometric system (for instance the original Bessell filters), is tabulated (Landolt 1992). An example of photometric standard star field (PG1047+003) is shown in Fig. B.4.

After the photometric standard star fields have been fully reduced (Sec. 3.4), with the technique of aperture photometry we measured the magnitude of the reference stars. Using Eq. B.11, where the apparent magnitude corresponds to the tabulated one, for each reference star we obtain a linear equation in which the flux calibration coefficients ($m_{\text{zero point}}$, k and A) are unknown:

$$y = a + b \cdot x + c \cdot z, \quad (\text{B.12})$$

where $y = m_{\text{tabulated}} - m_{\text{meas}}$ is the difference between the tabulated and the measured magnitude of the star, $a = m_{\text{zero point}}$ is the zero point, $b = -k$ the extinction coefficient and $x = AM$ the airmass at which the star has been observed, $c = A$ the color coefficient and z is the color of the star.

The flux calibration coefficients, together with their errors, can be determined with the least square method, which minimizes the sum of the squares of the residuals:

$$\sum_{i=1}^n [a + bx_i + cz_i - y_i]^2. \quad (\text{B.13})$$

This procedure can be applied if several standard star fields are observed and they cover a wide airmass range.

In case only one photometric standard star field is observed, it is not possible to determine

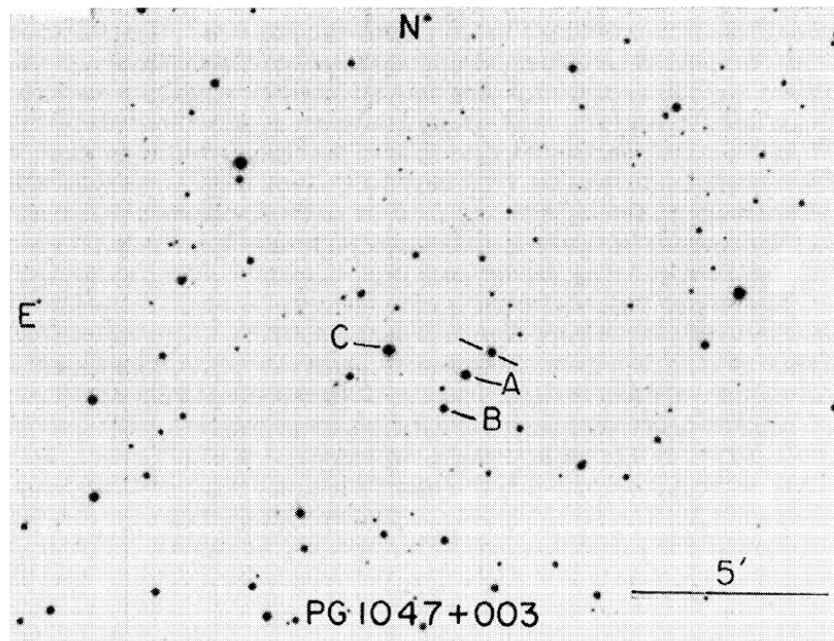


Figure B.4: Photometric standard star field PG1047+003. The position of the four reference stars is marked. Figure from Landolt (1992).

all three flux calibration coefficients in the way described. Thus, the zero point is determined from Eq. B.11, assuming extinction and color coefficients as provided by ESO for the night of the observation or as determined from previous observations. It is possible to adopt the flux calibration coefficients determined from a previous observation if: 1) the observations are close in time; 2) no changes in the configuration of the equipment took place (i.e. cleaning of the mirror, change of filter); 3) the atmosphere is stable.

C Table of measured brightness of 67P/C-G

Reduced magnitude $m(1,1,\alpha)$ in R filter from April 2004, June 2004, May 2006, August 2006 and July 2007 observations. σ is the error in the reduced magnitude and “Day” is the day of the observation.

time (h)	$m(1,1,\alpha)$ [mag]	σ [mag]	Day
0.465	15.44	0.05	1
0.560	15.46	0.05	1
0.657	15.47	0.05	1
0.751	15.57	0.05	1
0.854	15.59	0.05	1
1.143	15.60	0.05	1
1.237	15.61	0.05	1
2.850	15.38	0.05	1
2.944	15.35	0.05	1
3.040	15.36	0.05	1
3.421	15.33	0.05	1
4.179	15.37	0.05	1
4.274	15.37	0.05	1
5.918	15.26	0.05	1
6.013	15.30	0.05	1
6.201	15.28	0.05	1
6.295	15.33	0.05	1
6.488	15.31	0.05	1
6.980	15.33	0.05	1
8.126	15.51	0.05	1
8.408	15.56	0.05	1
8.503	15.58	0.05	1
8.602	15.64	0.05	1
8.695	15.58	0.05	1
8.884	15.50	0.05	1
119.979	15.37	0.05	2
120.305	15.38	0.05	2

continued on next page...

...continued from previous page

time (h)	m(1,1, α) [mag]	σ [mag]	Day
120.405	15.20	0.05	2
120.502	15.36	0.05	2
120.595	15.18	0.05	2
120.689	15.17	0.05	2
120.782	15.20	0.05	2
120.915	15.23	0.05	2
121.009	15.22	0.05	2
121.102	15.23	0.05	2
121.289	15.23	0.05	2
121.387	15.28	0.05	2
121.481	15.29	0.05	2
121.575	15.27	0.05	2
121.669	15.31	0.05	2
122.338	15.41	0.05	2
123.094	15.39	0.05	2
123.188	15.51	0.05	2
123.304	15.62	0.05	2
123.398	15.61	0.05	2
123.491	15.62	0.05	2
123.586	15.26	0.05	2
123.680	15.56	0.05	2
124.496	15.49	0.05	2
124.590	15.43	0.05	2
124.683	15.41	0.05	2
124.777	15.35	0.05	2
124.875	15.35	0.05	2
124.969	15.30	0.05	2
125.063	15.35	0.05	2
125.156	15.31	0.05	2
125.250	15.31	0.05	2
125.809	15.35	0.05	2
125.902	15.35	0.05	2
125.996	15.39	0.05	2
126.089	15.41	0.05	2
126.184	15.32	0.05	2
126.282	15.24	0.05	2
126.376	15.34	0.05	2
126.470	15.37	0.05	2
126.563	15.27	0.05	2
126.657	15.29	0.05	2
127.994	15.49	0.05	2

continued on next page...

...continued from previous page

time (h)	m(1,1, α) [mag]	σ [mag]	Day
128.088	15.44	0.05	2
128.562	15.47	0.05	2
128.656	15.52	0.05	2
128.750	15.49	0.05	2
143.737	15.44	0.05	3
143.831	15.40	0.05	3
143.925	15.35	0.05	3
144.019	15.30	0.05	3
144.398	15.24	0.05	3
144.492	15.26	0.05	3
146.089	15.27	0.05	3
147.472	15.35	0.05	3
147.566	15.41	0.05	3
147.660	15.36	0.05	3
149.157	15.48	0.05	3
149.251	15.51	0.05	3
149.344	15.54	0.05	3
149.550	15.49	0.05	3
151.751	15.37	0.05	3
152.172	15.35	0.05	3
152.270	15.23	0.05	3
152.365	15.33	0.05	3
152.459	15.33	0.05	3
152.570	15.29	0.05	3
152.669	15.39	0.05	3
152.763	15.39	0.05	3
152.857	15.34	0.05	3
2016.982	16.23	0.05	4
2017.112	16.26	0.05	4
2017.220	16.20	0.05	4
2040.754	16.21	0.05	4
2040.863	16.20	0.05	4
2040.971	16.24	0.05	4
2137.801	15.99	0.05	4
2137.918	15.98	0.05	4
2138.027	16.06	0.05	4
2158.769	16.05	0.05	4
2158.937	16.07	0.05	4
2159.046	16.11	0.05	4
10007.328	15.83	0.06	7
10007.369	15.75	0.06	7

continued on next page...

...continued from previous page

time (h)	m(1,1, α) [mag]	σ [mag]	Day
10007.410	15.86	0.06	7
10007.450	15.83	0.06	7
10007.490	15.82	0.06	7
10007.535	15.77	0.06	7
10007.575	15.80	0.06	7
10007.615	15.84	0.06	7
10007.655	15.78	0.06	7
10007.696	15.82	0.06	7
10007.740	15.78	0.06	7
10007.780	15.84	0.06	7
10007.821	15.83	0.06	7
10007.862	15.84	0.06	7
10007.902	15.78	0.06	7
10007.947	15.87	0.06	7
10007.987	15.82	0.06	7
10008.027	15.83	0.06	7
10008.068	15.78	0.06	7
10008.109	15.90	0.06	7
10008.155	15.85	0.06	7
10008.195	15.89	0.06	7
10008.235	15.85	0.06	7
10008.276	15.80	0.06	7
10008.316	15.87	0.06	7
10008.360	15.84	0.06	7
10008.400	15.80	0.06	7
10008.441	15.79	0.06	7
10008.481	15.79	0.06	7
10008.522	15.82	0.06	7
10008.567	15.80	0.06	7
10008.607	15.77	0.06	7
10008.655	15.71	0.06	7
10008.705	15.71	0.06	7
10008.745	15.73	0.06	7
10008.790	15.68	0.06	7
10008.830	15.73	0.06	7
10008.871	15.79	0.06	7
10008.912	15.71	0.06	7
10008.953	15.81	0.06	7
10010.020	15.77	0.06	7
10010.061	15.76	0.06	7
10010.104	15.66	0.06	7

continued on next page...

...continued from previous page

time (h)	m(1,1, α) [mag]	σ [mag]	Day
10010.145	15.67	0.06	7
10010.185	15.70	0.06	7
10010.231	15.80	0.06	7
10010.663	15.60	0.06	7
10010.704	15.61	0.06	7
10010.746	15.61	0.07	7
10010.787	15.60	0.06	7
10010.829	15.62	0.06	7
10010.910	15.62	0.06	7
10010.951	15.63	0.06	7
10010.993	15.56	0.06	7
10011.034	15.67	0.06	7
10011.078	15.63	0.06	7
10011.168	15.61	0.06	7
10011.210	15.61	0.06	7
10011.251	15.61	0.06	7
10011.293	15.64	0.06	7
10011.335	15.62	0.06	7
10011.380	15.65	0.06	7
10011.422	15.71	0.06	7
10011.463	15.62	0.06	7
10011.504	15.64	0.06	7
10011.546	15.66	0.06	7
10011.590	15.63	0.06	7
10011.632	15.65	0.06	7
10011.674	15.68	0.06	7
10011.715	15.70	0.06	7
10011.758	15.56	0.06	7
10011.816	15.64	0.06	7
10011.858	15.65	0.06	7
10011.899	15.65	0.06	7
10011.942	15.66	0.06	7
10011.983	15.63	0.06	7
10012.029	15.68	0.06	7
10012.070	15.63	0.06	7
10012.113	15.74	0.06	7
10012.157	15.77	0.06	7
10012.200	15.69	0.06	7
10012.246	15.69	0.06	7
10012.288	15.64	0.06	7
10012.330	15.68	0.06	7

continued on next page...

...continued from previous page

time (h)	m(1,1, α) [mag]	σ [mag]	Day
10012.372	15.71	0.06	7
10012.413	15.70	0.06	7
10012.459	15.67	0.06	7
10012.501	15.72	0.06	7
10012.543	15.72	0.06	7
10012.584	15.71	0.06	7
10012.733	15.72	0.06	7
10012.775	15.71	0.06	7
10012.816	15.80	0.06	7
10012.858	15.78	0.06	7
10013.379	15.86	0.06	7
10013.418	15.82	0.06	7
10013.457	15.84	0.06	7
10014.038	15.88	0.06	7
10014.079	15.88	0.06	7
10014.212	15.93	0.06	7
10014.254	15.87	0.06	7
10014.296	15.93	0.06	7
10014.380	15.95	0.06	7
10014.427	15.92	0.06	7
10014.470	15.94	0.06	7
10014.514	15.89	0.06	7
10014.556	15.91	0.06	7
10014.597	15.90	0.06	7
10014.647	15.87	0.06	7
10014.689	15.86	0.06	7
10014.731	15.85	0.07	7
10014.815	15.84	0.06	7
10014.861	15.89	0.06	7
10014.906	15.87	0.06	7
10014.947	15.82	0.07	7
10014.989	15.79	0.07	7
10015.032	15.88	0.07	7
10015.077	15.79	0.07	7
10015.120	15.74	0.07	7
10015.205	15.66	0.07	7
10015.246	15.72	0.07	7
10015.292	15.69	0.07	7
10015.335	15.62	0.07	7
10015.377	15.66	0.07	7
10015.420	15.64	0.07	7

continued on next page...

...continued from previous page

time (h)	m(1,1, α) [mag]	σ [mag]	Day
10015.462	15.65	0.07	7
-0.340	15.97	0.10	5
-0.252	16.04	0.08	5
-0.168	15.97	0.09	5
-0.117	16.06	0.08	5
-0.065	16.06	0.08	5
-0.016	16.18	0.09	5
0.033	16.10	0.09	5
0.082	16.06	0.08	5
0.132	16.08	0.08	5
0.182	16.02	0.08	5
0.231	16.19	0.08	5
0.280	16.12	0.09	5
0.329	16.13	0.08	5
0.476	16.11	0.06	5
0.566	16.18	0.06	5
0.655	16.15	0.06	5
0.746	16.23	0.06	5
0.835	16.16	0.06	5
0.925	16.19	0.06	5
1.015	16.15	0.06	5
1.105	16.15	0.06	5
1.285	16.15	0.06	5
1.453	16.10	0.04	5
1.543	16.17	0.05	5
1.633	16.18	0.04	5
1.722	16.20	0.04	5
1.813	16.20	0.05	5
1.903	16.33	0.04	5
1.993	16.25	0.04	5
2.083	16.20	0.04	5
2.172	16.26	0.04	5
2.263	16.29	0.05	5
0.464	15.58	0.04	6
0.558	15.52	0.04	6
0.886	15.57	0.04	6
0.980	15.58	0.04	6
1.321	15.48	0.04	6
1.416	15.49	0.04	6
1.513	15.48	0.04	6
1.607	15.44	0.05	6

continued on next page...

...continued from previous page

time (h)	$m(1,1,\alpha)$ [mag]	σ [mag]	Day
1.715	15.49	0.04	6
1.810	15.48	0.04	6
1.906	15.51	0.04	6
2.000	15.46	0.05	6
2.294	15.46	0.04	6
2.388	15.47	0.04	6
3.902	15.37	0.04	6
4.018	15.37	0.04	6
4.117	15.27	0.04	6
4.212	15.28	0.04	6
4.530	15.30	0.04	6
4.624	15.29	0.04	6
5.068	15.24	0.04	6
5.162	15.29	0.04	6
5.261	15.29	0.04	6
5.358	15.29	0.04	6
6.488	15.52	0.04	6
6.582	15.55	0.04	6
6.679	15.62	0.04	6
6.773	15.57	0.04	6
7.365	15.67	0.05	6
7.459	15.42	0.11	6

Table C.1: Results of R filter photometry of 67P/C-G for all observing runs. $m(1,1,\alpha)$ is the reduced magnitude and σ its error. Day is the day of the observation: 1 = May 25, 2006; 2 = May 30, 2006; 3 = May 31, 2006; 4 = August 2006; 5 = June 2004; 6 = April 2004; 7 = July 2007. The time relative to May 2006, August 2006 and July 2007 runs is normalized to May 26, 2006 00:00 UT. The time series of April 2004 and June 2004 are normalized to April 15, 2004 00:00 UT and June 16, 2004 23:20 UT, respectively. The times are light-time corrected.

D Rotational period and phase function determination

For the determination of the rotational period and phase function of 67P/C-G we used two methods: the Phase Dispersion Minimization with weighting (hereafter PDM) and the χ^2 minimization using a sum of harmonics fitted to the observations (hereafter χ^2 minimization). Both methods measure the quality of the rotational phase profile for a number of trial rotational periods simultaneously with, in this implementation, the phase function coefficient.

D.1 Phase Dispersion Minimization method

In the PDM method (Stellingwerf 1978, Drahus & Waniak 2006) the dataset is divided in bins (of equal width) and inside each bin the mean value of the data points is determined. What has to be minimized is the dispersion of the data points with respect to the mean value inside each bin. The best rotational period is the one producing the least observational scatter in such a grid of bins. Mathematically, PDM is a least-square fitting technique where the fit is relative to the mean curve as defined by the means of each bin. The PDM algorithm returns, for each value of the trial rotational frequency f_0 and phase coefficient, the quantity Θ whose minima indicate possible periodicities present in the light curve. This parameter is defined as:

$$\Theta = \frac{\sigma_{bin}^2}{\sigma_{tot}^2}, \quad (D.1)$$

where the numerator is the variance in the phased binned data and the denominator is the total variance of the measured points. The expression of the former term is (Drahus & Waniak 2006):

$$\begin{aligned} \sigma_{bin}^2 &= \left[\left(\sum_{j=1}^M n_j \right) \left(\sum_{j=1}^M n_j - M_f \right)^{-1} \right] \\ &\times \left(\sum_{j=1}^M \sum_{k=1}^{n_j} w_{jk} (S_{jk} - \bar{S}_j)^2 \right) \left(\sum_{j=1}^M \sum_{k=1}^{n_j} w_{jk} \right)^{-1} \end{aligned} \quad (D.2)$$

where M is the number of computational windows, equal to the product of the number of bins times the number of covers ($M = N_b N_c$), M_f is the number of non-empty windows,

D Rotational period and phase function determination

n_j the number of points in the j -th window, S_{jk} are the data points and w_{jk} their weights. \bar{S}_j is the mean signal in the j -th window:

$$\bar{S}_j = \left(\sum_{k=1}^{n_j} w_{jk} S_{jk} \right) \left(\sum_{k=1}^{n_j} w_{jk} \right)^{-1}, \quad (\text{D.3})$$

The total variance of the measured point is (Drahus & Waniak 2006):

$$\sigma_{tot}^2 = \frac{N}{N-1} \left(\sum_{i=1}^n w_i (S_i - \bar{S}_{tot})^2 \right) \left(\sum_{i=1}^n w_i \right)^{-1}, \quad (\text{D.4})$$

where N is the number of data point, S_i are the measured data points and w_i their weight. \bar{S}_{tot} is the mean value, given by:

$$\bar{S}_{tot} = \left(\sum_{i=1}^n w_i S_i \right) \left(\sum_{i=1}^n w_i \right)^{-1}. \quad (\text{D.5})$$

The working parameters of the PDM algorithm are the number of bins N_b and the number of covers N_c . The optimum number of bins in which the phase window has to be divided depends upon the number of data points to analyse and on their accuracy. If too few bins are used, real variabilities in the light curve can be interpreted as noise and thus solutions can be missed. This is shown in Fig. D.1 (left panel) where $N_b = 3$ is used. The dispersion of the data with respect to the mean value inside each bin is very high, due to the too large bin width employed.

If, instead, a too large number of bins is employed (Fig. D.1, right panel) artificial structures can be introduced and the method is unstable due to the poor data statistics in the computational windows. A good approach is to choose the number of bins in order to have in average at least 3 data points per bin and that the standard deviation in each bin is comparable with the accuracy of the measurements.

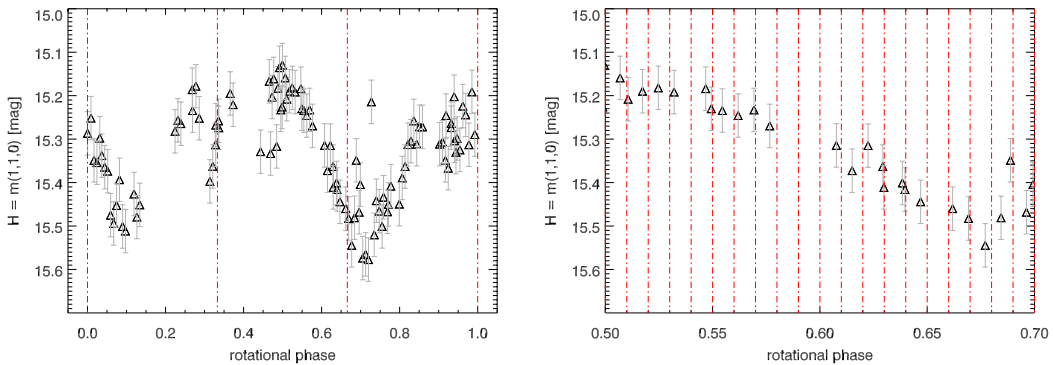


Figure D.1: Phased light curve of 67P/C-G. The red vertical lines show the bins used. Left panel: $N_b = 3$. Right panel: $N_b = 100$. In order to resolve the individual bins, a zoom of a part of the whole phase range is displayed.

D.2 χ^2 minimization method

The χ^2 minimization method consists in minimizing the dispersion of the data with respect to a synthetic profile which, in our case, is a sum of K harmonics:

$$\begin{aligned} mag(t) &= mag_0 + \sum_{n=1}^K \alpha_n \cdot \sin(2\pi n f_0 t + \phi_n) \\ &= mag_0 + \sum_{n=1}^K A_n \cdot \sin(2\pi n f_0 t) + B_n \cdot \cos(2\pi n f_0 t), \end{aligned} \quad (D.6)$$

where mag_0 is the mean magnitude and f_0 the rotational frequency. For each value of f_0 we obtain a different synthetic profile.

As for the PDM method, also the χ^2 minimization method returns, for each value of the trial rotational frequency f_0 and phase coefficient, the quantity Θ whose minima indicate possible periodicities present in the light curve. This parameter is defined in a similar way as for the PDM:

$$\Theta = \frac{\sigma_{fit}^2}{\sigma_{tot}^2}, \quad (D.7)$$

where the numerator is the variance with respect to the synthetic profile and the denominator is the total variance of the measured points (Equation D.4).

The single parameter of the χ^2 minimization method is the number of frequencies N_f , i.e. the number of harmonics including the base frequency that are used for fitting. The number of frequencies to employ depends on the light curve which has to be reproduced and thus caution has to be taken in its choice. When too low order synthetic profiles are used, the real variations in the light curve are interpreted as noise, while too high order profiles might lead to fitting of structures which are not real. Figure D.3 shows the light curve of 67P/C-G with superimposed synthetic profiles from Equation D.6 for a fixed value of the rotational frequency and number of frequencies from $N_f = 1$ to $N_f = 9$. The larger N_f is, the more structured the synthetic profile is.

The role played by the number of bins in the PDM method is played by the number of frequencies in the χ^2 minimization method. In fact in both cases, if these two aforementioned parameters are chosen too small, real variations present in the light curve can be interpreted as noise and thus solutions can be missed. If, instead, N_b and N_f are chosen too big, artificial (i.e. noise-induced) small-scale variations can be detected.

For our analysis, as working parameters, we chose: $N_b = 25$, $N_c = 5$ and $N_f = 5$. The phased light curve of 67P/C-G with overplotted bins used for the rotational period and phase function determination employing the PDM algorithm and the synthetic profile used for analysis employing the χ^2 minimization method are displayed in Fig. D.2.

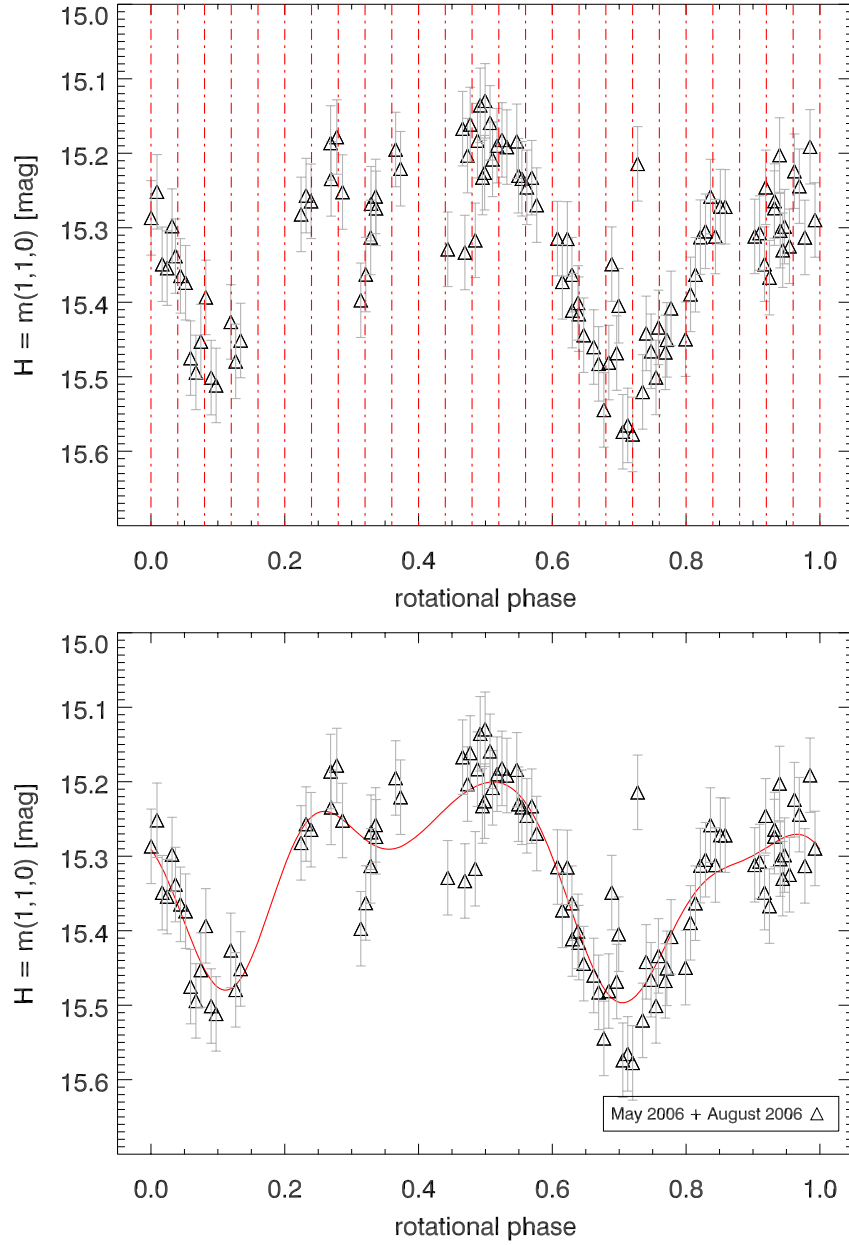


Figure D.2: Phased light curve of 67P/C-G with superimposed: left panel: the bins used for the rotational period and phase determination employing the PDM algorithm (left panel); right panel: a synthetic profile obtained from Equation D.6, with $T_0 \equiv 1/f_0 = 12.7047$ h and $N_f = 5$.

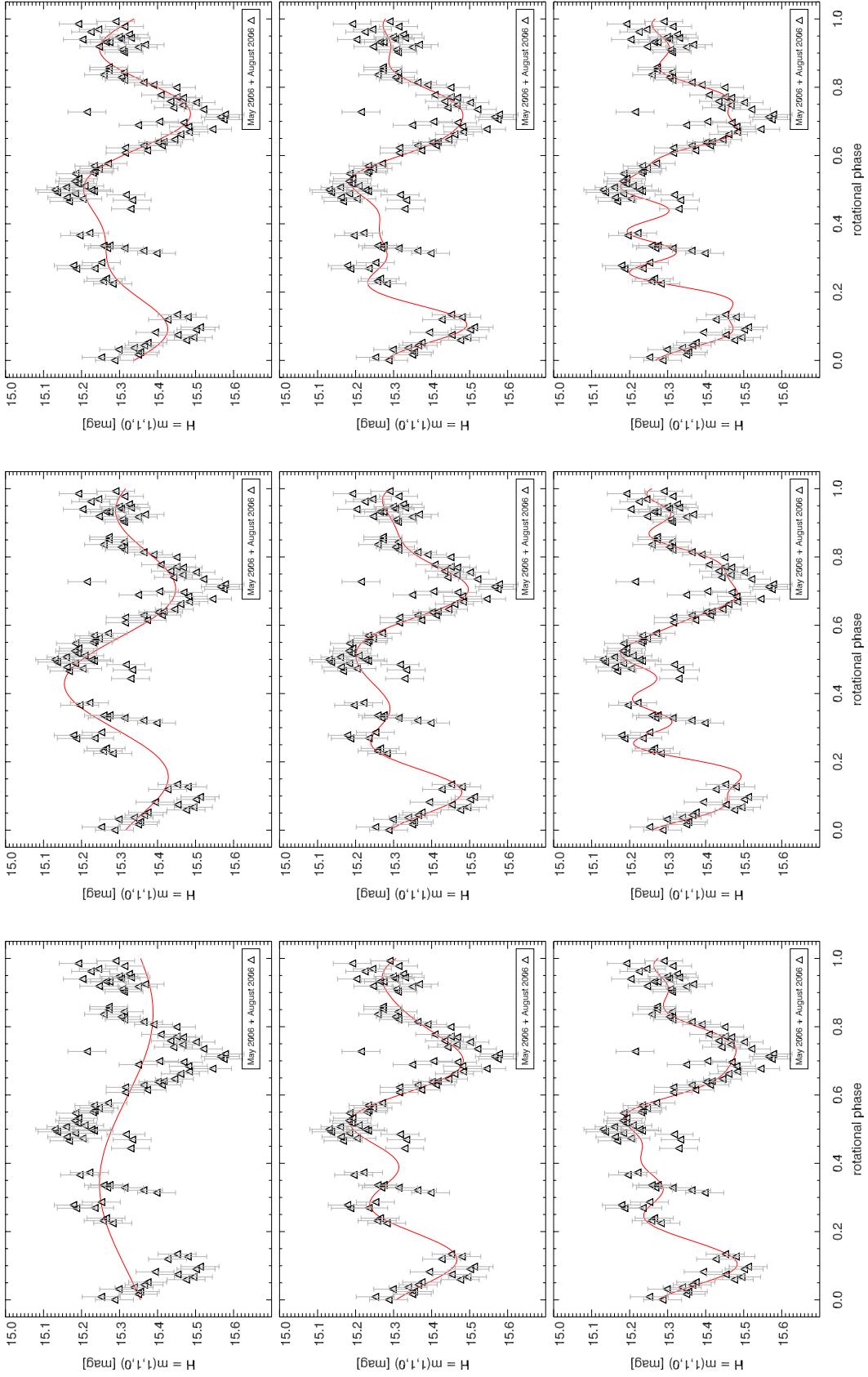


Figure D.3: Phased light curve of 67P/C-G with superimposed the synthetic profile obtained from Equation D.6, with $T_0 \equiv 1/f_0 = 12.7047$ h and N_f varying from 1 to 9 going from the top left panel to the bottom right one.

Bibliography

- Agarwal, J., Müller, M., Böhnhardt, H., Grün, E., 2006, Modelling the large particle environment of comet 67P/Churyumov-Gerasimenko, *Advances in Space Research*, 38, 9, 2049-2053.
- Agarwal, J., Mueller, M. and Gruen, E., 2007, Dust environment modelling of comet 67P/Churyumov-Gerasimenko, *Space Science Reviews*, 128, 79-131.
- Agarwal, J., 2007, The emission of large dust particles from comet 67P/Churyumov-Gerasimenko constrained by observation and modelling of its dust trail, PhD thesis.
- A'Hearn, M. F., Schleicher, D. G., Millis, R. L., et al., 1980, Comet Bowell 1980b, *Astronomical Journal*, 89, 579-591.
- A'Hearn, M. F., Millis, R. L., Schleicher, D. G., et al, 1995, The ensemble properties of comets: Results from narrowband photometry of 85 comets, 1976-1992, *Icarus*, 223-270.
- A'Hearn, M. F., Belton, M. J. S., Delamere, W. A., et al., 2005, Deep Impact: Excavating Comet Tempel 1, *Science*, 310, 258-264.
- A'Hearn, M. F., Combi, M. R., 2007, Deep Impact at Comet Tempel 1, *Icarus*, 187, 1-3.
- Belton, M. J. S., Meech, K. J., A'Hearn, M. F., et al., 2005, Deep Impact: Working Properties for the Target Nucleus Comet 9P/Tempel 1, *Space Science Reviews*, 117, 137-160.
- Belyaev, N. A., Kresak, L., Pittich, E. M., 1986, Catalogue of short-period comets, Bratislava: Slovak Academy of Sciences, Astronomical Institute.
- Birney, D. S., Gonzalez, G., Oesper, D., 2006, Book review: *Observational astronomy/Second edition*, Cambridge University Press, 312 pp.
- Bockelée-Morvan, D., Moreno, R., Biver, N., et al., 2004, CO and dust productions in 67P/Churyumov-Gerasimenko at 3 AU post-perihelion, in L. Colangeli, E. Mazzotta Epifani and P. Palumbo, editors, *ASSL Vol. 311: The New Rosetta Targets. Observations, Simulations and Instrument Performances*, 25-36.
- Böhnhardt, H., Birkle, K., 1994, Time variable coma structures in comet P/Swift-Tuttle, *A&AS*, 107, 101-120.

- Bönnhardt, H., Delahodde, C., Sekiguchi, T., et al., 2002, VLT observations of comet 46P/Wirtanen, *A&A*, 387, 1107-1113.
- Bönnhardt, H., Tozzi, G.P., Bagnulo, S., et al., 2008, Photometry and polarimetry of the nucleus of comet 2P/Encke, *A&A*, in press.
- Bowell, E., Hapke, B., Domingue, D., et al., 1989, Application of photometric models to asteroids, In *Asteroids II*, R. P. Binzel, T. Gehrels, M. S. Matthews (eds.), University of Arizona Press, 1989, 524-556.
- Brownlee, D. E., Horz, F., Newburn, R. L., et al., 2005, Surface of Young Jupiter Family Comet 81 P/Wild 2: View from the Stardust Spacecraft, *Science*, 304, 1764-1769.
- Chesley, S. R., 2004, An Estimate of the Spin Axis of Comet 67P/Churyumov-Gerasimenko, DPS meeting #36, #21.07; *BAAS*, 36, 1118.
- Cremonese, G., Bönnhardt, H., Crovisier, J., et al., 1997, Neutral sodium from Comet Hale-Bopp: a third type of tail, *Astrophysical Journal Letters*, 490, L199.
- Davidsson, B. J. R., Gutiérrez, P. J., 2005, Nucleus properties of Comet 67P/Churyumov Gerasimenko estimated from non-gravitational force modeling, *Icarus*, 176, 453-477.
- Delsanti, A.C., Bönnhardt, H., Barrera, L. et al., 2001, BVRI photometry of 27 Kuiper Belt Objects with ESO/Very Large Telescope, *A&A*, 380, 347-358.
- Delsemme, A. H., 1982, Chemical composition of cometary nuclei, In *Comets*, ed. Wilkening L. L., Tucson, AZ, University of Arizona Press, 85-130.
- Dohnanyi, J. W., 1969, Collisional models of asteroids and their debris, *J. Geophys. Res.*, 74, 2531-2554.
- Drahus, M., Waniak, W., 2006, Non-constant rotation period of Comet C/2001 K5 (LINEAR), *Icarus*, 185, 544-557.
- Fernández, J. A., Ip, W.-H., 1981, Dynamical evolution of a cometary swarm in the outer planetary region, *Icarus*, 47, 470-479.
- Fernández, J. A., Tancredi, G., Rickman, H., Licandro, J., 1999, The population, magnitudes, and sizes of Jupiter family comets, *A&A*, 352, 327-340.
- Fernandez, Y. R., Lisse, C. M., Ulrich Kaeufl, H. et al., 2000, Physical properties of the nucleus of comet 2P/Encke, *Icarus*, 147, 145-160.
- Ferrin, I., 2005, Secular light curve of Comet 28P/Neujmin 1 and of spacecraft target Comets 1P/Halley, 9P/Tempel 1, 19P/Borrelly, 21P/Giacobinni Zinner, 26P/Grigg Skjellerup, 67P/Churyumov Gerasimenko, and 81P/Wild 2, *Icarus*, 178, 493-516.
- Ferrin, I., 2007, Secular light curve of Comet 9P/Tempel 1, *Icarus*, 187, 326-331.
- Fulle, M., 1987, A new approach to the Finson-Probstein method of interpreting cometary dust tails, *A&A*, 171, 327-335.

- Fulle, M., Sedmak, G., 1988, Photometrical analysis of the Neck-Line structure of Comet Bennet 1970II, *Icarus*, 74, 383-398.
- Fulle, M., Barbieri, C., Cremonese, G., et al., 2004, The dust environment of comet 67P/Churyumov-Gerasimenko, *A&A*, 422, 357-368.
- Glassmeier, K.-H., Böhnhardt, H., Koschny, et al., 2007, The Rosetta mission: flying towards the origin of the solar system, *Space Science Reviews*, 128, 1-21.
- Hanner, M. S., Tedesco, E., Tokunaga, A. T., et al, 1985, The dust coma of periodic Comet Churyumov- Gerasimenko (1982 VIII), *Icarus*, 64, 11-19.
- Hansen, K. C., Bagdonat, T., Motschmann, U., et al., The plasma environment of comet 67P/Churyumov-Gerasimenko throughout the Rosetta main mission, 2007, *Space Science Reviews*, 128, 133-166.
- Hardorp, J., 1980, The sun among the stars. II - Solar color, Hyades metal content, and distance, *A&A*, 88, 334-344.
- Jewitt, D., Luu, J., 1993, Discovery of the candidate Kuiper belt object 1992 QB1, *Nature*, 362, 730-732.
- Jewitt, D. C., 2002, From Kuiper Belt Object to cometary nucleus: the missing ultrared matter, *The Astronomical Journal*, 123, 1039-1049.
- Keller, H. U., 1990, The nucleus, In *Physics and chemistry of comets*, ed. Huebner W. F., 13-68.
- Keller, H. U., Britt, D., Buratti, B. J., Thomas, N., 2004, In situ observations of cometary nuclei, In *Comets II*, M. C. Festou, H. U. Keller, and H. A. Weaver (eds.), University of Arizona Press, Tucson, 211-222.
- Kelley, M. S., Reach, W. T., Lien, D. J., 2008, The dust trail of Comet 67P/Churyumov Gerasimenko, *Icarus*, 193, 572-587.
- Kidger, M. R., 2004, Dust production and coma morphology of 67P/Churyumov-Gerasimenko during the 2002/2003 apparition. II. A comparative study of dust production in 46P/Wirtanen and 67P/Churyumov-Gerasimenko during their 2002/2003 apparition, *A&A*, 420, 389-395.
- Kimura H., Liu C. P., 1977, On the structure of cometary dust tails, *Chinese Astronomy*, 1, 235-264.
- Kuiper, G. P., 1950, On the origin of the solar system, *Proceedings of the National Academy of Sciences of the United States of America*, 37, 1-14.
- Ishiguro, M., 2008, Cometary dust trail associated with Rosetta mission target: 67P/Churyumov Gerasimenko, *Icarus*, 193, 96-104.
- Lamy, P. L., Toth, I., 1995, Direct detection of a cometary nucleus with the Hubble Space Telescope, *A&A*, 293L, L43-L45.

- Lamy, P.L., Toth, I., Fernandez, Y. R., Weaver, H. A., 2004, The sizes, shapes, albedos, and colors of cometary nuclei, In *Comets II*, M. C. Festou, H. U. Keller, and H. A. Weaver (eds.), University of Arizona Press, Tucson, 223-264.
- Lamy, P. L., Jorda, L., Toth, I., et al., 2004, Visible and thermal infrared observations of the nucleus of comet 67P/Churyumov-Gerasimenko, 35th COSPAR Scientific Assembly 18 - 25 July 2004, Paris (France).
- Lamy, P. L., Toth, I., Weaver H. A., et al., 2006, Hubble Space Telescope observations of the nucleus and inner coma of comet 67P/Churyumov-Gerasimenko, *A&A*, 458, 669-678.
- Lamy, P. L., Toth, I., Davidsson, B. J. R. et al. 2007, A portrait of the nucleus of comet 67P/Churyumov-Gerasimenko, *Space Science Reviews*, 128, 23-66.
- Landolt, A. U., 1992, UBVRI photometric standard stars in the magnitude range 11.5-16.0 around the celestial equator, *Astronomical Journal*, 104, 340-371.
- Lang, K. R., 1974, *Astrophysical formulae: A compendium for the physicist and astrophysicist*, Springer-Verlag Berlin Heidelberg New York.
- Levison, H. F., 1996, Comet Taxonomy, Completing the inventory of the solar system, *Astronomical Society of the Pacific Conference Proceedings*, T.W. Rettig and J.M. Hahn Eds., 107, 173-191.
- Lowry, S. C., Fitzsimmons, A., Collander-Brown, S., 2003, CCD photometry of distant comets. III. Ensemble properties of Jupiter-family comets, *A&A*, 397, 329-343.
- Lowry, S. C., Fitzsimmons, A., Jorda, L., et al., 2006, Aphelion observations of the nucleus of comet 67P/Churyumov-Gerasimenko: target of ESA's Rosetta comet orbiter mission, DPS meeting #38, #08.01; *BAAS*, 38, 492.
- Luu, J. X., 1993, Spectral diversity among the nuclei of comets, *Icarus*, 104, 138-148.
- Moreno, F., Lara, L. M., Muñoz, O., et al., 2004, Dust in Comet 67P/Churyumov-Gerasimenko, *The Astrophysical Journal*, 613, 1263-1269.
- Michałowski, T. 1988, Photometric astrometry applied to asteroids 6, 15, 43, and 624, *Acta Astronomica*, 38, 455-468.
- Meeus, J., 1998, *Astronomical algorithms* (2nd ed.) by J. Meeus. Richmond, VA: Willmann-Bell.
- O'Brien, D. P., Greenberg, R., 2003, Steady-state size distributions for collisional populations: analytical solution with size-dependent strength, *Icarus*, 164, 334-345.
- Oort, J. H., 1950, The structure of the cloud of comets surrounding the Solar System and a hypothesis concerning its origin, *Bull. Astron. Inst. Neth.*, 11, 91-110.
- Osip, D. J., Schleicher, D. G., Millis, R. L., 1992, Comets - Groundbased observations of spacecraft mission candidates, *Icarus*, 98, 115-124.

- Pittichova, J., Meech, K. J., 2001, Rotation of Comet 81P/Wild 2, DPS Meeting #33, #20.05; BAAS, 33, 1075.
- Russell, H. N., 1916, On the albedo of the planets and their satellites, *Astrophysical Journal*, 43, 73.
- Samarasinha, N. H., Mueller, B. E. A., Belton, M. J. S., Jorda, L., 2004, Rotation of cometary nuclei, In *Comets II*, M. C. Festou, H. U. Keller, and H. A. Weaver (eds.), University of Arizona Press, Tucson, 281-299.
- Schleicher, D. G., 2006, Compositional and physical results for Rosetta's new target Comet 67P/Churyumov Gerasimenko from narrowband photometry and imaging, *Icarus*, 181, 442-457.
- Schulz, R., Stuewe, J. A., Bönhardt, H., 2004, Rosetta target comet 67P/Churyumov-Gerasimenko. Postperihelion gas and dust production rates, *A&A*, 422, L19-L21.
- Schwehm, G., Schulz, R., 1999, Rosetta Goes to Comet Wirtanen, *Space Science Reviews*, 90, 313-319.
- Samarasinha, N. H., Mueller, B. E. A., Belton, M. J. S., Jorda, L., 2004, Rotation of cometary nuclei, In *Comets II*, M. C. Festou, H. U. Keller, and H. A. Weaver (eds.), University of Arizona Press, Tucson, 281-299.
- Sekanina, Z., 1981, Rotation and precession of cometary nuclei, *Annual review of earth and planetary sciences*, 9, 113-145.
- Stellingwerf, R. F., 1978, Period determination using phase dispersion minimization, *Astrophys. J.*, 224, 953-960.
- Sterken, C., Manfroid, J., 1992, *Astronomical Photometry - A Guide*, Kluwer Academic Publishers, vol. 84, no. 6, p. 656.
- Storrs, A. D., Cochran, A. L., Barker, E. S., 1992, Spectrophotometry of the continuum in 18 comets, *Icarus*, 98, 163-178.
- Swamy, K. S. K., 1996, *Physics of comets*, World Scientific series in astronomy and astrophysics, Singapore: World Scientific, 2nd ed.
- Sykes, M. V., Hunten, D. M., Low, F. J., 1986a, Preliminary analysis of cometary dust trails, *Advances in Space Research*, 6, 67-78.
- Sykes, M. V., Lebofsky, L. A., Hunten, D. M., Low, F., 1986b, The discovery of dust trails in the orbits of periodic comets, *Science*, 232, 1115-1117.
- Sykes, M. V., Walker, R. G., 1992, Cometary dust trails. I - Survey, *Icarus*, 95, 180-210.
- Sykes, M. V., Gruen, E., Reach, W. T., Jenniskens, P., 2004, The interplanetary dust complex and comets, In *Comets II*, M. C. Festou, H. U. Keller, and H. A. Weaver (eds.), University of Arizona Press, Tucson, 677-693.

- Szabó, Gy. M., Kiss, L. L., Sárneczky, K., 2008, Cometary activity at 25.7 AU: Hale-Bopp 11 years after perihelion, *The Astrophysical Journal*, 677, L121-L124.
- Tancredi, G., Fernández, J. A., Rickman, H., Licandro, J., 2000, A catalog of observed nuclear magnitudes of Jupiter family comets, *A&AS*, 146, 73-90.
- Tedesco, E. F., 1989, Asteroid magnitudes, UBV colors, and IRAS albedos and diameters, In *Asteroids II*, R. P. Binzel, T. Gehrels, M. S. Matthews (eds.), University of Arizona Press, 1989, 1090-1138.
- Tubiana, C., Duffard, R., Barrera, L., Bönhardt, H., 2007, Photometric and spectroscopic observations of (132524) 2002 JF56: fly-by target of the New Horizons mission, *A&A*, 463, 1197-1199.
- Weiler, M., Rauer, H., Helbert, J., 2004, Optical observations of Comet 67P/Churyumov-Gerasimenko, *A&A*, 414, 749-755.
- Weissman, P. R., Lowry, S. C., 2003, The size distribution of Jupiter-Family cometary nuclei, 34th Annual Lunar and Planetary Science Conference, March 17-21, 2003, League City, Texas.
- West, R. M., Hainaut, O., Smette, A., 1991, Post-perihelion observations of P/Halley. III - an outburst at $R = 14.3$ AU, *A&A*, 246, L77-L80.
- Whipple, F. L., 1950, A comet model. I. The acceleration of Comet Encke, *Astrophys. J.*, 111, 375-394.

Publications

Refereed publications

C. Tubiana, L. Barrera, M. Drahus, H. Böhnhardt, 2008, Comet 67P/Churyumov-Gerasimenko at large heliocentric distance, *A&A*, 490, 377-386.

Oral presentations and posters

C. Tubiana, H. Böhnhardt, M. Drahus, L. Barrera, J. L. Ortiz, G. Schwehm, R. Schulz, J. Stuewe and J. B. Vincent, 7P/Churyumov-Gerasimenko: the Rosetta target comet in the aphelion arc, ACM 2008, Baltimore, Maryland, USA, 13-18 July 2008. (Poster).

C. Tubiana, H. Böhnhardt, L. Barrera, M. Drahus, J. L. Ortiz, G. Schwehm, and R. Schulz, VLT observations of 67P/Churyumov-Gerasimenko at large heliocentric distance, Coordination of ground-based observations of Rosetta target comet 67P/Churyumov-Gerasimenko, Orlando, Florida, USA, October 7, 2007. (Oral).

C. Tubiana, H. Böhnhardt, L. Barrera, J. Ortiz, G. Schwehm, and R. Schulz, 67P/Churyumov-Gerasimenko: photometry and spectroscopy of the Rosetta target comet at large heliocentric distance, DPS meeting, Orlando, FLorida, USA, October 7-12, 2007. (Oral).

C. Tubiana, H. Böhnhardt, L. Barrera, M. Drahus, J. L. Ortiz, G. Schwehm, R. Schulz, J. Stuewe, and M. Lippi, Photometry and spectroscopy of 67P/Churyumov-Gerasimenko at large heliocentric distance, European Planetary Science Congress 2007, Potsdam, August 19-24, 2007. (Oral).

C. Tubiana, H. Böhnhardt, L. Barrera, J. L. Ortiz, G. Schwehm, R. Schulz, and J. Stuewe, Characterization of physical parameters of the ROSETTA target comet 67P/Churyumov-Gerasimenko, European Planetary Science Congress 2006, Berlin, Sept 18-22, 2006. (Oral).

C. Tubiana, H. Böhnhardt, L. Barrera, J. L. Ortiz, G. Schwehm, R. Schulz, and J. Stuewe, Characterization of physical parameters of the ROSETTA target comet 67P/Churyumov-Gerasimenko, EGU 2006, Vienna, April 2-7, 2006. (Poster).

Acknowledgements

I do not find the right words to express my thanks to all the people who shared life moments with me and helped me to arrive till to this point.

First of all, I want to thank the Max Planck Institute for Solar System Research (MPS) and the International Max Planck Research School on Physical Processes in the Solar System and Beyond (IMPRS), in the person of Dr. Dieter Schmitt for giving me the opportunity to carry out the research presented in this thesis. It has been wonderful to work in such an international environment! Many thanks to my supervisor Dr. Hermann Böhnhardt, for all the things he taught me, for the great opportunity to go to observe at the VLT in Chile, for believing in my ability to carry out this work, for answering to all my questions and for all the discussions from which I learnt a lot about comets and life.

I want to thank Prof. Dr. Jürgen Blum for many valuable discussions which helped me to dig in the physical concepts behind my thesis work. Many thanks to Dr. Gian Paolo Tozzi who taught me how to observe a comet. Without you the extraction of the 67P/C-G spectra would have been a real nightmare! Thanks to Prof. Dr. Luis Barrera for the very nice time we spent together in Chile during the observations and for showing me beautiful places in the Atacama desert. I learnt a lot from you! I want to thank Dr. Marco Fulle and Dr. Jessica Agarwal for determining, with their dust tail simulations, the position angle of the neck line at the time of our observations. Jessica, thank you for answering to all my questions and for your useful suggestions! Many thanks to Michal Drahus, for applying his code to our data for the determination of the rotational period and phase function of 67P/C-G.

Thanks to all my friends here in the Institute: without you my life here would have been impossible! Un grazie specialissimo a Cleme, per essere stata una grande amica e per tutto quello che abbiamo condiviso in questi tre anni! Thanks to my friends in Italy: every time I come home it is like I never left from there. Thanks to my parents, my sister and my brothers and my grand mothers. Without your presence and support it would have been much harder to be far away for such a long time. Elias, thanks for these last three years. A wonderful future is waiting for us!

Curriculum Vitae

Persönliche Daten

Name: Cecilia Tubiana
Geburtsdatum: 28. August, 1980
Geburtsort: Moncalieri (Torino), Italien
Staatsangehörigkeit: Italienisch

Schulbildung

1986-1991: Scuola Elementare Statale "E. Franchetti"
1991-1994: Scuola Media Statale "A. Vivaldi"
1994-1999: Liceo Scientifico di Stato "A. Volta"

Studium

1999-2002: Bachelor in Physics
Università degli Studi di Torino
2002-2004: Master in Environmental and Biomedical Physics
Università degli Studi di Torino